Phase Model Analysis of the Effect of Acetylcholine on Neural Synchrony in Hippocampal Networks

by

Megha Susan Manoj

A thesis
presented to the University of Waterloo
in fulfillment of the
thesis requirement for the degree of
Master of Mathematics
in
Applied Mathematics

Waterloo, Ontario, Canada, 2025

© Megha Manoj 2025

Author's Declaration

I hereby declare that I am the sole author of this thesis. This is a true copy of the thesis, including any required final revisions, as accepted by my examiners.

I understand that my thesis may be made electronically available to the public.

Abstract

Neural assemblies—transiently coordinated groups of neurons—are observed in the hippocampus and are thought to underlie the encoding and consolidation of episodic memories. Acetylcholine (ACh), a key neuromodulator, plays a critical role in learning and memory and has been implicated in neurodegenerative disorders involving hippocampal dysfunction. A well-supported hypothesis suggests that high levels of ACh during active exploration and rapid eye movement (REM) sleep promote memory encoding, while low levels during quiet waking and slow-wave sleep (SWS) support memory consolidation.

In this study, we examine the bidirectional role of ACh in modulating neural assembly formation through its effect on neural synchrony in the CA3 region of the hippocampus. We construct a computational model of a network of excitatory pyramidal neurons, each equipped with a slow, voltage-dependent, non-inactivating potassium current (M-current), which is downregulated in the presence of ACh. Neural assemblies are modelled mathematically as cluster solutions—special types of phase-locked states. Using a phase model reduction of a pair of weakly coupled neurons, we analyze the existence and stability of cluster solutions that may emerge in larger networks equipped with all-to-all globally homogeneous, symmetric distance-dependent and nearest-neighbours coupling architectures.

Our results suggest that ACh shapes assembly formation by modulating network dynamics in CA3. Under low ACh conditions, the network tends to fully synchronize, whereas high ACh levels enable the emergence of multiple stable cluster states, allowing for distinct patterns of activity associated with memory encoding. These findings propose a mechanism by which ACh regulates transitions in hippocampal network states, supporting distinct stages of memory formation.

Acknowledgements

First and foremost, I would like to express my gratitude to my supervisor, Dr. Sue Ann Campbell, for her unwavering support and guidance throughout my graduate studies. I am especially thankful for the opportunities she has given me, all of which have contributed to an extremely meaningful and rewarding research experience.

I would like to thank the graduate committee: Dr. Sue Ann Campbell, Dr. Brian Ingalls and Dr. N Sri Namachchivaya, for taking the time to read this thesis.

I would like to thank the friends I made during my time here: Amrita, Elly, Mackenzie, Maliha and Albert. You have been a source of so much joy throughout my journey here in Waterloo. Truly, I could not have accomplished any of this—especially during the final months of my program—without your kindness and companionship.

I would also like to thank my cousins, Nithin and Jithin Abraham, and my close friends, Amal, Julie, Jacky and Oliver for always being my home away from home.

Lastly, to my family, Manoj Vengasseril Kuriakose, Mridula Manoj and Emil Kurian George—your love and support all these years, has been a constant source of strength in my life. Thank you for everything.

Dedication

This thesis is dedicated to my *Amma* and *Appa*, Mridula and Manoj, for being my first teachers and for nurturing my love of learning.

Table of Contents

Author's Declaration ii

Abstract iii

Acknowledgements iv

Dedication v

List of Figures x

List of Tables xx

1 Introduction 1

2 Biological Background 5

2.1 Anatomy of the brain 5

2.1.1 Neuron morphology and physiology 6

2.1.2 Synapse 7

2.2 Hippocampus 9

2.2.1 Hippocampal structure 9

2.2.2 Acetylcholine as a neuromodulator for the hippocampus. 10

3 Mathematical Neuroscience Background **13**

3.1 Electrophysiology of neurons . . . 13

3.2 Hodgkin-Huxley model of the action potential . . . 14

3.2.1 Circuit model of the neuronal membrane . . . 15

3.2.2 Channel kinetics . . . 17

3.2.3 Hodgkin Huxley description of an action potential . . . 18

3.2.4 Generalization of the Hodgkin-Huxley model . . . 20

3.3 Excitability of a neuron . . . 21

3.3.1 Muscarinic current (M-current) . . . 24

3.4 Modelling synaptic transmission . . . 25

3.4.1 Destexhe model . . . 26

4 Phase Model Reduction of Conductance-based Models **27**

4.1 Theoretical background . . . 27

4.2 Phase model for a weakly connected network . . . 29

4.2.1 Physical interpretation of the interaction function. . . . 35

4.2.2 Phase model for a network of weakly coupled oscillators . . . 36

4.2.3 Phase-locking . . . 37

5 Analysis of Cluster Solutions using a Phase-Model Approach **38**

5.1 Phase model approach . . . 39

5.1.1 Existence of cluster solutions . . . 41

5.1.2 Stability of the cluster solutions . . . 42

5.2 Stability analysis for symmetric bi-directional coupling . . . 46

5.2.1 Nearest neighbours . . . 47

5.2.2 All-to-all coupling . . . 48

6 Reduced Traub Miles' Model of a Pyramidal Neuron **52**
6.1 Model description . . . 53
6.1.1 Network level extension . . . 56
6.2 Effect of M-current on the steady-state behaviour (bifurcation analysis) . . . 58
6.3 Parameter choice for phase model approximation . . . 59

7 Results **64**
7.1 Methods . . . 64
7.1.1 Numerical simulations . . . 64
7.1.2 Phase model calculation . . . 66
7.2 A pair of reduced Traub-Miles model neurons . . . 68
7.2.1 Phase difference model . . . 68
7.2.2 Phase model predictions . . . 72
7.2.3 Numerical studies . . . 73
7.3 A network of arbitrary size with all-to-all global homogeneous coupling . . . 76
7.3.1 Phase model predictions . . . 76
7.3.2 Numerical studies . . . 78
7.3.3 Prediction failure in the anti-phase and 3− cluster solutions . . . 82
7.4 A network of arbitrary size with all-to-all globally heterogeneous coupling . . . 87
7.4.1 Phase model predictions . . . 87
7.4.2 Numerical studies . . . 88
7.5 A network of arbitrary size with nearest neighbour coupling . . . 97
7.5.1 Phase model predictions . . . 97
7.5.2 Numerical studies . . . 98

8 Discussion **108**

References **116**

APPENDICES **129**

A Appendix for Chapter 3 **130**

B Appendix for Chapter 4 **131**

C Appendix for Chapter 7 **132**

C.1 How to determine the firing order of cluster solutions 132

C.2 Numerical computation of interaction function 133

C.2.1 Fourier approximation of interaction function 134

C.3 Appendix for Section 7.3 134

C.4 Appendix for Section 7.4 137

C.5 Appendix for Section 7.5 139

List of Figures

2.1 A schematic of the hippocampus (highlighted in red) within the temporal lobe of the brain (highlighted in yellow). Created in https://BioRender.com 6

2.2 Schematic illustrating the structure of a typical pyramidal neuron, consisting of a soma, dendrites, and an axon. A chemical synapse between two neurons is also shown. Created in https://BioRender.com 7

2.3 Schematic of the trisynaptic circuit in the hippocampus which is the main information pathway. In the present thesis, we study the auto-associative network of the CA3 region. *Note: Inhibitory interneurons not shown.* Created in https://BioRender.com 11

3.1 Schematic for the equivalent circuit model of the cell as proposed by Hodgkin and Huxley. The sodium and potassium channels are modelled as variable resistor in series with a battery. The ion channels are connected in parallel with one-another and with the capacitor. 15

3.2 Hodgkin Huxley functions. **(A)** The steady state functions, $m_\infty(V), n_\infty(V)$ and $h_\infty(V)$, are plotted. **(B)** The time constants, τ_m, τ_n and τ_h are plotted. 18

3.3 Illustration of an action potential and the different phases characterized by changes to the conductances. 19

3.4 Depiction of a sequence of finite-compartmental representations of a pyramidal neuron with the last stage representing the neuron as a single compartment. Created in https://BioRender.com 22

4.1 Phase description for a limit cycle. *Left* Voltage trace showing the phase zero as the peak of the potential. *Right* Limit cycle Γ in the phase portrait with different points $(\theta = 0, \pi/2)$ corresponding to the spike times and half period $T/2$ of the time trace. 30

5.1 Three categories of symmetric cluster solutions that can arise for a periodic solution corresponding to identical phase differences between adjacent neurons. The nodes in each diagram represent a spiking neuron and how they are arranged in phase space from 0 to 2π **(A)** In-phase or the $1-$cluster solution in which all the neurons spike in unison with a 0 phase difference. **(B)** Splay-state or $N-$cluster solution, where each neuron forms its own cluster and no two neurons synchronize. $\psi = \frac{2k\pi}{N}$, with $gcd(k, N) = 1$ **(C)** $n-$cluster solution, win which the neurons selectively synchronize and organize into clusters C_i, defined by $\{i, i+n, \ldots, N-n+i\}$ for $i = \{1, 2, \ldots, n\}$. Neurons within each cluster C_i are synchronized with one another. In this case, $\psi = \frac{2\pi m}{n}$ as described in the main text. 43

5.2 Three types of coupling considered in our analysis. Each node in the ring diagram represents a neuron. These diagrams convey information about which neurons are coupled together via reciprocal synapses, indicated by the lines joining two nodes. For the nearest neighbours, each neuron i is coupled to its neighbours $i+1 \pmod N$ and $i-1 \pmod N$. In the other two cases each neuron is synaptically coupled to all of its neighbours. The black lines for the global homogeneous case represent identical synaptic weights. . . . 49

6.1 Reduced Traub-Miles with M-current 54

6.2 Synaptically coupled RTM model neurons 57

6.3 Bifurcation curves in (I_{app}, g_M) parameter space. *Left.* Full two-parameter bifurcation diagram *Right.* Zoomed-in view near the red curves, highlighting the region relevant to our analysis. 59

6.4 Steady states as a function of current (I_{app}) for the RTM model at two values of g_M, before and after the Bogdanov Takens point (B.T). The red curves indicate stable points and the black curves indicate unstable points. The green curves above and below the fixed-point curve (in black) correspond to the maximum and minimum voltages along the periodic orbits. **(A)** One parameter bifurcation curve for g_M before the BT point ($g_M = 0$) when the neuron is exhibiting type I dynamics or class I excitability. The oscillations are born via a saddle-node on an invariant circle. **(B)** The bifurcation curve for g_M after the B.T point, when the neuron is type II (or class II), oscillations are born via a Hopf bifurcation (labelled H.B). Although the limit points still exist, the branch of periodic solutions are emerging from the Hopf point rather than the limit point. Numerical limitations prevented us from demonstrating the connection between the blue lines. 60

6.5 Frequency-Current curves for the RTM model neuron at different values of g_M. **(A)** F/I curve at $g_M = 0$. The firing frequency can start at arbitrarily low values for I_{app} near 0 μA . This is a neuron with type I excitability. **(B)** F/I curve at $g_M = 5$. The firing frequency starts a finite value and has a relatively narrow range of values for the same range of applied currents. This is a neuron with type II excitability. 61

6.6 Simulations for a single reduced Traub Miles neuron evaluated at different values of the M-current conductance. Each panel displays three time series corresponding to a fixed g_M under the effect of different values of the applied current ($I_{app} = 1, 30, 60$ μA). **(A)**When g_M is set to 0 mS/cm^2, a periodic solution can be obtained by applying $1, 30, 60$ μA **(B)** When g_M is set to 2 mS/cm^2, a periodic solution can be obtained by applying $30, 60$ μA **(C)** When g_M is set to 5 mS/cm^2, a periodic solution can be obtained by applying $30, 60$ μA **(D)** When g_M is set to 10 mS/cm^2, a periodic solution can be obtained by applying 60 μA 62

7.1 H_{odd}, in Eq. (7.8), is plotted for **(A)** $g_M = 5$ and **(B)** $g_M = 0$. In both cases, $\psi = 0$ and $\psi = \pi$ are the only fixed points for a pair of weakly coupled RTM model neurons. The stability analysis is discussed in the main text . 69

7.2 **(A)** H_{odd}, in Eq. (7.8), is plotted for $g_M = 2$ and 3.13. The subplots show behaviour near 0 and π. In both cases, 0 and π are fixed points to the system. **(B)** When g_M is set to 3.13, the system also exhibits additional fixed points labelled 'a' (and 'f') and 'b' (and 'e') near 0 (near 2π) and $\frac{\pi}{2}$ (near $3\frac{\pi}{2}$) respectively. **(C)** When g_M is set to 2, the system also exhibits additional fixed points labelled 'c' and 'd' near π. 70

7.3 Schematic of voltage traces corresponding to an in-phase and anti-phase solution for a pair neurons 71

7.4 Numerical simulations for a pair of RTM neurons at different strengths of the M-Current, with g_{syn} set to 0.2. **(A)** The cells oscillate in anti-phase when g_M set to 0. **(B)** g_M is set to 2 and the cells oscillate in an out-of-phase solution,associated with a phase difference that is close to the equilibrium point 'c', identified in panel (C) of Figure 7.2. **(C)** g_M is set to 3.13 and the cells oscillate in an out-of-phase solution, associated with a phase difference close to the equilibrium solution 'b', identified in panel (B) of Figure 7.2. **(D)** The cells synchronize when g_M is set to 5. 73

7.5 Multiple stable cluster solutions obtained for a network of reduced Traub-Miles model neurons of sizes $N = 10, 12, 15$ and 24. In the network, cells are coupled to every other cell with equal synaptic weights ($k = \lfloor \frac{N}{2} \rfloor$,$p = 1$). In each illustration, nodes sharing the same colour represent neurons belonging to the same cluster. The voltage traces are presented for a **(A)** 4−cluster, **(B)** 6−cluster and **(C)** 5−cluster solutions. A stable 4−cluster solution is illustrated for a network of **(D)** 24 cells and **(G)** 12 cells, both associated with $\psi = \frac{\pi}{2}$. A stable 6− cluster is illustrated in a network of **(E)** 24 cells and **(H)** 12 cells, both associated with $\psi = \frac{\pi}{3}$. **(F)** A stable 5−cluster solution is illustrated for a network of 15 cells associated with $\psi = \frac{2\pi}{5}$. **(I)**A different stable 5−cluster is illustrated for a network of 10 cells with $\psi = \frac{8\pi}{5}$. The order of cluster firing is discussed in the main text. 80

7.6 Synchronization of a network of RTM model neurons, when g_M is set to 5. **(A)** The voltage trace associated with an in-phase solution. The in-phase solution is illustrated for a network of **(B)** 24 cells, **(C)** 15 cells, **(D)** 12 cells and **(E)** 10 cells through raster plots and node diagrams. 81

7.7 Multistability when g_M is set to 0, in a network of 24 RTM model neurons with globally homogeneous coupling. **(A)** The network is initialized in a stable 4−cluster with a firing order: $C_1 - C_2 - C_3 - C_4$, where $C_i = \{i, i+4, \ldots, 19+i\}$. **(B)** A transient perturbation, in the form a current pulse, applied to a subset of the cells alters the firing order to $C_1 - C_4 - C_2 - C_3$. **(C)** Applying the pulse to a different subset of cell, can switch the network to a stable 4−cluster solution where the cells belonging to C_2 and C_4 change to $\{2, 10, 12, 14, 22, 24\}$ and $\{4, 6, 8, 16, 18, 20\}$ resp. **(D)** The network is initialized in a stable 6−cluster with a firing order: $C_1 - C_2 - C_3 - C_4 - C_5 - C_6$, where $C_i = \{i, i+6, \ldots, 17+i\}$. **(E)** A transient perturbation, in the form a current pulse, applied to subset of the cells alters the firing order to $C_1 - C_2 - C_6 - C_3 - C_4 - C_5$. **(F)** Applying a perturbation to a different subset of cells can also switch the network to a stable 6−cluster solution where the cells belonging to cluster C_6, C_2 and C_4 change to $\{6, 11, 16, 18\}$,$\{2, 13, 20, 24\}$ and $\{4, 8, 10, 22\}$. **(G)** The perturbation can also switch the network to a stable 6−cluster solution where the cells belonging to cluster C_6, C_2 and C_4 change to $\{8, 10, 20, 22\}$,$\{2, 12, 14, 24\}$ and $\{4, 6, 16, 18\}$ and the firing order changes to $C_1 - C_2 - C_3 - C_6 - C_5 - C_4$. 83

7.8 Anti-phase ($\psi = \frac{\pi}{2}$) obtained for a network of 4 neurons equipped with all-all homogeneous coupling at $g_M = 0$, contradicting the phase model prediction in Table 7.9 84

7.9 A 3−cluster obtained for a network of $6, 12, 15$ and 24 neurons equipped with all-all homogeneous coupling at $g_M = 0$. The voltage trace for the solution is presented in **(A)**. A 3−cluster solutions are illustrated in a network of **(A)** 3 cells, **(B)**12 cells and **(E)** 24 cells, all associated with $\psi = 2\frac{\pi}{3}$. **(D)** A 3−cluster solution obtained for a network of 15 cells associated with $\psi = 4\frac{\pi}{3}$. 84

7.10 Demonstration of splay state solutions for RTM networks equipped with distance-dependent coupling ($p = 0.5, k = \lfloor N/2 \rfloor$) with g_M set to 5. **(A)** A splay solution for a network of 12 cells, spiking with a phase difference $\psi = \frac{\pi}{6}$. **(B)** A splay solution for 16 cells with a phase difference $\psi = \frac{\pi}{8}$. **(C)** A splay solution obtained for a network of 24 neurons with $\psi = \frac{\pi}{12}$. In each case, the cells fire in the order of $1 - 2 - 3 - \cdots - N$ as illustrated through the raster plots. 93

7.11 Multistability in a network of RTM model neurons, equipped with global distance dependent coupling ($p = 0.5$), when g_M is set to 0. In each case, the network is initialized in a stable cluster solution and a transient perturbation is applied to a subset of the cells during time $t \in [8000, 8050]$. **(A)** Network of 8 cells is initialized in a stable 4−cluster solution $\left(\psi = \frac{\pi}{2}\right)$. **(B)** The perturbation reverses the firing order of the spiking cells from (A), switching the network to a different stable 4−cluster solution $\left(\psi = 3\frac{\pi}{2}\right)$. **(C)** A perturbation applied to a different subset of cells, can switch the initial state in (A) to a stable 8−cluster $\left(\psi = 7\frac{\pi}{4}\right)$. **(D)** Network of 24 cells is initialized in a stable 4−cluster solution $\left(\psi = \frac{\pi}{2}\right)$. **(E)** The perturbation switches the network in (D) to a different stable 4−cluster solution $\left(\psi = 3\frac{\pi}{2}\right)$ **(F)** The network in (D) can also switch to a stable 8−cluster $\left(\psi = 7\frac{\pi}{4}\right)$. 94

7.12 Multistability in a network of RTM model neurons with g_M set to 5, and with globally heterogeneous synaptic weights. A transient perturbation is applied during time $t \in [8000, 8050]$ to a network initialized in a stable splay solution. **(A)** Network of 12 cells, initialized in a stable splay solution $\left(\psi = \frac{\pi}{6}\right)$, synchronizes when 6 of the cells are perturbed transiently. **(B)** Network of 16 cells, initialized in a stable splay solution $\left(\psi = \frac{\pi}{8}\right)$, synchronizes when 8 of the cells are perturbed transiently. **(C)** Network of 24 cells, initialized in a stable splay solution $\left(\psi = \frac{\pi}{12}\right)$, synchronizes when 12 of the cells are perturbed transiently. 95

7.13 Demonstration of transitions between cluster solutions for a network of RTM model neurons, equipped with nearest neighbours coupling, with g_M set to 0. In this case, the network is initialized in a stable cluster solution as predicted by the phase model, and under the transient current pulse, it will switch to a symmetric cluster solution where the phase differences between adjacent cells are heterogeneous. **(A)** A network of 12 cells is initialized in an anti-phase solution with each cluster C_i defined by $\{i, i+2, \ldots, N-2+i\}$ for $i = \{1, 2\}$. Applying a transient pulse can switch it to a $4-$cluster solution with clusters C_i defined by $\{i, i+4\}$ for $i = \{1, 2, 3, 4\}$ and a firing order: $C_1 - C_4 - C_2 - C_3$.**(B)** A network of 24 cells is initialized in an anti-phase solution with each cluster C_i defined by $\{i, i+2, \ldots, N-2+i\}$ for $i = \{1, 2\}$. Applying a transient pulse can switch it to a $4-$cluster solution with clusters C_i defined by $\{i, i+4\}$ for $i = \{1, 2, 3, 4\}$ and a firing order: $C_1 - C_3 - C_2 - C_4$. **(C)** A network of 12 cells is initialized in a stable $4-$cluster associated with $\psi = \frac{\pi}{2}$. The transient pulse changes the firing order from $C_1 - C_2 - C_3 - C_4$ to $C_1 - C_4 - C_2 - C_3$. **(D)** A network of 12 cells is initialized in a stable $4-$cluster associated with $\psi = \frac{\pi}{2}$. The transient pulse changes the firing order from $C_1 - C_2 - C_3 - C_4$ to $C_1 - C_4 - C_2 - C_3$. 96

7.14 Splay states are obtained for a network of RTM model neurons, equipped with nearest neighbour coupling, with g_M set to 5. The solutions are presented in a similar format as Figure C.7. **(A)** A network of 5 cells spike individually corresponding to a $5-$cluster solution with $\psi = \frac{2\pi}{5}$. **(B)** A network of 7 cells exhibiting a $7-$cluster solution with $\psi = \frac{12\pi}{7}$. 100

7.15 Multiple stable $n-$clusters are obtained for a network RTM model neurons, coupled in a nearest neighbour fashion, with g_M set to 5. The solutions for $n = 6, 8$ and 12 are presented in a similar format as Figure C.6. **(A)-(C)** display the representative voltage traces for each $n-$cluster. Panels **(D)** and **(G)** illustrate the $6-$cluster solution in a network of 12 and 24 cells resp, with $\psi = \frac{\pi}{3}$. Panels **(E)** and **(H)** demonstrate the $8-$cluster solution in a network of 8 and 24 cells resp with $\psi = \frac{\pi}{4}$. Panels **(F)** and **(I)** illustrate the $12-$cluster in a network of 12 and 24 cells resp, with $\psi = \frac{\pi}{6}$ 102

7.16 Demonstration of multistablity in a network of 300 model RTM neurons equipped with nearest neighbours coupling ($k = 1$), with g_M set to 0. Rasters are plotted for each $n-$cluster solution along with a sub-figure which displays the first n cells in the network. **(A)** Network exhibiting an anti-phase solution with two clusters formed. **(B)** A $3-$cluster solution is obtained with $\psi = \frac{2\pi}{3}$. **(C)** A $5-$cluster solution is obtained with $\psi = \frac{6\pi}{5}$. **(D)** A $15-$cluster solution obtained with $\psi = \frac{14\pi}{15}$ 103

7.17 Demonstration of multistablity in a network of 300 model RTM neurons equipped with nearest neighbours coupling ($k = 1$), with g_M set to 5. Rasters are plotted for each $n-$cluster solution along with a sub-figure which displays the first n cells in the network. **(A)** Network exhibiting an $5-$cluster solution corresponding to $\psi = \frac{2\pi}{5}$. **(B)** A $6-$cluster solution obtained for the network with $\psi = \frac{\pi}{3}$. **(C)** A $12-$cluster solution is obtained with $\psi = \frac{\pi}{6}$. **(D)** A $15-$cluster solution is obtained with $\psi = \frac{2\pi}{15}$ 104

7.18 Demonstration of possible transitions between stable cluster solutions when g_M is set to 5, for a network of 24 RTM model neurons, equipped with nearest neighbour coupling. **(A)** The network is initialized in a stable $6-$cluster solution ($\psi = \frac{\pi}{3}$) **(B)** A transient perturbation applied to a subset of cells in the network, can switch it to a stable $12-$cluster solution associated with $\psi = \frac{\pi}{6}$ **(C)** The network is initialized in a stable $8-$ cluster solution associated with $\psi = \frac{\pi}{4}$. **(D)** The network is initialized in a stable $12-$ cluster solution associated with $\psi = \frac{\pi}{6}$. **(E)** A transient perturbation applied to subset of the cells in the network initialized in (A), (C) or (D), can switch them individually into a stable $24-$ cluster solution. **(F)** A transient perturbation applied to a different subset of the cells in the network initialized in (A), (C) or (D), can synchronize them. 106

7.19 Stability analysis for nearest neighbours determined by the sign of H'_{odd} on $[0, \pi]$ for different values of g_M. In each panel, unstable regions are highlighted in red, while stable regions are shown in green. **(A)** When g_M is set to 0, around $\psi = 1.046$, H'_{odd} changes its sign from negative to positive, and the corresponding solution becomes stable. **(B)** When g_M is set to 2, the corresponding H'_{odd} changes sign twice, around $\psi = 0.9131$ and 2.8321. **(C)** At $g_M = 5$, it is essentially a reverse picture of $g_M = 0$, and H'_{odd} becomes negative around $\psi = 1.6506$, beyond which the corresponding cluster solutions are unstable. 107

C.1 Interaction function for the reduced Traub-Miles model (7.7) evaluated at four distinct values of the M-current maximal conductance, g_M. We compare the different approximations in each case using 2, 10 and 30 terms. **(A)** g_M is set to 0 **(B)** g_M is set to 2 **(C)** g_M is set to 3.13 **(D)** g_M is set to 5 . . . 135

C.2 Multistability when g_M is set to 0, in a network of 12 RTM model neurons with globally homogeneous coupling. **(A)** The network is initialized in a stable 4−cluster with a firing order: $C_1 - C_2 - C_3 - C_4$, where $C_i = \{i, i+4, \ldots, 7+i\}$. **(B)** A transient perturbation, in the form a current pulse, applied to a subset of the cells alters the firing order to $C_1 - C_4 - C_2 - C_3$. **(C)** Applying the pulse to a different subset of cell, can switch the network to a stable 4−cluster solution where the cells belonging to C_2 and C_4 change to $\{2, 6, 12\}$ and $\{4, 6, 8\}$ resp. **(D)** The network is initialized in a stable 6−cluster with a firing order: $C_1 - C_2 - C_3 - C_4 - C_5 - C_6$, where $C_i = \{i, i+6, \ldots, N-6-i\}$. A transient perturbation, in the form a current pulse, applied to different subset of the cells alters the firing order to **(E)** $C_1 - C_6 - C_4 - C_2 - C_5 - C_3$ and **(F)** $C_1 - C_6 - C_2 - C_4 - C_5 - C_3$. 136

C.3 Multistability when g_M is set to 0, in a network of 15 RTM model neurons with a globally homogeneous coupling. **(A)** The network is initialized in a stable 5− cluster solutions with a firing order $C_1 - C_2 - C_3 - C_4 - C_5$, where $C_i = \{i, i+5, i+5\cdot 2, \ldots, 10+i\}$, for $i = \{1, 2, 3, 4, 5\}$. **(B)** A transient perturbation applied to a subset of the cells in the network can alter the firing order of to $C_1 - C_2 - C_5 - C_3 - C_4$. **(C)** A transient perturbation applied to a different subset of cells, can alter both the firing order from (A) and the arrangement of the cells in each cluster. The new clusters are given by: $C_1 = \{1, 9, 11\}$, $C_2 = \{2, 7, 15\}$, $C_3 = \{3, 5, 10\}$, $C_4 = \{4, 12, 14\}$ and $C_5 = \{6, 8, 13\}$. The new firing order is given by: $C_1 - C_2 - C_5 - C_4 - C_3$. 137

C.4 Multistability in a network of reduced Traub-Miles model neurons (RTM) equipped with a monotonic globally heterogeneous coupling ($p = 0.5$, $k = \lfloor N/2 \rfloor$), with g_M set to 0. The solutions are presented through voltage traces, raster plots and ring diagrams to illustrate the spike timing and coupling architecture, respectively. Each node in the ring represents a spiking cell. Nodes sharing the same colour belong to the same cluster. Voltage trace representations are presented for **(A)** anti phase, **(B)** 3−cluster and **(C)** 8−cluster solutions. **(D)** Anti-phase solution ($\psi = \pi$) obtained for a network of 8 cells **(G)** Anti-phase solution for a network of 24 cells. **(E)** 3−cluster solution for a network of 6 cells $\left(\psi = \frac{2\pi}{3}\right)$. **(H)** 3−cluster solution for a network of 24 cells associated with $\left(\psi = \frac{2\pi}{3}\right)$. **(F)** 8−cluster solution obtained for a network of 8 cells **(I)** 8−cluster solution $\left(\psi = \frac{3\pi}{4}\right)$ obtained for a network of 16 cells. The cluster firing order is discussed in the main text. 141

C.5 Multistability in a network of 12 RTM model neurons equipped with distance dependent coupling ($p = 0.5, k = 6$) with g_M set to 0. A transient perturbation is applied to a subset of the cells for time $t \in [8000, 8050]$. **(A)** The network is initialized in a stable $4-$cluster solution corresponding to an inter-cluster phase difference of $\psi = \frac{\pi}{2}$. **(B)** The perturbation reverses the firing order of the solution from (A), switching the network to a different stable $4-$cluster solution $\left(\psi = 3\frac{\pi}{2}\right)$. **(C)** A transient perturbation applied to a different subset of cells can switch the network in (A) to a stable $12-$cluster solution associated with a inter-cell phase difference of $\psi = 5\frac{\pi}{6}$. **(D)** The perturbation can also switch the network in (A) to a $12-$cluster associated with $\psi = 7\frac{\pi}{6}$. 142

C.6 Demonstration of multistablity within a network of RTM model neurons, equipped with nearest neighbour coupling and g_M set to 0. **(A)-(C)** display the voltage traces for each solution. The solutions are presented in two ways: Ring diagrams depicting the *nearest neighbour coupling* and the cells belonging to the same cluster (identified by the same colouring), and raster plots which display the firing order of the clusters. **(D),(G)** and **(J)** illustrate the anti-phase solutions for a network of 4, 8 and 24 cells resp. **(E),(H)** and **(K)** are the $3-$ cluster solutions for 6 ($\psi = \frac{2\pi}{3}$),15($\psi = \frac{4\pi}{3}$) and 24 ($\psi = \frac{2\pi}{3}$) cells resp. **(F),(I)** and **(L)** are the $5-$ cluster solutions for a network of 5($\psi = \frac{4\pi}{5}$) ,10($\psi = \frac{2\pi}{5}$) and 15($\psi = \frac{6\pi}{5}$) cells resp. The cluster ensembles and the order in which they fire are discussed in the main text. 143

C.7 Splay solutions are obtained for a network of RTM model neurons equipped with nearest neighbour coupling and with g_M set to 0. The solutions are presented in three ways: Voltage traces, Ring diagrams depicting the coupling architecture, and raster plots which tell us which cells fire when in a single cycle. **(A)** A splay state obtained for a network of 4 cells, corresponding to $\psi = \frac{\pi}{2}$. **(B)** A splay state obtained for a network of 7 cells, with $\psi = \frac{8\pi}{7}$. **(C)** A splay state obtained for 9 cells with $\psi = \frac{8\pi}{9}$. The cluster ensembles and the order in which they fire are discussed in the main text. 144

C.8 Demonstration of the possible transitions of a network, equipped with nearest neighbour coupling, initialized in a stable 3−cluster solution, when g_M is set to 0. **(A)** A network of 12 neurons is initialized in a stable 3−cluster solution associated with $\psi = 2\frac{\pi}{3}$. A transient perturbation, in the form of a current pulse, applied to a subset of cells in the network, can switch it to a **(B)** stable 3−cluster solution with the reverse firing order associated with $\psi = 4\frac{\pi}{3}$, or **(C)** a stable 12−cluster solution (splay) associated with $\psi = 5\frac{\pi}{6}$, or **(D)** an anti-phase solution ($\psi = \pi$). **(E)** A network of 24 neurons is initialized in a stable 3−cluster solution associated with $\psi = \frac{2}{\pi}3$. A transient perturbation, in the form of a current pulse, applied to a subset of cells in the network, can switch it to a **(F)** stable 12−cluster solution associated with $\psi = 7\frac{\pi}{6}$, or **(G)** a stable 12−cluster solution (splay) associated with $\psi = 5\frac{\pi}{6}$, or **(H)** an anti-phase solution ($\psi = \pi$). 145

C.9 Demonstration of synchrony within a network of RTM model neurons equipped with nearest neighbour coupling, when g_M is set to 5, obtained through transient current pulses applied to an initialized network, equipped with nearest neighbour coupling. **(A)** A network of 8 cells, initialized in a splay state ($\psi = \frac{\pi}{4}$) , can synchronize under the transient perturbation applied to a subset of the cells in the network (labelled initial and final respectively). A network of 12 cells is initialized in a **(B)** stable splay state ($\psi = \frac{\pi}{6}$), and a **(C)** stable 6− cluster solution ($\psi = \frac{\pi}{3}$) **(D)** A transient perturbation applied to a subset of the cells in the network, initialized in (C) and (D), can synchronize the network. 146

List of Tables

6.1 Description of the ionic currents in Eq. (6.1) 63

6.2 Kinetics for the rate functions. 63

6.3 Kinetics for the M-current. 63

6.4 Parameters for Eq. (6.18) 63

6.5 Parameter values for phase model analysis 63

7.1 Phase model predictions for a pair of RTM model neurons at different values of g_M $(= \{0, 2, 5\})$. 72

7.2 Neuronal behaviour at different Levels of ACh 75

7.3 Phase model predictions for $n-$ clusters $(n = \{1, .., 15\})$ across different values of g_M in a network with *global homogeneous coupling*. The solutions that were verified numerically are marked with a *. 77

7.4 μ_j for $n = 2$ 82

7.5 μ_j for $n = 3$ 82

7.6 Evaluation of the derivative of the interaction function, H at $0, \pi, 2\frac{\pi}{3}$ and $4\frac{\pi}{3}$ under increasing number of Fourier terms used in the approximation. . 85

7.7 Phase model predictions across different values of $g_M = \{0, 2, 5\}$ in RTM networks equipped with *distance-dependent coupling with* $p = 0.5$. 89

7.8 Phase model predictions across different values of $g_M = \{0, 2, 5\}$ in RTM networks equipped with *distance-dependent coupling with* $p = 0.5$.. *Continuation from Table 7.7* 90

7.9 Phase model predictions for selected ψ across different values of $g_M (= \{0, 2, 5\})$ in a network with nearest neighbour coupling. 99

C.1 Period of the limit cycles exhibited by the RTM model neuron corresponding to different values of g_M 134

Chapter 1

Introduction

The study of synchronization within neural networks is crucial for understanding how different regions of the brain communicate and coordinate on both local and global scales. In particular, groups of neurons may transiently synchronize to form spatiotemporal patterns of activity, which serve as a mechanism for encoding information. The hippocampus is a critical structure in the brain responsible for the formation of episodic memories—memories relating to the events from one's personal life [14]. An example of an episodic memory, could include remembering what you may have for breakfast yesterday, or where you were on your birthday last year. These type of memories are believed to be encoded as distinct patterns of neuronal activity and stored in the CA3 region of the hippocampus, where they can later be retrieved in response to partial cues [48, 50].

A network of spiking neurons can organize into such distinct patterns by forming 'neural assemblies'—groups of neurons that transiently synchronize their activity. Through this synchrony, they are often proposed as a mechanism underlying the generation of distinct brain rhythms, which are commonly observed in electroencephalogram (EEG) recordings. Neural assemblies observed in the hippocampus, are thought to facilitate spatial navigation tasks and, the encoding and storage of episodic memories [57, 27, 110, 121]. It is also theorized that, in addition to external inputs, the intrinsic oscillatory dynamics of the hippocampus can also play a role in the formation of neural assemblies [57, 110] . An important input that affects the hippocampal dynamics is acetylcholine—a neuromodulator known for its vital role in cognitive functions, particularly those involving learning and memory [61, 63, 62]. It is believed that different levels of ACh may be linked to distinct brain rhythms, belonging to a specific frequency band, which emerge during different physiological states (wakefulness and sleep) [73]. A generally accepted consensus, is that high levels of ACh during active exploration and rapid eye movement (REM) sleep, sup-

port the encoding of new stimuli, while low levels of ACh during quiet waking and slow wave sleep (SWS), facilitate the consolidation of previously formed memories for future recall [63, 64, 60, 58, 73, 43]. In the present thesis, we investigate this bidirectional role of acetylcholine (ACh) in neural assembly formation, specifically studying the distinct neural assemblies that may be supported by a network of pyramidal neurons in the CA3 region of the hippocampus, under varying levels of ACh (high vs. low).

Mathematically, neural assemblies are reminiscent of cluster solutions for a given biophysical network of model neurons, which are often suggested as a mechanism for assembly formation [46]. In particular, by imposing symmetries in the coupling architecture of the network, we can study model-independent cluster solutions, where the inter-cluster phase differences are identical. The resulting solutions are symmetric, in the sense that each cluster harbours an identical number of neural oscillators. To study these types of solutions, we derive a phase model approximation of the biophysical network—an approach that has been used previously to investigate cluster solutions in networks of weakly coupled oscillators [106, 33, 88, 87, 97, 15, 120, 98]. A phase model approximation can simplify a high-dimensional biophysical neuron model to a simpler model while retaining essential dynamical features required to study neural synchrony [45]. In the present thesis, we impose a circulant form of coupling, such that the corresponding biophysical network satisfies periodic boundary conditions—effectively arranging the identical model neurons along a one-dimensional ring. Phase model analysis has been used to derive the conditions of existence and stability of symmetric cluster solutions for such networks under various coupling architectures, including all-to-all coupling with a globally homogeneous [106, 15], and symmetric heterogeneous distribution [15, 97, 120] of synaptic weights. We apply these results to a homogeneous network of conductance based model pyramidal neurons coupled via weak excitatory synapses, under varying levels of ACh, and consider three coupling configurations: all-to-all globally homogeneous, symmetric distance-dependent and nearest-neighbours coupling.

Acetylcholine acts as a neuromodulator by altering the neuronal behaviour at both the cellular and network levels. In particular, at the cellular level, acetylcholine can suppress [55] a slow, voltage-dependent, non-inactivating potassium current [36] found in hippocampal cells [12] known as the muscarinic current (M-current). Based on the response to input current, Hodgkin classified neurons into two types: Class I and Class II [66]. The work in this present thesis is primarily inspired by the results of a paper [4], where an M-current induced bifurcation in a general biophysical neuron model (that incorporates an M-current) is linked to a switch in the neuronal excitability from Class I to Class II dynamics. They applied their results to various neuron models coupled with excitatory synapses and demonstrated an M-current induced transition from anti-phase solutions (Class I excitability, no

M-current) to in-phase synchrony (Class II excitability, high M-current), through intermediary out-of-phase solutions (intermediate strengths of M-current). This result aligns with prior studies of pairs of model neurons weakly coupled together with an excitatory synapse and either Class I or Class II excitability [56, 29]. The effects of M-current on synchronization, have been extensively studied, both experimentally and computationally. The phase response curve (PRC), which is an experimentally obtainable measure, can be used to characterize the synchronization properties of a neuron [136, 56]. Experimental studies have demonstrated changes in the shape and type of the phase response curves (PRC) associated with cortical pyramidal neurons, primarily driven by the M-current, which have then been simulated for different neuron models [125, 126, 127]. Computational papers have also studied specific network level implications of the M-current induced switch in neuronal dynamics [72, 39, 40, 116, 80, 137, 117, 89]. In particular, [39] analyzes the combined effect of increased firing frequencies and the M-current on the ability of an excitatory pyramidal network to synchronize. However, to our knowledge, these works do not systematically explore the manner in which the hippocampal network undergoes de-synchronization, when the M-current is suppressed, as it would in the presence of acetylcholine. A network consisting of spiking neurons may desynchronize, by organizing themselves into neural assemblies. In [31], they demonstrate a desynchronization of an all-to-all coupled 5− cell network, into a splay state through the suppression of M-current. In [9, 116, 80, 117], the desynchronization is studied as travelling wave solutions or considered to be generally asynchronous states. Our work in this thesis, aims to further explore the de-synchronization within the network, by studying the corresponding cluster solutions under different coupling configurations, using a phase model approach. Additionally, we examine the possible desynchronized states in each case in the presence of M-current, associated with low levels of ACh, and compare them to those arising under high ACh conditions.

The layout of this thesis is as follows. In Chapter 2, we provide the necessary background in biology, reviewing the structure of the brain and the underlying components responsible for its function. In particular, we introduce the hippocampus, which is the structure of interest in our work. In Chapter 3, we review relevant mathematical concepts in neuroscience; particularly, methods used to model the behaviour of neurons and synaptic transmission in the hippocampus. We provide a description of the cellular properties by which individual neurons generate electrical activity and how we can model the underlying dynamics. We also describe how bifurcation theory is used to classify the excitability of a neuron and the factors that can affect it. We conclude this chapter by reviewing models on synaptic transmission in order to build networks of model neurons that are coupled together through a chemical synapse. In Chapter 4, we describe the phase model reduction of a general high-dimensional conductance-based model neuron to a simpler one-dimensional

model which preserves the relevant dynamical features needed to study neural synchrony. In Chapter 5, we describe how we can use this phase model reduction to study the cluster solutions of a biophysical network of conductance-based model neurons equipped with a circulant form of coupling architecture. In particular, we review the existence and stability conditions for networks equipped with an all-to-all globally homogeneous, symmetric distance-dependent and nearest-neighbours type of coupling. In Chapter 6, we describe a single-compartment model of an excitatory hippocampal pyramidal neuron with an M-current, which is a reduction due to [108] of a detailed model developed by Traub and Miles [131]. We also perform a bifurcation analysis of this model to demonstrate the M-current induced switch in neuronal excitability, and propose model parameters that are appropriate for our study using the phase model reduction. In Chapter 7, we present our results. We describe a phase model approximation of the RTM model neuron using parameters determined in the previous chapter, along with the stability analysis of various cluster solutions, under different strengths of the M-current, and the different coupling configurations of the corresponding network. Finally in Chapter 8, we summarize our work and discuss how our results may fit in the narrative of the cholinergic modulation of hippocampal dynamics. We discuss the limitations of our work as well as future directions that could be taken based on this work.

Chapter 2

Biological Background

The nervous system is a collection of cells responsible for coordinating activities that enables an organism to interact with its environment. It is composed of two parts: the central nervous system (CNS), consisting of the brain and spinal cord, and the peripheral nervous system (PNS) [65, 26], comprising spinal and cranial nerves, that branch out from the spinal cord and brain respectively. In vertebrates, the nervous system is highly centralized—all higher neural functions originate in the brain [26].

2.1 Anatomy of the brain

The brain can be broadly divided into three main components: the *cerebrum*, *cerebellum* and the *brain stem*. The outermost surface of the cerebrum and cerebellum is coated by a layer of heavily wrinkled tissue known as the cortex [77]. In mammals, complex functions like information processing are localized within the cerebral cortex. The cortex is dorsally divided into two hemispheres—a left and a right hemisphere—each of which is further divided into four anatomically distinct lobes: *frontal*, *parietal*, *occipital* and *temporal lobes*. Each lobe can be associated with specific neural functions. For example, the frontal lobes are primarily responsible for planning movement as well as critical thinking, while the occipital lobes, located at the back of the brain, are responsible for the processing of visual stimuli [77]. The temporal lobes, located by the ears, in front of the occipital lobes and beneath the frontoparietal lobes, are largely concerned with the processing of auditory stimuli [26]. They also consist of sub-cortical structures—*hippocampus* and the *amygdaloid*—responsible for aspects of learning, memory, and emotion [77]. The location of the hippocampus in the brain is illustrated in Figure 2.1.



Figure 2.1: A schematic of the hippocampus (highlighted in red) within the temporal lobe of the brain (highlighted in yellow). Created in https://BioRender.com

The brain, like all organs of the body, is composed of discrete cellular elements. Two main types of cells make up the brain: neurons and glia. Glial cells play a supportive role by supplying energy and structural stability to brain tissue [65]. Glial cells are outside of the scope of this thesis, we will focus only on neurons.

2.1.1 Neuron morphology and physiology

Neurons are the functional units of the brain, responsible for processing and transmitting information. All neurons share the same basic architecture as illustrated in Figure 2.2, consisting of a cell body or *soma* and two types of cytoplasmic extensions: a long and unbranched *axon*, and a group of shorter, tree-like branched extensions called *dendrites* [77]. In general, the morphology and organization of these components can vary among neurons, thereby characterizing different types of neurons. For example, pyramidal neurons—named after their pyramid-shaped soma—have multiple dendrites that branch extensively from both the base and apex of the soma [90], along with a long, thick axon that extends from the soma.

The cellular composition of a neuron is, for the most part, no different than a standard mammalian cell. Neurons have a cytoplasm that is bounded by a *cell membrane* that is made up of a lipid bilayer. The cell membrane separates ions between the extracellular and the intracellular fluids while allowing small and non-polar molecules, like oxygen, to pass

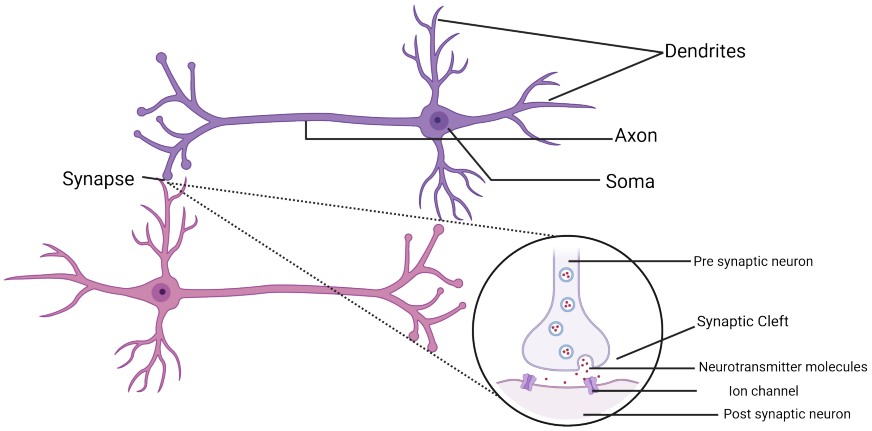


Figure 2.2: Schematic illustrating the structure of a typical pyramidal neuron, consisting of a soma, dendrites, and an axon. A chemical synapse between two neurons is also shown. Created in https://BioRender.com

through [90]. The soma contains a nucleus and cellular organelles that facilitate protein synthesis and other cellular functions [65]. Unlike most other mammalian cells, various voltage-gated protein channels are embedded in the cell membrane of neurons. These channels, also known as *ion channels*, regulate the flow of ions into and out of the neuron.

Action potential

Neurons carry and encode information by means of electrical signals called *action potentials*, which are large, transient changes in the electrical potential across the cell membrane. This will be explained in more detail in the next chapter. Action potentials are initiated at the initial segment of the axon, known as the *axon hillock*, and propagates all the along the axon to its endpoints, the *axon terminals* [90]. At the terminals, action potentials can trigger a series of complex biochemical events that facilitate the transmission of signals to neighbouring neurons via their dendrites.

2.1.2 Synapse

The point at which two neurons communicate is known as a *synapse* [77]. Accordingly, the neuron transmitting the signal is called the *presynaptic neuron*, while the receiving neuron

is called the *postsynaptic neuron.* On each cell, an average of hundreds or even thousands of synapses are formed [26].

Signals can be transmitted through *chemical synapses*, mediated by the release of chemicals, or *electrical synapses*, mediated by gap junctions [90]. Most synaptic contacts in the brain, including those we encounter in our work, are chemical [26]. At a chemical synapse, the region separating the presynaptic cell and the postsynaptic cell is called the *synaptic cleft.* A substance known as a *neurotransmitter* is released from the presynaptic terminals and diffuses across the narrow cleft toward the postsynaptic cell. Neurotransmitters are typically synthesized in the presynaptic neuron and stored in tiny spherical packets called *synaptic vesicles*, located in the axon terminals [77]. When an action potential arrives at the presynaptic terminal, it causes calcium to enter the terminal, which in turn causes the vesicles to fuse with the cell membrane [36]. The 'docked' vesicles then release the neurotransmitter molecules into the synaptic cleft, which diffuse across the cleft and bind to specific receptor proteins on the postsynaptic membrane [26].

The interaction between a receptor and its corresponding neurotransmitter typically increases (excites) or decreases (inhibits) the likelihood of the postsynaptic neuron generating an action potential. This depends on the type of receptor found on the postsynaptic membrane. The primary excitatory neurotransmitter in the brain is *glutamate* which stimulates two receptors: *2-amino-3-hydroxy-5-methylisoxazol-4-propanoic acid (AMPA)/Kainate* and *N-methyl-D-asparate (NMDA)* [36]. On the contrary, *γ-Aminobutyric Acid (GABA)* is an inhibitory neurotransmitter found in most interneurons [90], which stimulates two receptors: GABA_A and GABA_B [36]. GABA_A and AMPA receptors are *ionotropic*, meaning neurotransmitter binding directly alters ion channels, leading to changes in membrane potential. In contrast, GABA_B receptors are *metabotropic*, with neurotransmitter binding initiating secondary processes that eventually affect ion channel activity, and subsequently neuronal excitability [77].

Another neurotransmitter of significance, is *acetylcholine (ACh)*, which was first discovered and chemically isolated from the vagus nerve of an isolated frog heart [90]. Acetylcholine plays different roles in different parts of the nervous system. In the brain, ACh tends to act as a neuromodulator that can alter cellular properties of neurons, which in turn affect affect network behaviour. It is found in areas such as the basal forebrain and the medial septum [128]. ACh can stimulate *ionotropic nicotinamide receptors (nAChR)* and *metabotropic muscarinic receptors (mAChR)*, both of which increase the neuron excitability [77]. In this thesis, we study the indirect effect of ACh, through its action on muscarinic receptors found in hippocampal pyramidal neurons [16, 28].

2.2 Hippocampus

The hippocampus (HPC) is a subcortical structure located in the ventral part of the medial temporal lobe of the brain. Its curved shape resembles that of a seahorse, which is reflected in its name—"hippocampus", derived from the Greek word for seahorse. The hippocampus plays a critical role in spatial navigation (building a mental map of the environment) and contextual learning [107, 105, 103, 48]. It is especially essential for the formation, storage, and retrieval of *episodic memories*—also known as *autobiographical memories*—which involve the conscious recollection of events from one's past [124, 122, 14, 119]. It should be noted that surrounding structures in the temporal, frontal and parietal lobes have also been implicated in memory processes, but are outside the scope of our work [99, 18].

2.2.1 Hippocampal structure

The hippocampus is primarily composed of an excitatory pyramidal cell layer, along with inhibitory GABAergic interneurons and excitatory granule cells. Based on cell distribution and function, the hippocampus can be broadly divided into two distinct regions: dentate gyrus (DG) and the cornu ammonis regions (CA1, CA2 , CA3 and CA4)[1]. Together with the entorhinal cortex, these regions form a relatively simple neural circuit, known as the *trisynaptic pathway*, which is the main information-processing circuit in the hippocampus [14]. A schematic of the pathway is illustrated in Figure 2.3, for reference.

The entorhinal cortex (EC) serves as the primary input into the hippocampus, receiving information from multiple cortical and sub-cortical regions [132]. The pathway between the EC and the hippocampus, known as the *perforant path*, contains axonal outputs from the pyramidal and granule cells of the EC [101], which primarily synapse onto the dentate gyrus granule cells. EC is involved in preprocessing and selectively filtering incoming signals, before they are directed into the hippocampus [78]. The DG further processes the incoming signals, before sending them to the CA3 region [48, 85, 49, 42], via the *mossy fiber (MF) pathway*. This pathway contains the axonal output of the DG granule cell, and their synaptic connections with the dendrites of CA3 pyramidal neurons.

The CA3 region is densely packed with pyramidal neurons that have many excitatory synapses with each other, forming what is often referred to as an *auto-associative network*

[1]The CA2 and CA4 are relatively narrow regions sharing similar characteristics with the CA3 region. It is sometimes included as a part of CA3. Details are not provided in this thesis, due to its irrelevance in our work.

[48].

The branches of the axons that form connections within the CA3 region, are called the *recurrent collaterals* [101]. The recurrent collaterals are activated via the perforant pathway during a memory retrieval process known as pattern completion [119, 109, 86], in which stored patterns of information are retrieved based on partial or incomplete inputs [14]. A key anatomical feature of the CA3 network is its relatively homogeneous appearance, with no prominent variation in neuronal shape or size [101]. This region has also been linked to the efficient storage of memories, where a single CA3 pyramidal cell can be involved in distinct representations of multiple memories [119]. The axons of CA3 pyramidal cells further branch out and project onto the dendrites of CA1 pyramidal cells. These branches are referred to as *Schaeffer collaterals* [14]. Within this neural circuit, GABAergic interneurons project to all the principal excitatory neurons (pyramidal and granule cells) [14], providing inhibition to prevent runaway excitation. The primary output of the hippocampus emerges from the CA1 region via the EC, and projects back to cortical regions of the brain. Projections also emerge from the CA3 region to sub-cortical structures [132].

It is worthwhile to note that the trisynaptic pathway is a unidirectional circuit; that is, the CA1 pyramidal cells do not project back into the CA3, nor do the CA3 project into the DG granule cells [101]. In addition to the intrinsic synaptic pathways, modulatory pathways from distal regions of the brain, directly project into the hippocampus, making synaptic connections with the excitatory neurons [14]. The four main extrinsic modulatory inputs into the hippocampus are acetylcholine (ACh), norepinephrine, dopamine, and serotonin [90].

2.2.2 Acetylcholine as a neuromodulator for the hippocampus.

The entire hippocampus is innervated by long cholinergic projection fibers [2] emerging from several regions of the basal forebrain [79, 91, 53] and the medial septal nucleus of the brain stem [112], through which acetylcholine (ACh) is released. As discussed in Section 2.1.2, ACh acts as a neuromodulator, altering both neuronal excitability and synaptic transmission [77], which can, in turn affect behaviour at the network level. ACh can stimulate both ionotropic nicotinic (nAChR) and metabotropic muscarinic receptors (mAChR) [128]. In the hippocampus, cholinergic receptors are predominantly muscarinic [128].

[2] Axon terminals that release Acetylcholine. Associated neurons that synthesize ACh are referred to as cholinergic neurons.

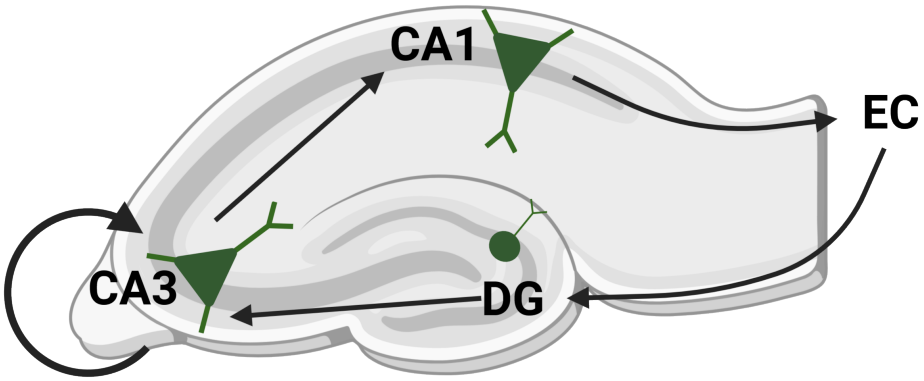


Figure 2.3: Schematic of the trisynaptic circuit in the hippocampus which is the main information pathway. In the present thesis, we study the auto-associative network of the CA3 region. *Note: Inhibitory interneurons not shown.* Created in https://BioRender.com

At the cellular level, ACh has been shown to indirectly increase the tendency of neurons to fire repetitive action potentials [55, 93], through its action on the metabotropic muscarinic receptors [55, 12], expressed in hippocampal pyramidal cells [16, 28]. Cholinergic excitation can also cause pyramidal neurons to be highly susceptible to incoming signals [55, 62, 63]. A blockade of cholinergic receptors has been demonstrated to selectively impair the encoding of new memories, but not the retrieval of previously formed memories [47, 100, 96]. This suggests that the activation of cholinergic receptors, mediated by high levels of ACh, could support the encoding of novel stimuli [63, 64], during which feedforward transmissions involving the EC-DG-CA3 pathway are enhanced [64, 58]. Meanwhile, low levels of ACh, causing little to no receptor activation, can facilitate the consolidation of newly encoded memories [63, 59, 114, 43] .

At the network level, ACh has been linked to the induction of oscillations that share common frequencies with the theta rhythm ($4-12$ Hz) [8, 135] and gamma rhythm ($35-70$ Hz) [41]; the latter is believed to originate in the CA3 region. In particular, depending on the concentration of ACh, distinct rhythmic oscillations may emerge corresponding to different frequency bands [38, 73]. These rhythms, or waves, have been identified and correlated to different behavioural states. For example, theta oscillations recorded from the hippocampus, have been observed during active exploration [133] and rapid-eye-movement (REM) sleep [13, 10], while gamma rhythms are associated with alert behaviours and higher

cognition tasks [104, 19, 23]. Disruption of cholinergic modulation can impair cognitive functions underlying the learning and memory processes [53]. This suggests a bidirectional role for ACh in modulating hippocampal dynamics, where both high and low levels of ACh are essential for different stages of memory formation [63, 58, 73, 114].

Chapter 3

Mathematical Neuroscience Background

3.1 Electrophysiology of neurons

As discussed in Section 2.1.1, the cell membrane of a neuron, like all other mammalian cells, is made up of a bilayer that is impermeable to ions, and separates the intracellular fluid of the cell's interior from the surrounding extracellular fluid [26]. Due to this impermeability, a potential difference exists between these two regions across the neuronal membrane, known as the *membrane potential*, V [36]. This is mathematically defined as

$$V = V_{inside} - V_{outside}, \tag{3.1}$$

where V_{inside} is the intracellular potential and $V_{outside}$ is the potential of the extracellular fluid. Both regions are populated by ionic species such as sodium (Na^+), potassium (K^+), and chloride (Cl^-) [1]. The distribution of these ions is not uniform: K^+ ions have a higher intracellular concentration whereas Na^+ & Cl^- ions have higher extracellular concentration [36]. These concentration differences are maintained through the active transport of ions by specialized structures embedded within the membrane, known as *ionic pumps.*

A variety of ion-conducting channels, are embedded within the membrane, which regulate the movement of ions in and out of the cell, allowing the membrane to be selectively permeable to some ionic species. Some ion channels open or close depending on the membrane potential. These are known as *voltage-gated channels*. *Non-gated channels* on the other hand, are always open [36].

[1] There are other ionic species but these are the principle ions responsible for action potentials.

The electrical activity of the neuron is primarily driven by the electrochemical forces that emerge due to the differences in the relative ionic concentrations inside and outside the cell. Differences in individual ionic concentration induce a chemical gradient, which tends to drive ions to diffuse from a region of high concentration to low concentration [36]. The passive flow of ions, driven by the chemical gradient, causes a separation of charges across the impermeable layer, and induces an electrical gradient across the membrane. The membrane potential at which these two forces balance is defined as the corresponding *equilibrium or Nernst potential* for the ion. Similarly,this potential can be determined by the following relation:

$$E_{ion} = \frac{RT}{zF} \ln \left(\frac{[outside]}{[inside]} \right) \tag{3.2}$$

Eq. (3.2) is known as the *Nernst equation*. In Eq. (3.2), $[outside]$ & $[inside]$ refer to the ion concentrations in the extracellular fluid and intracellular fluid respectively, z is the valence number corresponding to the ion, R is the ideal gas constant, T is the absolute temperature and F is the Faraday's constant. At rest, the neuron is permeable to K^+, Na^+ and Cl^- which results in a *resting potential* somewhere between the equilibrium potentials of K^+, Na^+ and Cl^-.

The cell is said to be *depolarized*, when the membrane potential is greater than the resting potential. The cell is *hyperpolarized*, when the membrane potential is less than the resting potential. An action potential occurs when the membrane undergoes a rapid depolarization to a positive value followed by repolarization to a negative value, resulting in a "spike" in the membrane potential. In the following section, we introduce a model that is capable of describing this dynamical behaviour of the neuronal membrane potential.

3.2 Hodgkin-Huxley model of the action potential

In 1952, Alan L. Hodgkin and Andrew F. Huxley presented a mathematical description for the generation of an action potential in the giant axon of a squid [70]. This formulation culminated in the very first biophysical representation of neuron behaviour, which we know as the *Hodgkin-Huxley model*. This formalism serves as a foundation for many biophysical neuron models that are used today.

In earlier experiments, Hodgkin and Cole attributed the significant rise in the membrane potential during an action potential to changes in the membrane's permeability to different ions [17, 123]. This discovery was followed by a series of experiments conducted by Hodgkin and Huxley [66, 69, 67, 68], through which they established a quantitative link between

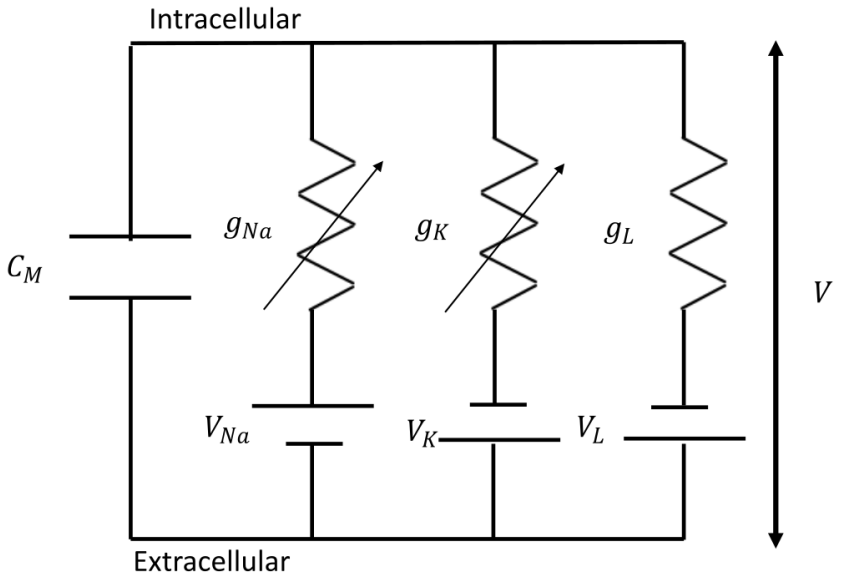


Figure 3.1: Schematic for the equivalent circuit model of the cell as proposed by Hodgkin and Huxley. The sodium and potassium channels are modelled as variable resistor in series with a battery. The ion channels are connected in parallel with one-another and with the capacitor.

changes in membrane permeability to sodium and potassium, resulting in the generation of the action potential.

3.2.1 Circuit model of the neuronal membrane

Based on their observations in [70], Hodgkin and Huxley suggested that the electrical behaviour of the neuronal membrane could be modelled as an equivalent circuit composed of batteries, resistors and capacitors as illustrated in Figure 3.1. In this representation, an ion channel is modelled as a conductor in series with a battery, where the conductor represents the membrane permeability to the ion and the battery models the ion's concentration gradient. The phospholipid bilayer contributes to the separation of charges across the cell membrane, making it functionally comparable to a capacitor [36].

Note that this representation assumes that the potential is the same throughout the cell. Hodgkin and Huxley achieved this in their experiments on the squid axon using a space-clamping technique [36]. Thus, the total membrane current can be divided into a

capacitive current and an ionic current:

$$I_{total} = I_{cap} + I_{ion} \tag{3.3}$$

The capacitive current comes from the fact that the membrane can store charge and release it in the form of currents. As such, the relationship between the total charge stored by the membrane, Q, and the membrane potential, V, can be described by:

$$Q = C_M V, \tag{3.4}$$

where C_M is the membrane capacitance. We can obtain I_{cap}, by taking the time derivative of Eq. (3.4), allowing us to rewrite Eq. (3.3) as the following:

$$I_{total} = C_M \frac{dV}{dt} + I_{ion} \tag{3.5}$$

According to Kirchoff's law, the net current, I_{total}, leaving this circuit is zero, and thus Eq. (3.5) can be rewritten as the following:

$$C_M \frac{dV}{dt} = -I_{ion}, \tag{3.6}$$

where ionic current, I_{ion}, is written as the sum of the sodium, potassium and leak currents [70], leading to the following equation:

$$C_M \frac{dV}{dt} = -I_{Na} - I_K - I_L \tag{3.7}$$

Each current included in Eq.(3.7) is modelled as a product of the conductance for that specific ion, $\hat{g}_{ion}$, and the potential difference across the ion channel

$$C_M \frac{dV}{dt} = -\hat{g}_{Na}(V - V_{Na}) - \hat{g}_K(V - V_K) - \hat{g}_L(V - V_L). \tag{3.8}$$

The $\hat{g}_{ion}$ is a measure of the membrane's permeability to that ion. $(V - V_{ion})$ is the driving force that causes the ionic flux, where V_{ion} is the Nernst potential. The leak current models to the passive flow of ions through the non-gated channels, with relatively constant conductances [36]. In the model, C_M, V_{Na}, V_K, V_L and $\hat{g_L}$ are constant [70].

During an action potential, the membrane permeabilities $\hat{g}_{Na}$ and $\hat{g}_K$ not only change with time but with the membrane potential [69, 68]. Consequently, these changes in the conductances, represent the opening and closing of the corresponding ion channels.

3.2.2 Channel kinetics

As described in Section 3.1, ion channels maybe be regulated by voltage-dependent gates. An ion channel is said to be open when all its gates are in the open state. The opening and closing of a gate can be modelled as follows [36]:

$$C \underset{\beta_X(V)}{\overset{\alpha_X(V)}{\rightleftharpoons}} O, \tag{3.9}$$

where $\alpha_X(V)$ denotes the rate of transition from a closed (C) to an open (O) state, and $\beta_X(V)$ is the rate for the reverse transition. If X represents the fraction of open gates, then according to the law of mass action, we can derive the following relation:

$$\frac{dX}{dt} = \alpha_X(V)(1 - X) - \beta_X(V)X = \frac{X_\infty(V) - X}{\tau_X(V)}, \tag{3.10}$$

where

$$X_\infty(V) = \frac{\alpha_X(V)}{\alpha_X(V) + \beta_X(V)} \qquad \tau_X(V) = \frac{1}{\alpha_X(V) + \beta_X(V)} \tag{3.11}$$

If the voltage is held constant (voltage-clamped[2]), equation (3.10) can be solved with an initial condition $X(0)$.

$$X(t) = X_\infty(V) + (X(0) - X_\infty(V)) \exp^{-\frac{t}{\tau_X(V)}}, \tag{3.12}$$

where $m(t)$ tends to its steady state value, m_∞, at a rate that is determined by the time constant, $\tau_X(V)$. In the Hodgkin-Huxley model, the sodium and potassium channels are modelled as follows [70]:

$$\hat{g}_{Na} = g_{Na} \cdot m^3 h \tag{3.13}$$

$$\hat{g}_K = g_K \cdot n^4, \tag{3.14}$$

where g_{Na} and g_K represent the maximal conductances, m and h are the sodium activation and inactivation gating variables, respectively, and n is the potassium activation variable. Each gating variable X satisfies an equation in the form of Eq. 3.10, with rate functions $\alpha_X(V)$ and $\beta_X(V)$ determined by fitting them to steady-state activation/inactivation curves and time-constants obtained from voltage-clamp experiments.

[2] A voltage clamp experiment enables the experimenter to hold the membrane potential at a constant level V_c [36].

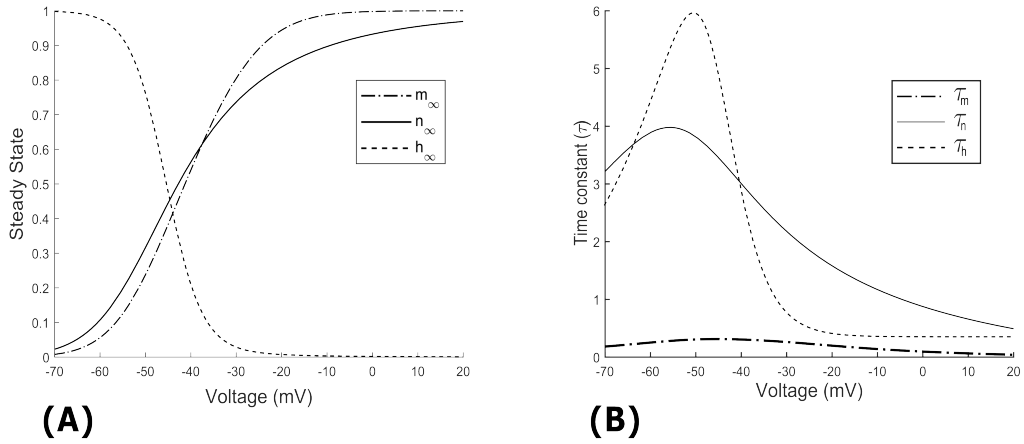


Figure 3.2: Hodgkin Huxley functions. **(A)** The steady state functions, $m_\infty(V), n_\infty(V)$ and $h_\infty(V)$, are plotted. **(B)** The time constants, τ_m, τ_n and τ_h are plotted.

As illustrated in panel (A) of Figure 3.2, the steady state functions of the activation variables, $m_\infty(V)$ and $n_\infty(V)$, tend to 0 for hyperpolarizing currents and 1 for depolarizing currents. This corresponds to the activation of their respective variables m and n, when the membrane is depolarized during an action potential. On the other hand, the steady state function of the inactivation variable, $h_\infty(V)$ is a decreasing function which approaches 1 for hyperpolarizing currents and 0 for depolarizing currents [36]. We also note that the time constants satisfy the following relationship: $\tau_m(V) << \tau_h(V)$ and $\tau_n(V)$, as illustrated in panel (B), Figure 3.2.

In the following section, we describe the relative timings of the ionic currents that facilitate the generation of an action potential.

3.2.3 Hodgkin Huxley description of an action potential

An action potential is an electrical response observed in neurons, characterized by a significant deviation in the membrane potential from rest. Action potentials usually occur in three stages as illustrated in Figure 3.3. The first stage is *depolarization* during which the membrane potential rises from resting to some peak value. This is followed by the second stage, *repolarization*, in which the membrane potential decreases toward the resting potential. Often, there can be an after-hyperpolarization, during which the membrane potential decreases below the resting potential to a minimum value before returning back

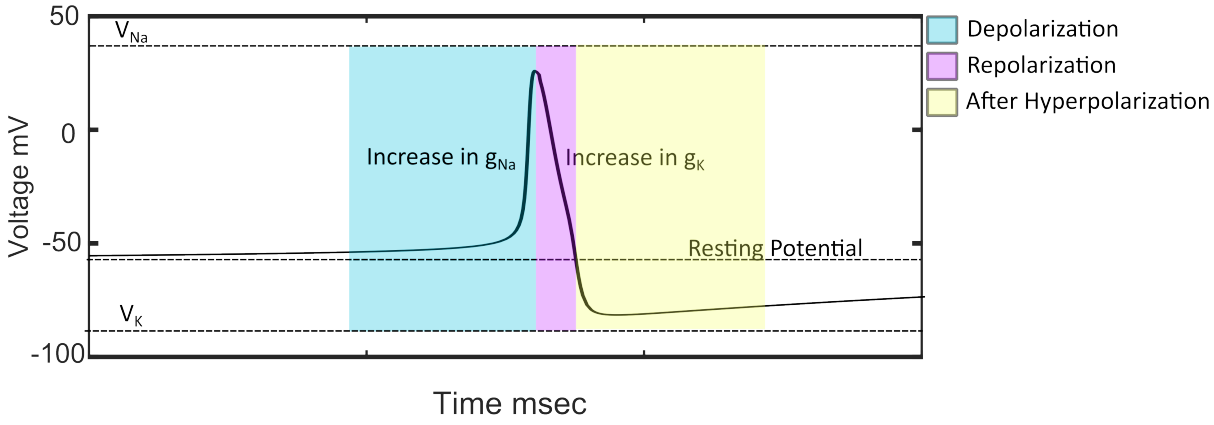


Figure 3.3: Illustration of an action potential and the different phases characterized by changes to the conductances.

to baseline. Using the Hodgkin-Huxley model, we describe the dynamical behaviour of the sodium and potassium currents during the different stages of an action potential.

Consider a neuron where the membrane potential is initially at the *resting potential*. An action potential will be initiated if an external current induces a sufficient depolarization of the membrane. This increase in membrane potential raises the activation variables m and n, while decreasing the inactivation variable h (provided in Eqs. (3.13) and (3.14)). Since $\tau_m(V) << \tau_h(V)$ and $\tau_n(V)$ for all V, a relatively faster activation of $\hat{g}_{Na}$ occurs. The fast activation of $\hat{g}_{Na}$ triggers an inward Na^+ current (I_{Na}) , driving the membrane potential (V) closer to the Nernst potential of sodium (V_{Na}) [74]. This, in turn, further increases $\hat{g}_{Na}$, creating a positive feedback loop. This process marks the *depolarization* phase of the action potential, characterized by an upstroke in V as illustrated in the Figure 3.3. Meanwhile, the K^+ channels begin slowly activating in the background, as determined by a delayed activation of n (since $\tau_m < \tau_n$). During this phase, I_{Na} dominates the total current.

As the membrane potential gets closer to V_{Na}, the driving force of the sodium current ($V - V_{Na}$) decreases and the sodium channel begins to inactivate. The inactivation gate will close, since h decreases towards 0, effectively shutting down the Na^+ current. At the same time, n increases [36] thereby increasing the potassium driving force ($V - V_K$). This allows an outward potassium current to dominate, driving the membrane potential towards the resting potential, marking the repolarization phase of the action potential, corresponding to the downstroke in V as shown in the Figure 3.3. Following repolarization,

the membrane potential V_M will often decrease below the resting potential due to the slow activation of the potassium current. This period of extra hyperpolarization is known as the after-hyperpolarization phase marked by the trough following the downstroke of the action potential in Figure 3.3, after the membrane potential crosses the resting potential. It is subsequently followed by a refractory period, during which K^+ channels begin to deactivate and the Na^+ channels deinactivate allowing for the membrane potential to slowly return to the resting value.

Note that the membrane potential must exceed a certain threshold, for the neuron to generate an action potential—a phenomenon known as the 'all or none' principle. In this case, if the input is not sufficiently large, then no action potential occurs.

3.2.4 Generalization of the Hodgkin-Huxley model

The Hodgkin-Huxley model describes an action potential in a squid giant axon, that is primarily driven by a fast (transient) sodium current and the delayed rectifier potassium current. However, neurons in general can have many different ion channels in addition to those describes in the Hodgkin-Huxley model. In our work, we are particularly interested in a voltage-dependent potassium current known as the M-current. We review two relevant properties of the Hodgkin-Huxley model as describes in Section 3.2, that can be utilized to build a biophysical model of a neuron which incorporates the muscarinic current (M-current).

Conductance-based modelling

Models that adapt the framework of Hodgkin and Huxley to describe the dynamics of the membrane potential due to the presence of various ion channels are referred to as *conductance-based models* [22]. In particular, these models use the formalism outlined in Section 3.2.2 to describe the ion channels kinetics. In our work, we utilize a conductance-based model to reproduce the firing properties of a neuron in the hippocampus under the effect of M-current.

Single-compartment and multi-compartment models

The membrane potential in Eq. (3.8) is represented as a single variable and is spatially independent. Physically, this corresponds to the representation of a neuron as a *single, isopotential, compartment*. Alternatively, neuronal morphology may be incorporated into

the model by dividing the neuron into multiple compartments, each equipped with its own membrane potential and a set of gating variables. Individual compartments are coupled to neighbouring compartments via coupling currents, modelled using Ohm's law. Details regarding multi-compartmental modelling can be found in [36].

In our work, we consider single-compartment neuron models, where the voltage variable represents the membrane potential ar a particular location of the neuron, typically the soma [11]. Single compartment models can be derived from detailed multi-compartment models using a series of parameter adjustments as depicted in Figure 3.4. In Chapter 6, we consider a pyramidal neuron that is modelled using a single-compartmental reduction of a highly detailed 19-compartment model.

To summarize, the pyramidal neuron model is described by the following equation:

$$C_M \frac{dV}{dt} = I_{app} - \sum_{i=1}^{N} g_{i,ion} \cdot a_i^{p_i} \cdot b_i^{q_i}, \cdot (V - V_{ion}) \tag{3.15}$$

where I_{app} denotes the externally applied current, and the ionic currents are summed, with each described by its maximal conductance $g_{i,ion}$, the driving force $(V - V_{ion})$ and gating variables a_i and b_i, as described in Section 3.2.2.

3.3 Excitability of a neuron

Towards the end of Section 3.2.3, we briefly discuss an 'all or none' principle in which the membrane potential must be sufficiently depolarized, i.e. cross some minimum threshold, in order to evoke an action potential. Typically, to evoke this transient response, the membrane potential is depolarized by a brief pulse of current. In Eq. (3.15), this corresponds to the external current, I_{app}, modelled as a square pulse. The neuron may exhibit a graded response to brief current pulses of different amplitudes that do not meet the threshold. In this case, the membrane potential increases by a little each time before returning back to rest. For a large enough amplitude, the neuron evokes an all-or-none action potential response. Experimentally, it is quite difficult to pinpoint the exact threshold beyond which, the neuron generates an action potential. Alternatively, the external current, I_{app}, may be applied for a long period of time. In this case, for a strong enough *constant* input, the neuron may respond, by firing repetitive action potentials. The transition of the neuron from its resting state to the repetitive spiking state, can be described by its *excitability.* In [74], a neuron is said to be excitable, when it is near a bifurcation point.

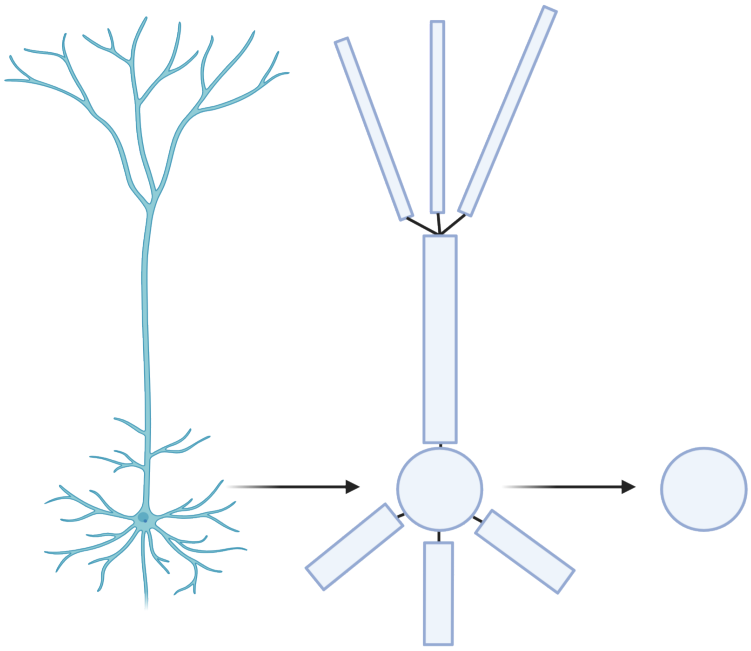


Figure 3.4: Depiction of a sequence of finite-compartmental representations of a pyramidal neuron with the last stage representing the neuron as a single compartment. Created in https://BioRender.com

From a geometric point of view, the neuron at resting potential, corresponds to a stable equilibrium point in the phase portrait associated with the system. By applying a strong enough *constant* current input, the corresponding system undergoes a bifurcation resulting in the appearance of a stable limit cycle in the phase portrait. Bifurcation theory is used to analyze how solutions change as parameters in a model are varied [129]. Using bifurcation theory, we can classify how the behaviour of a neuron model changes as the externally applied current (I_{app}) is varied. This type of bifurcation is referred to as co-dimension 1, since we only one parameter is varied to change the qualitative dynamics [129].

Prior to the introduction of bifurcation theory, Hodgkin classified the different behaviours of a neuron by stimulating the squid axon with input currents of various amplitudes [66]. Through this process, he identified three classes of responses by plotting the frequency of the spiking vs the corresponding amplitude of the input current, otherwise known as a frequency-current (F/I) curve. It wasn't until 1989, that Rinzel and Ermentrout reproduced the same classification through the lens of dynamical systems theory [115]. We briefly describe the first two classes which are relevant in this thesis, and

their corresponding co-dimension 1 bifurcations with respect to the strength of the applied current.

Class I response

According to Hodgkin, neurons, exhibiting class I responses, can generate action potentials starting at arbitrarily low frequencies [74]. In their (F/I) curve, we see that the neuron can exhibit oscillations starting from zero to relatively high frequencies for larger strength of the input current. Rinzel and Ermentrout showed that in conductance-based models this type of transition corresponds to a *saddle-node on an invariant circle bifurcation (SNIC)*[115, 36]. In this type of bifurcation, a stable node (neuron at resting potential) will coalesce with a saddle point as the current input is increased, and like clasping the ends of necklace, it forms a closed orbit. Increasing the current further, annihilates the fixed point on the orbit and in its place is a stable limit cycle, which corresponds to repetitive spiking. At the point of coalescence (bifurcation point), the closed orbit, also known as an invariant circle, corresponds to a trajectory with infinite period. This can be interpreted as an action potential that asymptotically approaches the resting potential post-spike, without ever firing again. Neurons exhibiting class I responses are also known as type I neurons.

The Hodgkin-Huxley model presented in Section 3.2 is a neuron with type I dynamics.

Class II response

For neurons exhibiting a class II response, the periodic spiking is initiated at some positive minimum frequency, and they are relatively insusceptible to the strength of the applied current. This is also evident in their (F/I) curve, where the transition from resting to spiking is discontinuous and the range of frequencies is relatively narrow compared to type I neurons. In conductance-based models, this type of transition is usually characterized by a *sub-critical Andronov Hopf bifurcation*, in which a stable fixed point *loses* its stability via an unstable limit cycle. Typically this bifurcation occurs together with a saddle-node of limit cycles, which gives rise to the stable limit cycle associated with periodic spiking. This explains why the frequency does not approach zero as the applied current is near the bifurcation point. Further, there exists a neighbourhood of the bifurcation point (non empty set of current values), in which the limit cycle and the fixed point are both stable; i.e., the system exhibits bistability. Neurons exhibiting a class II response, are also referred to as type II neurons.

From a dynamical systems perspective, a neuron at rest corresponds to a stable fixed point and the question of whether the stability is lost or if the fixed point completely vanishes through the bifurcation is what typically defines its excitability type. In the next section we introduce a slow potassium current found abundantly in many hippocampal neurons, whose presence can switch the behaviour from Class-II to Class-I dynamics.

3.3.1 Muscarinic current (M-current)

In addition to the delayed rectifier potassium channel, there are other voltage-gated potassium channels, that affect the firing properties of a neuron. For example, the A-current is a transient potassium current with similar dynamics as the transient sodium current, in that they both contain activation and inactivation gates [36].

In the present thesis, we study a slow non-inactivating voltage-dependent potassium current known as the muscarinic or M-current. The M-current is carried by the corresponding voltage-gated M-type channels (for muscarine sensitive) that activate at low-thresholds [77]. It is down-regulated in the presence of acetylcholine through the stimulation of metabotropic muscarinic cholinergic receptors (mAChRs) associated with the channel [77, 72]. These receptors initiate secondary signalling pathways that lead to the closure of the corresponding M-channels [55, 12]. The M-current can affect the excitability of a neuron and is responsible for a phenomenon known as spike frequency adaptation, in which the firing rate of a neuron that has been sufficiently depolarized for repetitive spiking is gradually decreased [36]. These currents are also found in excitatory pyramidal neurons of the cortex and hippocampus and in inhibitory interneurons within the hippocampus. We can model with M-current conductance with a formalism similar to that of the delayed rectifier potassium current, but, with a slower activation variable, labelled w.

In [4], a general conductance based model for a neuron incorporated with an M-current is given by:

$$C_M \frac{dV}{dt} = I_{app} - \sum_{i=1}^{N} g_{i,ion} \cdot a_i^{p_i} \cdot b_i^{q_i} \cdot (V - V_{ion}) + g_M w (V - V_K), \tag{3.16}$$

where g_M is the maximal M-current conductance, w is the activation variable and V_K is the corresponding Nernst potential for potassium. The remaining parameters are the same as those described in Eq. 3.15.

Experimentally, acetylcholine has been demonstrated to suppress the voltage dependent M-current [55], a calcium activated potassium current [93] and the leak current [126]. In

our work, we focus on in its effect on the M-current. This is of particular interest to us, since the cholinergic suppression of M-current has been shown to switch the excitability of pyramidal neurons from type II to a type I dynamics [126, 127]. Similarly, for a general conductance-based model incorporated with an M-current, it has been shown that the change in the neuronal excitability with respect to the M-current conductance corresponds to an underlying co-dimension 2 Takens Bogdanov bifurcation in the $\{I_{app}, g_M\}$ parameter space [4]. We replicate this result for a specific model of the pyramidal neuron in Chapter 6, using bifurcation analysis.

3.4 Modelling synaptic transmission

In order to study the network level behaviour of neurons, we need to model the synaptic transmission that can arise between two or more neurons with chemical synapses. In Section 2.1.2, we described a series of biochemical events that lead to the release of a neurotransmitter into the synaptic cleft to enable synaptic transmission via a chemical synapse. Based on this, we review a model describing the presynaptic release of transmitter molecules and its effect on the post synaptic conductance. The released transmitter molecules bind to a closed receptor on the post synaptic neuron which can modify its membrane potential [22]. We can introduce a synaptic current (I_{syn}) in the principle membrane potential equation of the post-synaptic neuron to model this effect:

$$C_M \frac{dV}{dt} = I_{app} - I_{ionic} - I_{syn}, \tag{3.17}$$

where the I_{syn} synaptically couples the presynaptic and postsynaptic neuron. It is modelled with the same formalism as an ionic current; as a product of conductance g_{syn} and a driving force $(V - V_{syn})$[36]:

$$I_{syn} = g_{syn}(t) \cdot (V - V_{syn}) \tag{3.18}$$

Here, V_{syn} determines whether I_{syn} will tend to increase or decrease the membrane potential, V, of the post synaptic neuron. The value of V_{syn} is determined by type(s) of ions that pass through the channel in the post-synaptic membrane associated with a particular neurotransmitter and receptor. Accordingly, the effect can classify the neurotransmitter as excitatory ($V_{syn} \sim 0$) or inhibitory ($V_{syn} < V_{rest}$). Unlike in the case of the ionic current, g_{syn} depends on the membrane potential of the presynaptic neuron.

3.4.1 Destexhe model

In our study we will use a synaptic model due to Destexhe and collaborators. In this model, the synaptic conductance is given by

$$g_{syn}(t) = \overline{g}_{syn} \cdot s(t), \tag{3.19}$$

where $\overline{g}_{syn}$ is the maximal conductance value and s is a synaptic gating variable, representing the fraction of receptor channels on the postsynaptic neuron at time t, ready to bind with the transmitter molecules. The interaction of transmitter molecules with the postsynaptic receptors can be modelled as a two-state kinetic scheme similar to the opening and closing of voltage-gated ion-channels, except in this case, the channel kinetics depend on the amount of neurotransmitter released:

$$C + T \underset{\beta}{\overset{\alpha}{\rightleftharpoons}} O \tag{3.20}$$

In Eq. (3.20), C represents a closed receptor which binds with a transmitter molecule, T, and changes to the open state, represented by O. α and β are the corresponding forward and backward rate constants describing the binding process. In the reverse reaction, transmitter molecules unbind from the receptor and it closes.

Using mass-action kinetics similar to the Hodgkin-Huxley model presented in Section 3.2.2, $s(t)$ satisfies:

$$\frac{ds}{dt} = \alpha[T](1 - s) - \beta s, \tag{3.21}$$

where α is the rate at which receptor channels are bound. β is the closing rate for the channels.

In 1994, Destexhe modelled the relationship between transmitter concentration, $[T]$, and the presynaptic membrane potential V_{pre} [24] as follows

$$[T](V_{pre}) = \frac{T_{max}}{1 + \exp\left(\frac{-(V_{pre} - V_T)}{K_p}\right)}, \tag{3.22}$$

where V_T is the voltage at which the function is half-activated, K_p is the steepness of the voltage dependence and T_{max} is the maximal concentration of the neurotransmitter in the synaptic cleft.

Based on fitting experimental data, Destexhe [24] proposed the following parameter values $V_T = 2$, $K_p = 5$ mV and $T_{max} = 1$ mM. We use this formalism to model an AMPA synapse in Chapter 6.

Chapter 4

Phase Model Reduction of Conductance-based Models

As discussed in Section 3.3, neurons can display periodic firing [26, 77, 14] which can be observed experimentally and modelled computationally using high dimensional, detailed biophysical models. To investigate the associated neural synchrony, we can consider these detailed biophysical models, though they may have the disadvantage of heavy computational demands and the inclusion of details irrelevant in the study of synchronization. In this chapter, we introduce an approach that involves the reduction of a highly dimensional biophysical model to a simpler model which preserves the relevant dynamical features needed to study synchrony. The idea is to gain insight into the synchronization properties of the neuron by analyzing the effect of perturbations to its phase. This can be done in two ways: by determining a phase-response curve for a neuron or deriving a phase oscillator approximation of the model.

The latter approach, which has been used to study synchronization properties of networks of weakly coupled oscillators [29, 35, 51, 84, 44], is the method we adopt in this thesis. The main focus of this chapter is to present the phase model approximation for a biophysical neural network.

4.1 Theoretical background

A biophysical conductance-based model of a neuron, built using methods introduced in the Chapter 3, can be represented as the following generic differential equation model of a

single oscillator:

$$\dot{X}(t) = F(X(t)) \qquad X \in \mathbb{R}^M. \tag{4.1}$$

For example for a model such as Eq. (3.16), we have $X = \left[V, m, h, n, w\right]^T$ and F is a vector function describing the rate of change for each variable. In Section 3.3, we described how the transition of a neuron model from rest to repetitive firing can be analyzed from the perspective of dynamical systems. Note that repetitive firing in the model corresponds to an isolated, asymptotically stable periodic solution of the differential equation, i.e., a *stable limit cycle*. In the generic model (4.1), a limit cycle is an isolated periodic solution, $X^*(t)$, with an initial condition, $X(0) = X_0$, that can described by a closed trajectory, Γ, in $\mathbb{R}^M$ [71]. Recall that if the period of $X^*(t)$ is T , then $X^*(t+T) = X^*(t)$ for all time $t > 0$. In particular, this means for each $y \in \Gamma$, there is a unique $t \in [0, T)$ such that $y = X^*(t)$. The limit cycle is called stable, if for all $\varepsilon > 0$, there exists an open neighbourhood V_ε of Γ such that for all $x \in V_\varepsilon$, if $X(t)$ is a solution trajectory of Eq. (4.1) with initial condition, $X(0) = x$, then $d\left(X(t), \Gamma\right) < \varepsilon$. The limit cycle is *asymptotically stable* [111], if it is stable and, in addition, for all solution trajectories, $X(t)$, initialized within an open neighbourhood, V, of Γ, we have

$$\lim_{t\to\infty} d\left(X(t), \Gamma\right) = 0$$

The limit cycle is said to be *exponentially asymptotically stable*, if the distance, $d\left(X(t), \Gamma\right)$, decays exponentially as $t \to \infty$.

A closed trajectory $\Gamma \subset \mathbb{R}^M$ is topologically equivalent to the unit circle $\mathbb{S}^1$ [71, 102], meaning we can define a continuous mapping (h) that can deform the former into the latter. Essentially, for each $y \in \Gamma$, the mapping h assigns an angle $\theta \in [0, 2\pi)$ such that

$$\dot{\theta} = \Omega = \frac{2\pi}{T} \qquad \theta \in \mathbb{S}^1, \tag{4.2}$$

where T is the period of the limit cycle and Ω is the corresponding natural frequency. Following Winfree [136], we can define a mapping h as follows.

$$\begin{aligned} & h : \Gamma \mapsto [0, 2\pi] \\ s.t. \quad & \theta(t) = h(X^*(t)) \text{ is a solution to Eq. (4.2)}, \end{aligned} \tag{4.3}$$

which allows us to locally represent the $M-$dimensional dynamics for a system (4.1) , exhibiting a stable limit cycle, by a single variable, the phase (θ) which satisfies (4.2) (Theorem 4.2 in [71]). Conventionally, $\theta = 0$ is assigned to the peak of Γ with respect to

some norm. For the neural model we consider, this corresponds to the time $t_{spike} \in [0, T)$, when the neuron spikes (V is maximum). Accordingly, the phase at time t represents the amount of time that has passed since the oscillator last spiked as a fraction of 2π. This can be defined as follows.

$$\theta(t) = 2\pi \frac{(t - t_{spike}) \mod T}{T} \tag{4.4}$$

If we assume that t_{spike} is 0, then the phase satisfies $\theta(0) = 0$ and the mapping (4.4) defines a *natural phase* for the limit cycle Γ.

Now let us consider a network of N uncoupled oscillators such that for each i, the corresponding oscillator X_i has a stable limit cycle attractor $\Gamma_i \subset \mathbb{R}^{MN}$.

$$\dot{X}_i(t) = F_i(X_i(t)) \qquad X_i \in \mathbb{R}^M \qquad i = \{1, 2, \ldots, N\} \tag{4.5}$$

Each limit cycle Γ_i is independent and topologically equivalent to $\mathbb{S}^1$. As a result the direct product of limit cycles ($\vec{\Gamma} = \Gamma_1 \times \Gamma_2 \times \cdots \times \Gamma_N$) is homeomorphic to the $n-Torus$ ($\mathbb{T}^N = \mathbb{S}^1 \times \mathbb{S}^1 \times \ldots \mathbb{S}^1$) [71]. If we assume that for all $i \in \{1, .., N\}$, $F_i = F$, then $\Gamma_i = \Gamma \subset \mathbb{R}^M$ and Eq. (4.5) reduces to the following

$$\dot{X}_i(t) = F(X_i(t)) \qquad X_i \in \mathbb{R}^M \qquad i = \{1, 2, \ldots, N\} \tag{4.6}$$

As for the single oscillator, we can represent the $M-$dimensional dynamics for each oscillator, i.e., each stable limit cycle solution $X_i^*(t)$, in (4.6) by a corresponding phase variable θ_i. This gives the following

$$\dot{\theta}_i = \Omega \qquad \theta_i \in \mathbb{S}^1 \qquad i = \{1, 2 \ldots, N\} \tag{4.7}$$

where $\Omega = \frac{2\pi}{T}$ and T is the period of the limit cycle Γ as illustrated in Figure 4.1. Eq. (4.7) is the corresponding *phase model* for (4.6). Integrating (4.7) for each i, we get

$$\theta_i(t) = \Omega t + \varphi_i \qquad \varphi_i \in \mathbb{S}^1, t \in [0, T_i) \tag{4.8}$$

In Eq (4.8), φ_i is also known as the *phase deviation* for θ_i (corresponding to X_i), which describes the deviation of $\theta_i(t)$ from the natural phase [71]. For an uncoupled system such as (4.6), the phase deviation is constant and is determined by the initial conditions.

4.2 Phase model for a weakly connected network

In the present thesis, we study a network of weakly coupled biophysical neural oscillators represented as follows

$$\dot{X}_i(t) = F(X_i(t)) + \varepsilon G_i(X_1, X_2, \ldots, X_N, \varepsilon) \qquad X_i \in \mathbb{R}^M, i \in \{1, .., N\}, \tag{4.9}$$

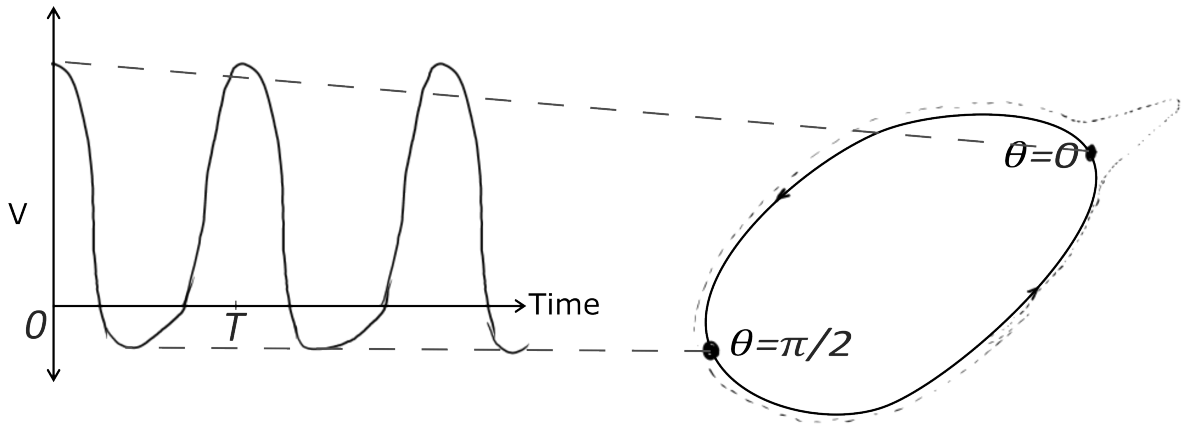


Figure 4.1: Phase description for a limit cycle. *Left* Voltage trace showing the phase zero as the peak of the potential. *Right* Limit cycle Γ in the phase portrait with different points $(\theta = 0, \pi/2)$ corresponding to the spike times and half period $T/2$ of the time trace.

where the strength of coupling, described by G_i, is determined by the parameter ε[1]. Typically by weak we mean that $\varepsilon << 1$. We assume that each oscillator in (4.9) has an asymptotically stable limit cycle attractor $\Gamma \subset \mathbb{R}^M$ corresponding to a T periodic solution $X_i^*(t)$, when decoupled ($\varepsilon = 0$). The goal is to now derive a corresponding phase model for Eq. (4.9) in the limit of weak coupling $\varepsilon << 1$.

We know that the phase model in the uncoupled case ($\varepsilon = 0$) is given by Eq. (4.7), which represents the local $M-$ dimensional dynamics corresponding to Eq. (4.6) restricted to the invariant manifold M_Γ, described by the direct product of limit cycles Γ, $M_\Gamma = \Gamma \times \Gamma \times \cdots \times \Gamma$ (Lemma 4.5 in [71]) . For $\varepsilon > 0$ and sufficiently small, it can shown that the M_Γ is perturbed to another invariant manifold, M_Γ^ε, associated with Eq. (4.9) (Chapter 4 in [71]) and that the corresponding phase model is given by:

$$\dot{\theta}_i(t) = \Omega + \epsilon g_i(\theta_1, \ldots, \theta_N) \qquad t \in [0, T), \tag{4.10}$$

where g_i is known as the *phase coupling function* and explicitly depends on the phase variables θ_i (Chapter 9 in [71]). Essentially, we assume that the coupling introduced between the oscillators in Eq. (4.9), is weak enough, such that it does not affect the amplitude or shape of the limit cycles Γ, but only the relationship between the phase variables, θ_i. As a result, we can expect the phase model to have the following form

$$\theta_i(t) = \Omega t + \varphi_i(t) \qquad \varphi_i \in \mathbb{S}^1, t \in [0, T), \tag{4.11}$$

[1]By convention, this is taken to be positive.

where the phase deviation, φ_i in (4.7), will describe the deviations of the subsystem X_i, from its natural phase *due to influences from other oscillators*. Comparing Eqs. (4.10) and (4.7), it becomes clear to us that the phase deviations, φ_i, must be slowly varying with time, t.

Below we present a theorem, together with a sketch of its proof, that enables us to approximate the phase coupling functions, g_i, for a pair of weakly coupled oscillators. The theorem is based on Malkins theorem [94, 95], with the proof strategy that closely follows the approach from Theorem 9.2 in [71].

Theorem 4.2.1. *Consider a pair of identical neurons that are coupled together through a reciprocal synaptic connection ($N = 2$ and $G_i(X_1, X_2) = G(X_i, X_{i+1 \pmod 2})$ in Eq. (4.9))* [2].

$$\begin{aligned} \dot{X}_1 &= F(X_1) + \varepsilon G(X_1, X_2) \\ \dot{X}_2 &= F(X_2) + \varepsilon G(X_2, X_1), \end{aligned} \tag{4.12}$$

Suppose that in the corresponding decoupled system ($\varepsilon = 0$),

$$\begin{aligned} \dot{X}_1 &= F(X_1) \\ \dot{X}_2 &= F(X_2) \end{aligned} \tag{4.13}$$

each oscillator exhibits an exponentially asymptotically stable $T-$periodic solution associated with a limit cycle attractor Γ. Let φ_i be the corresponding phase deviation of the i^{th} oscillator as defined in (4.11), and $s = \Omega t$ be a scaled parameter of time. Then φ_i satisfies the following differential equation.

$$\begin{aligned} \frac{d\varphi_1}{ds} &= \varepsilon H(\varphi_2 - \varphi_1) + \mathcal{O}(\varepsilon^2) \\ \frac{d\varphi_2}{ds} &= \varepsilon H(\varphi_1 - \varphi_2) + \mathcal{O}(\varepsilon^2) \end{aligned} \tag{4.14}$$

where the function H, known as the interaction function, is defined in as follows:

$$H(\varphi) = \frac{1}{2\pi} \int_0^{2\pi} \hat{Z}(s) \cdot (G(\Gamma(s), \Gamma(s+\varphi)))\, ds \tag{4.15}$$

In (4.15), $\hat{Z}$ is the unique periodic solution to the linear system

$$\dot{Z} = -\frac{1}{\Omega} \{DF(\Gamma(s))\}^T Z \tag{4.16}$$

[2] We assume that there is no self coupling

satisfying the normalization condition

$$\hat{Z}(0)^T F(\Gamma(0)) = 1 \tag{4.17}$$

Proof. First, we transform the system (4.12) to

$$\Omega \dot{X}_i(s) = F(X_i) + \varepsilon G_i(X_i, X_j, \varepsilon) \qquad i = \{1, 2\}, j = (i+1) \bmod 2, \tag{4.18}$$

through a change of variables $s = \Omega t$. Then the the limit cycle solution Γ of the uncoupled ($\varepsilon = 0$) subsystem is $2\pi-$ periodic with respect to s. Let $X_i^*(s) = \Gamma(s + \varphi_i)$ for $s \in [0, 2\pi]$ be the corresponding periodic solution.

We consider a solution $x_i(s)$ to the subsystem X_i in (4.18), defined on the $\varepsilon-$perturbation of the manifold $M_\Gamma = \Gamma \times \Gamma \subset \mathbb{R}^{2M}$:

$$x_i(s) = \Gamma(s + \varphi_i(\tau)) + \varepsilon P_i(s + \varphi_i(\tau), \varepsilon), \tag{4.19}$$

where $\tau = \varepsilon s$. In (4.19), $\varphi(\tau)$ accounts for the deviations from the natural phase due to the influence from the other oscillator. As outlined above, we expect that it will depend on the slow variable τ, due to the fact that the coupling is on the order of ε. The εP_i are smooth functions that account for the $\varepsilon-$perturbation of the manifold M_Γ.

We differentiate (4.19) with respect to s and expand in ε:

$$\begin{aligned} \dot{x_i} &= \dot{\Gamma}(s + \varphi_i(\tau)) \left(1 + \varepsilon \frac{d}{d\tau} \varphi_i\right) + \varepsilon \dot{P}_i \left(s + \varphi_i(\tau), \varepsilon\right) \left(1 + \varepsilon \frac{d}{d\tau} \varphi_i\right) \\ &= \dot{\Gamma}(s + \varphi_i(\tau)) \left(1 + \varepsilon \frac{d}{d\tau} \varphi_i\right) + \varepsilon \dot{P}_i \left(s + \varphi_i(\tau), 0\right) + \mathcal{O}(\varepsilon^2) \end{aligned} \tag{4.20}$$

Next we substitute (4.19) into (4.18)

$$\begin{aligned} \dot{x_i} = \frac{1}{\Omega} & F(\Gamma(s + \varphi_i(\tau)) + \varepsilon P_i(s + \varphi_i(\tau), \varepsilon)) \\ & + \varepsilon \frac{1}{\Omega} G(\Gamma(s + \varphi_i(\tau)) + \varepsilon P_i(s + \varphi_i(\tau), \varepsilon), \Gamma(s + \varphi_j(\tau)) + \varepsilon P_j(s + \varphi_j(\tau), \varepsilon)) \end{aligned} \tag{4.21}$$

F, G and P_i are smooth functions, so we can expand them as power series in ε to obtain

$$\dot{x_i} = \frac{1}{\Omega} \left(F(\Gamma(s + \varphi_i)) + \varepsilon DF(\Gamma(s + \varphi_i(\tau))) P_i(s + \varphi_i, 0) + \varepsilon G(\Gamma(s + \varphi_i(\tau)), \Gamma(s + \varphi_j(\tau)))\right) \tag{4.22}$$

$+\mathcal{O}(\varepsilon^2)$

Now we equate the left hand side of (4.21) and (4.20). Since Γ is a periodic solution of the uncoupled system, we have

$$\dot{\Gamma}(s+\varphi_i(\tau)) = \frac{1}{\Omega}F(\Gamma(s+\varphi_i(\tau))) \tag{4.23}$$

So the terms of order 1 with respect to ε cancel out.

Using (4.23) in the rest of the equation gives:

$$\begin{aligned}\frac{1}{\Omega}F(\Gamma(s+\varphi_i(\tau)))\frac{d}{d\tau}\varphi_i + \dot{P}_i(s+\varphi_i,0) =& \frac{1}{\Omega}\left(DF(\Gamma(s+\varphi_i(\tau)))P_i(s+\varphi_i,0)\right) \\ &+ \frac{1}{\Omega}\left(G(\Gamma(s+\varphi_i(\tau)),\Gamma(s+\varphi_j(\tau))\right) + \mathcal{O}(\varepsilon)\end{aligned} \tag{4.24}$$

Since φ varies slowly with respect to s, it may be treated as a parameter. We can therefore, perform the following change of variables: $s+\varphi_i \longrightarrow s$, under which (4.24) simplifies as follows:

$$\frac{1}{\Omega}F(\Gamma(s))\frac{d}{d\tau}\varphi_i + \dot{P}_i(s,0) = \frac{1}{\Omega}\left(DF(\Gamma_i(s)P_i(s,0) + G(\Gamma(s),\Gamma_j(s+\varphi_j(\tau)-\varphi_i(\tau))\right) + \mathcal{O}(\varepsilon) \tag{4.25}$$

We wish to study the solutions, P_i of Eq. (4.25), with φ treated as a parameter since it varies slowly with respect to s. To this end we define a linear operator $\mathcal{L}$

$$\mathcal{L}Z = \dot{Z} - A(s)Z = b_i(s,\varphi), \tag{4.26}$$

where

$$A(s) = \frac{1}{\Omega}DF(\Gamma(s)) \tag{4.27}$$

$$b_i(s,\varphi) = \frac{1}{\Omega}G(\Gamma(s),\Gamma(s+\varphi_j(\tau)-\varphi_i(\tau)) - \frac{1}{\Omega}F(\Gamma(s))\frac{d}{d\tau}\varphi_i + \mathcal{O}(\varepsilon) \tag{4.28}$$

Note $A(s)$ and $b_i(s,\varphi)$ are 2π-periodic. Eq. (4.26) is an inhomogeneous linear system which can be studied by considering the adjoint linear homogeneous system

$$\frac{d}{ds}Z(s) = -A(s)^T Z(s) \tag{4.29}$$

with a normalization condition, which we take in the form

$$\frac{1}{2\pi}\int_0^{2\pi} Z(s)\cdot F(\Gamma(s))ds = 1. \tag{4.30}$$

Due to the exponential asymptotic stability of limit cycle Γ, the original system (4.26) and its adjoint (4.29) both have 1 as a simple Floquet multiplier (eigenvalue to the Poincare Map) with all other multipliers not on the unit circle (outside for (4.29) and inside for (4.26)). This means that there exists a unique nontrivial periodic solution $\hat{Z}(t)$ to (4.29), subject to (4.30) and all other periodic solutions are scalar multiples of this solution.

Applying the Fredholm alternative (see (B.0.1)), there is a continuous $2\pi-$periodic solution to (4.26), and hence (4.25) if and only if the orthogonality condition

$$\langle \hat{Z}, b\rangle = \frac{1}{2\pi}\int_0^{2\pi} \hat{Z}(p)\cdot b_i(p,\varphi)dp = 0 \tag{4.31}$$

holds. Applying this condition we find

$$\frac{1}{2\pi\Omega}\int_0^{2\pi} \hat{Z}(s)\cdot\left(G(\Gamma(s),\Gamma(s+\varphi_j(\tau)-\varphi_i(\tau)) - F(\Gamma(s))\frac{d}{d\tau}\varphi_i\right)ds + \mathcal{O}(\varepsilon) = 0 \tag{4.32}$$

where $\hat{Z}$ is a periodic solution to the adjoint problem (4.29) satisfying (4.30). Rearranging (4.32) and using the assumption that $\frac{d\varphi_i}{d\tau}$ is slowly varying with respect to s, we get

$$\frac{1}{2\pi}\int_0^{2\pi} \hat{Z}(s)\cdot(G(\Gamma(s),\Gamma(s+\varphi_j(\tau)-\varphi_i(\tau)) + \mathcal{O}(\varepsilon) = \frac{d}{d\tau}\varphi_i\left(\frac{1}{2\pi}\int_0^{2\pi}\hat{Z}(s)\cdot F(\Gamma(s))ds\right) \tag{4.33}$$

The integral on the right hand side of (4.33) is a function of $\hat{Z}(t)$, and we apply the normalization condition (4.30),

$$\frac{d}{d\tau}\varphi_i = \frac{1}{2\pi}\int_0^{2\pi}\hat{Z}(s)\cdot(G(\Gamma(s),\Gamma(s+\varphi_j(\tau)-\varphi_i(\tau)))\,ds + \mathcal{O}(\varepsilon) \tag{4.34}$$

Recalling that $\tau = \varepsilon s$, we obtain the phase model for a pair of weakly coupled neurons

$$\frac{d}{ds}\varphi_i = \varepsilon\frac{1}{2\pi}\int_0^{2\pi}\hat{Z}(s)\cdot(G(\Gamma(s),\Gamma(s+\varphi_j(\tau)-\varphi_i(\tau)))\,ds + \mathcal{O}(\varepsilon^2) \tag{4.35}$$

We define a function H on $[0, 2\pi]$

$$H(\psi) = \frac{1}{2\pi} \int_0^{2\pi} \hat{Z}(s) \cdot (G(\Gamma(s), \Gamma(s+\psi))\, ds$$

For the pair of weakly coupled neurons, we have the following system describing the evolution of the phase deviations for the system (4.12)

$$\begin{aligned} \frac{d\varphi_1}{ds} &= \varepsilon H(\varphi_2 - \varphi_1) + \mathcal{O}(\varepsilon^2) \\ \frac{d\varphi_2}{ds} &= \varepsilon H(\varphi_1 - \varphi_2) + \mathcal{O}(\varepsilon^2) \end{aligned} \tag{4.36}$$

Finally using that fact $\frac{1}{\Omega} F(\Gamma(s))$ is a solution to linear homogeneous system $\dot{x} = A(s) \cdot x(s)$, we have that $\hat{Z}(s)^T F(\Gamma(s)) = const$ for any $s \in [0, 2\pi]$. Applying the normalization condition, (4.30), we conclude that

$$\hat{Z}(s)^T F(\Gamma(s)) = 1 \qquad \text{for any s}$$

resulting in (4.17), if we take $s = 0$. □

4.2.1 Physical interpretation of the interaction function.

Consider a neuron that is firing repetitive action potentials. Suppose we apply a perturbation to this spiking neuron, in the form of a current pulse. Depending on the strength and timing, this pulse may transiently impact the length of the *inter-spike intervals*—the duration between two successive spikes. If the pulse is weak enough, the neuron will have one different inter-spike interval and then continue to spike with same inter-spike interval it had before the perturbation. In the language of phase variables and limit cycles, this pulse may change the phase, θ_i,without changing the amplitude and shape of the limit cycle, at the time it is applied. In an experimental setting, this effect can be quantitatively measured as a difference between the expected phase ($\theta_{old}(t)$) in the absence of the perturbation and the perturbed phase ($\theta_{new}(t)$) in its presence [45, 32]. Winfree referred to the plot $\theta_{new} - \theta_{old}$ vs θ_{old} as the *phase response curve (PRC)* [136]. Depending on the perturbation strength and timing, we can either have a negative or positive response (or difference), which can delay or advance the firing of the neuron respectively (bring it closer to the spike time or go past it and be further from it). The PRC can be broadly categorized into two types: Type I, where the responses are strictly positive, and Type II, where there is a region of negative response as well. The PRC type of a neuron model can be closely

related to its excitability class (see Section 3.3). Typically class I oscillators exhibit Type I PRCs [56]. However, there is no strict correspondence between class II excitability and Type II PRCs.

Now for a pair of weakly coupled neurons, this current perturbation is the synaptic current. The coupling function G in the integral term in (4.35) is a measure of the stimulus (synaptic current) applied to the limit cycle of the postsynaptic neuron at a phase s if the presynaptic neuron is at phase $s+\psi$. The function Z is a sensitivity function that measures the impact of the perturbation due to G at a particular phase. Z can be thought as a measure of the infinitesimal phase response curve (iPRC) (or *phase-dependent sensitivity*) at the phase s [36, 45]. The product of the sensitivity function and the stimulus measure is averaged over one cycle. The resulting integral determines the net effect on the phase difference ψ.

4.2.2 Phase model for a network of weakly coupled oscillators

We conclude this chapter by extending the phase model for a pair of weakly coupled oscillators to the network level. In the network level extension for the corresponding biophysical model, the coupling term in the equation for the membrane potential V_i is in the form $\sum_{j=1}^{N} g_{syn} w_{ij} s_j (V_i - V_{syn})$ which can be represented as the following family of equations:

$$\frac{dX_i}{dt} = F(X_i) + \epsilon \sum_{j=1}^{N} w_{ij} G(X_i, X_j) \tag{4.37}$$

Note that in (4.37), $X_i = \left[V_i, m_i, h_i, n_i, w_i, s_i\right]^T$, as there is now an additional variable, which is the synaptic gating variable s_i. Accordingly, the vector function F will also have an additional dimension keeping track of the dynamics, $\dot{s}_i$. In the biophysical model, only the first dimension of the vector function G is non-zero since the coupling explicitly affects the membrane potential. $\{w_{ij}\}$ is the coupling matrix which describes the connectivity structure within the network, that is, information about which oscillators are coupled together.

Note that in (4.37), the coupling function G itself, is defined between any two neurons and is independent of network architecture and size. As such, the corresponding interaction function H can be defined for the phase deviation variables between any two neurons. Thus, the corresponding phase model for (4.37) is constructed as follows with the network

architecture and size kept unchanged.

$$\frac{d\varphi_i}{ds} = \varepsilon \sum_{j=0}^{N-1} w_{ij} H(\varphi_j - \varphi_i), \tag{4.38}$$

where H is as defined in 4.2.1. Recalling the relationship between θ_i and φ_i from Eq. (4.8), we may rewrite (4.38) in terms of θ_i as follows:

$$\frac{d\theta_i}{ds} = 1 + \varepsilon \sum_{j=0}^{N-1} w_{ij} H(\theta_j - \theta_i), \tag{4.39}$$

In general, it is impossible to analytically derive the interaction function. In the present thesis, H is numerically derived for a pair of weakly coupled biophysical model neurons.

4.2.3 Phase-locking

Consider a solution to the phase model Eq. (4.38) with weak coupling represented as follows

$$\theta_i(t) = \Omega t + \varphi_i(t), \tag{4.40}$$

where φ_i is the phase deviation determined by the interaction function H. We define a particular class of solutions such that the difference between two oscillators $\theta_i(t) - \theta_j(t)$, or equivalently $\varphi_i - \varphi_j$, is constant at steady state. This corresponds to a phase-locked state in the corresponding biophysical network, where adjacent neurons spike periodically with a fixed phase difference. We say that the solution is in-phase, if this steady state difference is 0 for all i and j [129]. In the biophysical network, this corresponds to a fully synchronized system, where all the neurons are spiking in unison [71]. In Chapter 5, we look for a special type of phase-locked solution where the corresponding network will break into subgroups of synchronized neural oscillators, a phenomenon known as clustering.

Chapter 5

Analysis of Cluster Solutions using a Phase-Model Approach

Our approach to studying the formation of neural assemblies within a network emphasizes the individual contributions of participating neurons. Specifically, we focus on solutions in networks of intrinsically oscillating neurons that phase-lock at steady state with fixed phase differences. This idea, briefly introduced at the end of Chapter 4, connects with the mathematical framework used to study the phase-locking behaviours in biophysical neuron models—phase model reduction. A *cluster solution* is a special type of phase-locked solution of the network, where neurons self-organize into synchronous clusters (i.e., with a zero phase difference) that maintain fixed inter-cluster phase differences. Cluster solutions have been extensively studied using phase models, particularly under the assumption of weak coupling—one that is often reasonable for biological neural networks. The conditions for the existence and stability of cluster solutions have been derived for various coupling architectures, including all-to-all coupling with a globally homogeneous [106, 15], and symmetric heterogeneous distribution [15, 97, 120] of synaptic weights.

In this chapter, we use the phase reduction of a system of weakly coupled oscillators, arranged on a one-dimensional ring, to study cluster solutions. We review the conditions of existence and stability described in [97, 106, 15] for these solutions under different connectivity schemes.

5.1 Phase model approach

Consider the phase model reduction that was derived for a weakly coupled system of the form (4.37) at the end of Chapter 4,

$$\frac{d\theta_i}{ds} = 1 + \varepsilon \sum_{j=1}^{N} w_{ij} H(\theta_j - \theta_i) \tag{5.1}$$

Recall that to arrive at Eq. (5.1), we assumed that, in the absence of coupling the corresponding network, (4.37), exhibits stable, homogeneous limit cycle solutions. Phase-locked solutions are periodic solutions of the network (4.37); these solutions can emerge in networks of neurons exhibiting limit cycle behaviour. To study these solutions, we assume that the network satisfied periodic boundary conditions. This corresponds to the neurons being arranged in a one dimensional ring, which imposes a symmetry on the network's coupling architecture. Specifically, the coupling matrix W, takes a circulant form:

$$W = \text{circ}\begin{pmatrix} w_0 & w_1 & w_2 & \dots & w_{N-1} \end{pmatrix} \tag{5.2}$$

which can be written equivalently as

$$w_{ij} = w_{(j-i) \bmod \text{N}} \tag{5.3}$$

In the corresponding biophysical neuron model, the synaptic coupling structure is identical for each neuron, resulting in a rotational symmetry. Following [97], if each neuron is coupled to r of its nearest neighbours on either side, we say the network has a connectivity radius r, that is $w_k, w_{N-k} > 0$ for all $k \leq r$. Additionally, we assume that there is no self-coupling ($w_0 = 0$).

We introduce a phase difference variable ψ_i defined as follows:

$$\psi_i = \theta_{i+1} - \theta_i, \qquad i \ (\text{mod } N) \tag{5.4}$$

The phase difference, ψ_i, describes the relative position of the oscillator θ_{i+1} with respect to θ_i within their respective cycles. If this difference is 0, then two oscillators are in-phase, that is, their cycles synchronize. The phase differences, Eq. (5.4), must satisfy the periodic boundary conditions for Eq. (5.1) since the model neurons are arranged in a one-dimensional ring. This gives the constraint

$$\sum_{i=1}^{N} \psi_i = 0 \bmod 2\pi \tag{5.5}$$

The period for each oscillator θ_i is 2π, and so Eq. (5.5) implies that the phase differences are distributed in some way within the interval $[0, 2\pi]$. The difference between any two oscillators θ_j and θ_i on the ring can defined in terms of the individual phase variables ψ_i.

$$\theta_j - \theta_i = \begin{cases} \sum_{s=0}^{j-i-1} \psi_{i+s} & i < j \\ \\ -\sum_{s=0}^{i-j-1} \psi_{i-1-s} & j < i \end{cases}, \tag{5.6}$$

where i and j are modulo N. In modular arithmetic form, Eq. (5.6) can be represented as $\sum_{s=0}^{j-i-1 \pmod N} \psi_{i+s \pmod N}$

We rewrite the model in Eq. (5.1), in terms of the phase difference variables (ψ_i) equipped with circulant coupling defined by (5.3) [15]:

$$\begin{aligned} \frac{d\psi_i}{ds} &= \frac{d\theta_{i+1}}{ds} - \frac{d\theta_i}{ds} \\ &= \varepsilon \left(\left(\sum_{j=1}^{N} w_{j-i-1(\text{mod N})} H(\theta_j - \theta_{i+1}) \right) - \left(\sum_{j=1}^{N} w_{j-i(\text{mod N})} H(\theta_j - \theta_i) \right) \right) \\ &= \varepsilon \left(\left(\sum_{k=1}^{N-1} w_k H(\sum_{s=0}^{k-1} \psi_{s+i+1 \pmod N}) \right) - \left(\sum_{k=1}^{N-1} w_k H(\sum_{s=0}^{k-1} \psi_{s+i \pmod N}) \right) \right) \\ &= \varepsilon \left(\sum_{k=1}^{N-1} w_k \left(H \left(\sum_{s=0}^{k-1} \psi_{s+i+1(\text{mod N})} \right) - H \left(\sum_{s=0}^{k-1} \psi_{s+i(\text{mod N})} \right) \right) \right) \end{aligned} \tag{5.7}$$

Note that the periodic boundary conditions defined in Eq. (5.5) reduce the dimensionality of (5.7) to $N-1$. However, to take advantage of the symmetry, we choose to work with the redundant $N-$dimensional phase-difference model.

Equilibrium solutions of the phase difference model (5.7) correspond to steady states in which the phase differences, ψ_i, remain constant. These solutions represent phase-locked states of the full system in Eq. (4.37). We now review the existence and stability of cluster solutions—phase-locked states in which oscillators within each subgroup are synchronized (i.e., with phase differences, (5.6), equal to zero). This analysis will be used to make predictions about what kind of cluster solutions can occur in the full model (4.37).

5.1.1 Existence of cluster solutions

To broadly investigate clustering within neural networks, we can consider two types of solutions: model-dependent and model-independent solutions [88]. Here, we prioritize generality by focusing on model-*independent* solutions for (4.37).

Recall that an equilibrium solution, ψ_{eq}, for (5.7) is determined by solving $\dot{\psi}_i = 0$. For these solutions to represent model-independent cluster solutions, they must be independent of the interaction function H and the weights (w_i) in (5.3). Consider a model-independent solution given by

$$\psi_{eq} = \begin{bmatrix} \psi & \psi & \dots & \psi \end{bmatrix}, \tag{5.8}$$

where the individual phase differences (ψ_i) are identical. Clearly (5.8) is an equilibrium solution for (5.7) which is independent of the interaction function, H and the coupling matrix, W. Eq. (5.8) corresponds to a periodic solution in which adjacent neurons phase-lock at the same phase i.e. ψ. Applying the constraint equation in (5.5) to (5.8), imposes restrictions on choice of ψ that lead to cluster solutions. In particular, we have

$$\sum_{i=1}^{N} \psi_i = N\psi = 0 \ (\text{mod } 2\pi) \implies \psi = 2\frac{k\pi}{N} \qquad k \in \{0, 1, .., N-1\} \tag{5.9}$$

Based on (5.9), the phase difference equations (5.7) can admit N cluster solutions satisfying Eq. (5.8). Depending on the values of k and N, each cluster solution falls into one of the following three categories, as described in [97]:

1. *Synchronized state* or *1-cluster* solution, depicted in Panel (A), Figure 5.1, for which $\psi = 0$. In the biophysical model, this corresponds to a periodic solution in which all cells in the network spike together, thereby forming a single cluster of synchronized oscillators.

2. *Splay state* or *N-cluster* solution, defined by $\psi = 2\frac{k\pi}{N}$, where k and N are relatively prime. From (5.8), we see that $N\psi = 2\pi k$, which implies that the cells within the network are uniformly distributed over k full periods, forming N distinct clusters as illustrated in Panel (B), Figure 5.1. In this case, no two neurons will synchronize, that is, each cluster will have only one neuron.

3. *n-cluster* solution, where n is a non-trivial factor of N. In particular, this solution arises where there exists a common integer factor l such that $N = l \cdot n$ and $k = l \cdot m$,

where m and n are relatively prime. The phase difference between adjacent oscillators is then given by:

$$\psi = 2\frac{m\pi}{n} \qquad gcd(m,n) = 1$$

Consider the phase difference between θ_1 and θ_{n+1}.

$$\theta_{n+1} - \theta_1 = \sum_{i=1}^{n+1} \psi_i = n\psi = 2m\pi = 0 \pmod{2\pi} \tag{5.10}$$

Eq. 5.10 implies that the corresponding neurons X_1 and X_{n+1} in the biophysical model will synchronize. Similarly, neurons X_q and $X_{q+n \pmod N}$ will also synchronize for $q = \{1, 2, .., N\}$. Applying this recursively, we find that neurons $X_1, X_{n+1}, ..., X_{(l-1)\cdot n+1}$ synchronize and form a cluster C_1. Repeating this process for $q = \{2, 3, .., n\}$, yields the remaining clusters $C_2, .., C_n$, thereby creating an ensemble of n clusters. Each cluster contains exactly $\frac{N}{n}(= l)$ cells, as illustrated in Panel (C), Figure 5.1. As an example, if N is even, then (5.7) will always admit a $2-$cluster solution with $\psi = \pi$, also known as the *anti-phase state*. In this case, the corresponding biophysical network splits into two clusters, C_1 and C_2, each containing exactly $\frac{N}{2}$ oscillators, that are given by:

$$C_1 = \{1, 3, 5, .., N-1\} \qquad C_2 = \{2, 4, 6, .., N\}$$

The numbers in the cluster refer to the cell indices of the corresponding cells in the network.

Note that each of the solutions described above is characterized by clusters containing an identical number of oscillators. This particular type of cluster solution is called a *symmetric cluster solution*. In general, (5.7) *will always admit the in-phase or synchronized solution*. If n divides N, then (5.4) admits an $n-$cluster solution in which the phase difference between adjacent neurons is given by $\psi = \frac{2\pi m}{n}$ for $m < n$. In the present thesis, we consider the stability analysis for cluster solutions belonging to any one of the three types described above. Depending on the value of the phase difference ψ, we can determine the firing order of clusters, which has been described in Appendix C.1.

5.1.2 Stability of the cluster solutions

To investigate the stability of the symmetric cluster solutions described in the previous section, we linearize the system (5.7) about the equilibrium solution (5.8). Rewriting (5.7)

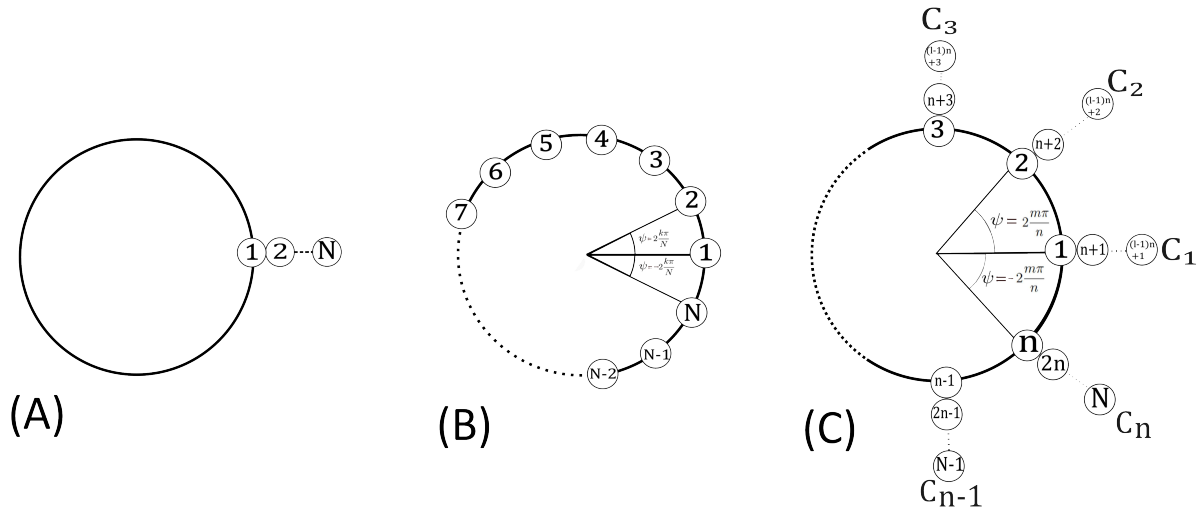


Figure 5.1: Three categories of symmetric cluster solutions that can arise for a periodic solution corresponding to identical phase differences between adjacent neurons. The nodes in each diagram represent a spiking neuron and how they are arranged in phase space from 0 to 2π **(A)** In-phase or the $1-$cluster solution in which all the neurons spike in unison with a 0 phase difference. **(B)** Splay-state or $N-$cluster solution, where each neuron forms its own cluster and no two neurons synchronize. $\psi = \frac{2k\pi}{N}$, with $gcd(k, N) = 1$ **(C)** $n-$cluster solution, win which the neurons selectively synchronize and organize into clusters C_i, defined by $\{i, i+n, \ldots, N-n+i\}$ for $i = \{1, 2, \ldots, n\}$. Neurons within each cluster C_i are synchronized with one another. In this case, $\psi = \frac{2\pi m}{n}$ as described in the main text.

as

$$\frac{d\psi_i}{dt} = f_i(\psi_1, \psi_2, \ldots, \psi_N),$$

the linearization can be written as

$$\Psi' = \mathbf{J}(\psi)\Psi \tag{5.11}$$

where $\Psi = (\psi_1, \psi_2, \ldots, \psi_N)^T$ and $\mathbf{J}$ is the jacobian of the right-hand side of the system (5.7). Recall that the entries of $\mathbf{J}$ are computed as follows

$$\mathbf{J_{ij}} = \partial_{\psi_j} f_i = \begin{cases} -\varepsilon \sum_{k=1}^{N-1} w_k \cdot H'\left(\sum_{s=0}^{k-1} \psi_s\right) & i = j \\ \varepsilon \left[\sum_{k=(j-i)\bmod \mathrm{N}}^{N-1} w_k \cdot H'\left(\sum_{s=0}^{k-1} \psi_{(s+i+1)\bmod \mathrm{N}}\right) \right. & \\ \left. - \sum_{k=(j-i+1)\bmod \mathrm{N}}^{N-1} w_k \cdot H'\left(\sum_{s=0}^{k-1} \psi_{(s+i)\bmod \mathrm{N}}\right) \right] & i \neq j \end{cases} \tag{5.12}$$

Evaluating (5.12) at the equilibrium (5.8), we obtain the following jacobian entries:

$$\mathbf{J_{ij}} = \begin{cases} -\varepsilon \sum_{s=1}^{N-1} w_s \cdot H'(s\psi) & i = j \\ \varepsilon \left(w_{(j-i)\bmod \mathrm{N}} \cdot H'\left((j-i)\bmod \mathrm{N}\ \psi\right)\right) & i \neq j \end{cases} \tag{5.13}$$

Eq. (5.13) shows that the jacobian matrix $\mathbf{J}$ is a circulant matrix. In particular, $\mathbf{J}$ has the following circulant form:

$$\mathbf{J} = \varepsilon\, circ\begin{pmatrix} c_0 & c_1 & c_2 \ldots & c_{N-1} \end{pmatrix} \tag{5.14}$$

where $c_0 = \sum_{s=0}^{N-1} w_s \cdot H'(s\psi)$ and $c_k = w_k \cdot H'(k\psi), k = 1, \ldots, N-1$

In [52], the eigenvalues of a general circulant matrix are derived. Using this result, the eigenvalues of (5.14) are given by

$$\lambda_j = -\varepsilon \sum_{k=0}^{N-1} w_k \cdot H'(k\psi)\left(1 - e^{i\left(\frac{2\pi kj}{N}\right)}\right) \qquad j \in \{0, 1, .., N\}, \tag{5.15}$$

where $j = 0$ corresponds to a zero eigenvalue, which will always exist. This degeneracy arises as a consequence of the sum constraint described in Eq. (5.5). Essentially, the existence of the zero is due to the redundancy in the extra dimension represented in the model, so we may ignore this eigenvalue in the stability analysis of the cluster solution. We now state the necessary condition for a symmetric cluster solution ψ to be asymptotically stable, as presented in the theorem from [15].

Theorem 5.1.1. *The equilibrium point* $\psi = \frac{2\pi k}{N}$ $k \in \{0, 1, \ldots, N-1\}$ *, and the corresponding cluster solution for the phase difference model* (5.7) *is asymptotically stable if the* μ_j *defined below is positive for all* $1 < j < \lfloor \frac{N}{2} \rfloor$

$$\mu_j = \sum_{k=1}^{N-1} w_k H'(k\psi) \left(1 - \cos\left(\frac{2\pi kj}{N}\right)\right) \tag{5.16}$$

and is unstable if at least one of the μ_j *is negative.*

Proof. A symmetric cluster solution of (5.7) with a phase-difference ψ, is asymptotically stable if the real part of all the eigenvalues computed in (5.15) corresponding to $j \geq 1$ is strictly negative.

$$\begin{aligned}
\mathbf{Re}(\lambda_j) &= -\varepsilon \sum_{k=1}^{N-1} w_k \cdot \mathbf{Re}\left(H'(k\psi)\left(1 - e^{i\left(\frac{2\pi kj}{N}\right)}\right)\right) \qquad j \in \{1, .., N\} \\
&= -\varepsilon \sum_{k=1}^{N-1} w_k \cdot \left(H'(k\psi)\mathbf{Re}\left(1 - e^{i\left(\frac{2\pi kj}{N}\right)}\right)\right) \\
&= -\varepsilon \sum_{k=1}^{N-1} w_k \cdot \left(H'(k\psi)\left(1 - \cos\left(\frac{2\pi kj}{N}\right)\right)\right)
\end{aligned} \tag{5.17}$$

We define a variable μ_j as follows

$$\mu_j = \sum_{k=1}^{N-1} w_k \cdot \left(H'(k\psi)\left(1 - \cos\left(\frac{2\pi kj}{N}\right)\right)\right) \qquad j \in \{1, .., N\}$$

Substituting μ_j in (5.17), the symmetric cluster associated with ψ is stable if

$$\begin{aligned}
\lambda_j = -\varepsilon\mu_j < 0 \qquad & \forall\, j \in \{1, 2, .., N\} \\
\iff \mu_j > 0 \qquad & \forall\, j \in \{1, 2, .., N\}
\end{aligned} \tag{5.18}$$

Using the fact that the cosine function is even and 2π periodic, the following is true

$$\cos\left(\frac{2\pi kj}{N}\right) = \cos\left(2\pi k - \frac{2\pi kj}{N}\right) = \cos\left(\frac{2\pi k(N-j)}{N}\right) \tag{5.19}$$

which implies that $\mu_j = \mu_{N-j}$, allowing us to reduce the number of eigenvalues to compute in (5.18) to verify the stability.

$$\mu_j > 0 \qquad \forall\, j \in \left\{1, 2, .., \left\lfloor \frac{N}{2} \right\rfloor\right\} \tag{5.20}$$

□

Below, we state a few of the implications of Theorem 5.1.1, which have been proven in [15]

1. *The synchronized state ($\psi = 0$) will always exist for any network configuration, regardless of how the coupling is set-up and is stable if and only if $H'(0) > 0$.* The stability of the in-phase solution is, therefore independent of the size of the network, N, and the coupling weights, w_i. This makes the analysis of full synchrony particularly powerful, as the stability can be determined by verifying a single condition.

2. *The 2-cluster or the anti-phase solution ($\psi = \pi$) will always exist for a network of size N that is even.* It is a periodic solution in which every adjacent neuron is out-of-phase with one another by exactly half a period. For $N = 2$, the anti-phase state is stable if $H'(\pi) > 0$. For $N > 2$, the stability is independent of the coupling configuration and is stable if both $H'(0)$ and $H'(\pi)$ are strictly positive. It becomes unstable if $H'(\pi) < 0$. However, this is not a strict condition– the anti-phase state can still be stable even if either $H'(0)$ or $H'(\pi)$ is non-positive. We see this in Chapter 7 where the anti-phase state is stable even though the in-phase state is unstable for a specific set of parameters.

5.2 Stability analysis for symmetric bi-directional coupling

We now assume that the coupling strengths in Eq. (5.3) are *symmetric*, meaning that $w_k = w_{N-k}$ for $k = \{1, 2, \ldots, N-1\}$. Under this assumption, the coupling weight from each cell to its k^{th} neighbour on either side is equal. As a result, the corresponding coupling matrix, W, satisfies

$$W = \begin{cases} circ\begin{pmatrix} 0 & w_1 & w_2 & \ldots & w_{\frac{N-1}{2}} & w_{\frac{N-1}{2}} & \ldots & w_2 & w_1 \end{pmatrix} & \text{For } N \text{ odd} \\ \\ circ\begin{pmatrix} 0 & w_1 & w_2 & \ldots & w_{\frac{N}{2}-1} & w_{\frac{N}{2}} & w_{\frac{N}{2}-1} & \ldots & w_2 & w_1 \end{pmatrix} & \text{For } N \text{ even} \end{cases} \tag{5.21}$$

In this configuration, the strength of the synaptic influence of neuron i on neuron j, is equivalent to that of neuron j on i. Applying Theorem 5.1.1, to the phase difference model (5.7), equipped with a coupling architecture defined by (5.21), we get the following

expressions for μ_j

$$\mu_j = \begin{cases} \sum_{k=1}^{\lfloor \frac{N}{2} \rfloor} w_k (H'(k\psi) + H'(-k\psi)) \left(1 - \cos\left(\frac{2\pi kj}{N}\right)\right), & N \text{ is odd} \\ w_m H'(m\psi)\left(1 - (-1)^j\right) + \sum_{k=1}^{m-1} w_k (H'(k\psi) + H'(-k\psi)) \left(1 - \cos\left(\frac{\pi kj}{m}\right)\right), & N = 2m \text{ is even} \end{cases} \tag{5.22}$$

Theorem 5.2.1. *The equilibrium point $\psi = \frac{2\pi p}{N}, p \in \{1, 2, \ldots, N\}$, and the associated cluster solution for the phase difference model (5.7), equipped with a bidirectional symmetric coupling described by (5.21), is asymptotically stable if μ_j defined in Eq. (5.22) is strictly positive for all $j \in \{1, 2, \ldots, \lfloor \frac{N}{2} \rfloor\}$ and unstable if at least one $\mu_j < 0$.*

As a consequence of Theorem 5.2.1, we have that *the symmetric clusters associated with ψ and $(2\pi - \psi)$ are strongly related.* In particular, they share the same stability owing to the 2π periodicity of the interaction function H. In Eq. (5.22), we observe that the derivative of the odd part of the interaction function appears, namely:

$$H'_{odd}(\psi) = \left(\frac{1}{2}\left(H(\psi) - H(-\psi)\right)\right)' = \frac{1}{2}\left(H'(\psi) + H'(-\psi)\right)$$

It follows that $H'_{odd}(2\pi - k\psi) = H'_{odd}(k\psi)$. Thus, the symmetric clusters associated with ψ and $2\pi - \psi$ share the same stability.

Below we examine two special cases of bi-directional symmetric coupling and review the associated stability results for each one as described in [97, 15].

5.2.1 Nearest neighbours

We focus on the configuration of the network (5.7), where each neuron is connected only to its nearest neighbours, i.e., the coupling radius r is 1. In particular, the coupling matrix for this network is given by (5.21), with $w_1 \neq 0$ and $w_j = 0, j = 2, \ldots N$. We review the stability result discussed in [97] by applying Theorem 5.2.1 to this network. For $j \in \{1, 2, \ldots, \lfloor \frac{N}{2} \rfloor\}$, μ_j in (5.21) reduces to the following

$$\mu_j = w_1 \left(H'(\psi) + H'(-\psi)\right) \left(1 - \cos\left(\frac{2\pi j}{N}\right)\right) = 2w_1 H'_{odd}(\psi) \left(1 - \cos\left(\frac{2\pi j}{N}\right)\right) \quad (5.23)$$

In (5.23), w_1 and $\left(1 - \cos\left(\frac{2\pi j}{N}\right)\right)$ are nonnegative. In order to guarantee stability, we only need to consider the expression $H'(\psi) + H'(-\psi)$ which is independent of j, yielding the following result.

Corollary 5.2.1.1. *A symmetric cluster solution associated with the equilibrium point ψ for a network equipped with nearest neighbour coupling is asymptotically stable if and only if $H'_{odd}(\psi) > 0$*

Corollary 5.2.1.1 has significant implications. Notable, it shows that the stability of a symmetric cluster solution associated with a phase difference ψ is independent of the size of the network N, when the network has symmetric nearest neighbour coupling. This is a powerful result, especially considering the fact that the number of possible $n-$cluster solutions for a phase difference ψ, increases with N, yet they will share the same stability regardless of network size.

This connectivity scheme can be used to represent networks with relatively sparse connections, such as those found within the CA1 sub-hippocampal region. To study the recurrent connections within the CA3-sub hippocampal network, we extend the coupling radius in (5.21), to $r = \lfloor \frac{N}{2} \rfloor$ so that each neuron connects to all other neurons in the network.

5.2.2 All-to-all coupling

The CA3 sub-hippocampal region is densely populated with excitatory pyramidal neurons and, importantly, it is a recurrently connected region as described in Section 2. To study an excitatory homogeneous CA3 recurrent network of pyramidal neurons, we can extend the coupling radius r to $\lfloor \frac{N}{2} \rfloor$. In this case, $w_j \neq 0$, for all $j \in \{1, 2 \ldots \lfloor \frac{N}{2} \rfloor\}$ in Eq. (5.3). For arbitrary values of w_i, the stability analysis follows from Theorem 5.2.1. Below, we consider two different configurations of (5.3) for all-to-all coupling, and their corresponding stability analyses as described in [15, 106].

Distance dependent (global heterogeneous coupling)

In real neural networks, the coupling strengths are likely to be heterogeneous. Thus, it is worthwhile to study configurations in which all the weights w_i in (5.21) are different,

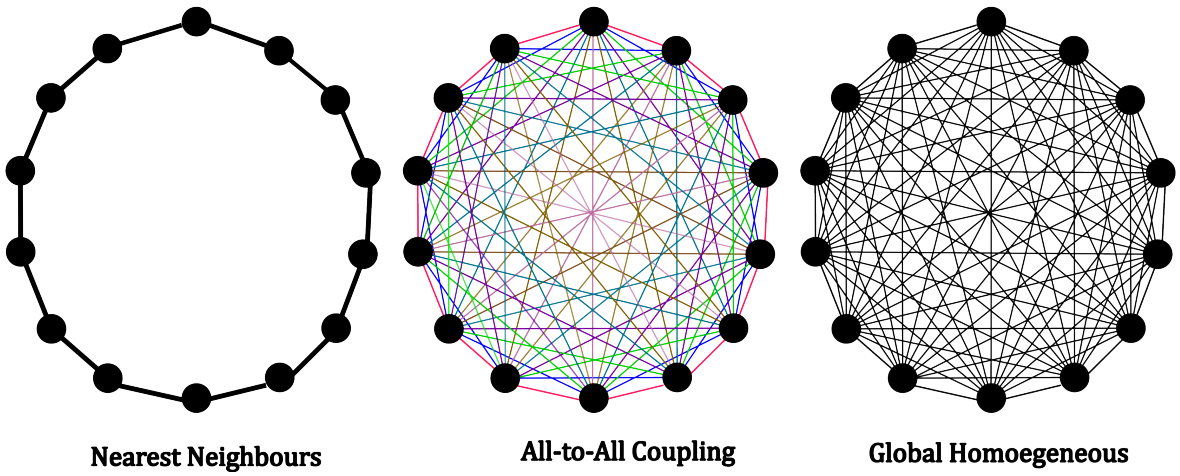


Figure 5.2: Three types of coupling considered in our analysis. Each node in the ring diagram represents a neuron. These diagrams convey information about which neurons are coupled together via reciprocal synapses, indicated by the lines joining two nodes. For the nearest neighbours, each neuron i is coupled to its neighbours $i+1 \pmod N$ and $i-1 \pmod N$. In the other two cases each neuron is synaptically coupled to all of its neighbours. The black lines for the global homogeneous case represent identical synaptic weights.

but not random. This way, we introduce a *selective heterogeneity* in the synaptic weights. In particular, we consider a network where the relative coupling strengths for a neuron decrease with distance from the neuron. This does not necessarily reflect a physical distance in the corresponding network, but rather a hierarchy in the strengths of the coupling to all other neurons in the network. We call this type of coupling distance-dependent [15]. The corresponding coupling matrix W will satisfy (5.21) with $w_i = w_1 \cdot p^{i-1}$ for some non zero $p < 1$:

$$W = w_1 \cdot circ\begin{pmatrix} 0 & 1 & p & p^2 & \cdots & p^2 & p & 1 \end{pmatrix}$$

Applying Theorem (5.2.1) to this system, (5.22) reduces to the following [15] :

$$\mu_j = w_1 \cdot \sum_{k=1}^{N-1} p^{k-1}(H'_{odd}(k\psi) + H'_{odd}(-k\psi)) \left(1 - \cos\frac{2\pi kj}{N}\right) > 0 \qquad \forall j \in \{1, .., \lfloor \frac{N}{2} \rfloor\}, \tag{5.24}$$

for N odd and

$$\mu_j = w_1 \cdot \left(p^{\frac{N-3}{2}} H\left(m\psi\right)\left(1 - (-)^j\right) + 2\sum_{k=1}^{m-1} p^{k-1}(H'_{odd}(k\psi) + H'_{odd}(-k\psi)) \left(1 - \cos\frac{2\pi kj}{N}\right) > 0 \right) \qquad \forall j \in \{1, .., \lfloor \frac{N}{2} \rfloor\}, \tag{5.25}$$

for $N = 2m$, even.

Unlike the nearest-neighbours case, the stability of an equilibrium point ψ associated with a cluster solution for the phase difference model (5.7), equipped with this type of coupling, *will depend on the size of the network.*

As we can see, for arbitrary values of w_j, we cannot derive a minimal stability condition like in the case of nearest neighbours. Thus, to determine stability we will be required to compute the values of all the μ_j in Eq. (5.22), associated with a cluster solution. This leads us to consider a special case of all-all coupling where minimal stability conditions can be computed.

Global homogeneous coupling

This is a special case for a network with all-all coupling, in which all the weights w_j in Eq. (5.21) are set to 1, i.e., the coupling matrix is $W = circ\begin{pmatrix} 0 & 1 & 1 & \cdots & 1 & 1 \end{pmatrix}$. Applying

Theorem 5.1.1 shows that a symmetric cluster solution associated with the equilibrium point ψ is asymptotically stable if and only if

$$\mu_j = \sum_{k=1}^{N-1} H'(k\psi)\left(1-\cos\frac{2\pi kj}{N}\right) > 0 \qquad \forall j \in \{1,..,\lfloor\frac{N}{2}\rfloor\} \tag{5.26}$$

This set of inequalities can be modified such that the conditions outlined in (5.26) is independent of the size of the network N and the equilibrium point ψ. Essentially, we can redefine μ_j in (5.26) to generalize the stability analysis of a symmetric $n-$cluster solution where $n < N$.

$$\begin{aligned}\mu_j &= \sum_{k=1}^{n-1}\left(H'\left(\frac{2\pi k}{n}\right)\right)\left(1-\cos\frac{2\pi kj}{n}\right) \qquad 1 \le j \le \lfloor\frac{n}{2}\rfloor \\ \hat{\mu}_0 &= \sum_{k=0}^{n-1}\left(H'\left(\frac{2\pi k}{n}\right)\right)\end{aligned} \tag{5.27}$$

Eq. (5.27) recovers the results from [106]. Since all the coupling weights are identical, networks with global homogeneous coupling are unaffected by any rearrangement of indices [6, 134]. In this case, the stability of a symmetric cluster solution where the adjacent phase differences are not necessarily equal can also be determined by meeting the condition outline in Eq. (5.27). Thus, Eq. (5.27) determines the stability for any symmetric $n-$cluster solution in a network equipped with a globally homogeneous distribution of synaptic weights.

Chapter 6

Reduced Traub Miles' Model of a Pyramidal Neuron

In 1982, Traub and Miles developed a biologically plausible model of a CA3 pyramidal neuron that successfully replicated distinct firing patterns observed in both in vivo and in vitro experiments [131]. This model consisted of 19-compartments containing up to four active currents with kinetics inferred from various sources of voltage-clamp experiments performed on guinea pig and invertebrate hippocampal slices [130, 5, 75, 76]. The resulting model was useful for studying the population behaviours of pyramidal neurons in the hippocampus and was capable of exhibiting realistic bursting patterns. In particular, this model could demonstrate the appropriate increase in firing frequency with the depolarization.

A single compartmental reduction of a biophysical model is faster to simulate while retaining relevant features enabling us to build networks that can replicate selective biological behaviours. In 1998, Ermentrout and Kopell [34] constructed a model of the hippocampus circuit composed of pyramidal neurons and interneurons to study the effect of synaptic coupling and conduction delays on neural synchrony. The pyramidal neuron model was derived by reducing the Traub–Miles model to a single compartment. In this reduced model, both calcium currents and calcium-activated potassium currents were omitted.

However, neither model accounts for the muscarinic K^+ current (M-Current) which has been implicated in hippocampal dynamics through cholinergic neuromodulation [55, 54, 135, 7, 41]. In [20], Emrentrout and Crook constructed a 2-compartmental reduction of the Traub-Miles model as an extension of previous work, [113, 21] to study the effect of spike frequency adaptation (SFA) on neural synchrony within cortical networks. To incorporate

spike frequency adaptation into their model, they added two different currents, one of which was the M-current.

In 2000, Ermentrout and Kopell examined the distinct synchronization properties of gamma and beta rhythms observed in cortical networks [81]. One of the key features contributing to these rhythms was the involvement of an M-current, which had been absent in their initial model [34]. The dynamics for the M-current were modelled using kinetics described in [21, 20]. The reduced model was later utilized and validated by Olfusen and Kopel [108], to study the mechanisms underlying the transition between gamma and beta rhythms, specifically those induced by the cholinergic modulation of M-current.

This is the model we use to conduct our investigation into the effect of the acetylcholine sensitive M-current on the neural synchrony in a network of hippocampal CA3 pyramidal neurons. This model has been successful in replicating behaviours supported by experimental evidence, in particular, the M-current induced beta rhythms [81, 108].

6.1 Model description

The final model is a single-compartmental representation of a pyramidal neuron in the rat hippocampus as illustrated in Figure 6.1. It is a conductance based model with parameters taken from [34, 81, 21, 108]. The model includes a fast sodium current (I_{Na}), a delayed rectifier potassium current (I_K), a slow voltage dependent non-inactivating potassium current (I_M), a leak current (I_L) and an applied current (I_{app}). This leads to the following model for the membrane potential:

$$C\frac{dV}{dt} = I_{app} - I_L - I_K - I_{Na} + I_M + I_{syn}, \tag{6.1}$$

where each current was modelled using a Hodgkin-Huxley formalism described in section 3.2.2. The description for each current is summarized below.

Transient Na^+ current (I_{Na})

This current is given by the following equation

$$I_{Na} = g_{Na} \cdot m^3 \cdot h \cdot (V - V_{Na}) \tag{6.2}$$

In the original Traub-Miles model, steady-state values m_∞ and h_∞ and time constants τ_m and τ_h were based on a model for spinal interneurons [130]. The rate functions for

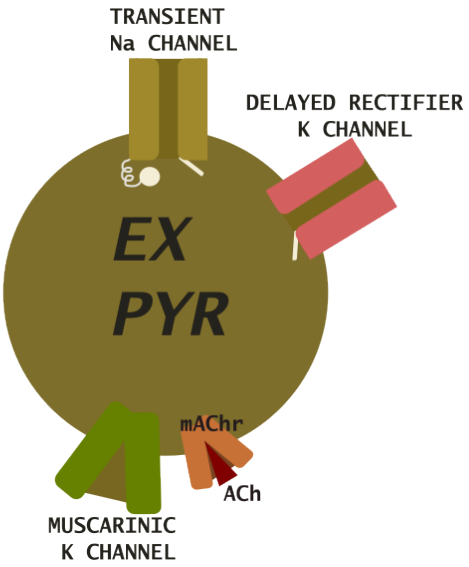


Figure 6.1: Reduced Traub-Miles with M-current

the activation variable m and the inactivation variable h were modified for the single compartment model by Ermentrout and Kopell [34, 81] to obtain:

$$\alpha_m(V) = \frac{0.32(54+V)}{1-\exp\left(-\frac{54+V}{4}\right)} \qquad \beta_m(V) = \frac{0.28(V+27)}{\exp\left(\frac{V+27}{5}\right)-1} \tag{6.3}$$

$$\alpha_h(V) = 0.128\exp\left(\frac{-(V+50)}{18}\right) \qquad \beta_h(V) = \frac{4}{1+\exp\left(-\frac{V+27}{5}\right)} \tag{6.4}$$

The reversal potential V_{Na} is set at $+50\text{mV}$. The maximal conductance g_{Na} is chosen to be $100\,\text{mS/cm}^2$.

Delayed rectifier K^+ current (I_K)

This current is given by the following equation

$$I_K = g_k \cdot n^4 \cdot (V - V_K). \tag{6.5}$$

The steady state activation variable n_∞ and time constant τ_n are also taken from a previous interneuron model [130]. In [34], the kinetics for the rate functions were modified as follows:

$$\alpha_n = \frac{0.032(V+52)}{1-\exp\left(\frac{V+52}{5}\right)} \qquad \beta_n = 0.5\exp\left(\frac{-(57+V)}{40}\right) \tag{6.6}$$

The reversal potential V_K is maintained at -100 mV and the maximal conductance parameter g_K is chosen to be 80mS/cm^2 .

Muscarinic K^+ current (I_m)

This current takes the following form:

$$I_M = g_M \cdot w \cdot (V - V_K) \tag{6.7}$$

The kinetic model for the activation variable, w, was taken from [21, 20] and adjusted by Ermentrout and Kopell [81] as follows:

$$w_\infty(V) = \frac{1}{1+\exp\left(\frac{-(V+35)}{10}\right)} \tag{6.8}$$

$$\tau_w(V) = \frac{400}{3.3\exp\left(\frac{V+35}{20}\right)+\exp\left(-\frac{V+35}{20}\right)} \tag{6.9}$$

$$\frac{dw}{dt} = \frac{w_\infty(V) - w}{\tau_w(V)} \tag{6.10}$$

The maximal conductance parameter g_M is typically set around 1mS/cm^2, however this is one of the parameters that is varied during our analysis.

Leakage current (I_L)

This current is modelled as follows:

$$I_L = g_L \cdot (V - V_L) \tag{6.11}$$

where g_L is $0.1\ \text{mS/cm}^2$. The reversal potential V_L is set at $-67\ \text{mV}$.

Total synaptic current ($I_{synaptic}$)

The synaptic current is composed of the excitatory and inhibitory synaptic inputs that are received by the neuron. For a pyramidal neuron, if it receives input from another pyramidal neuron, the nature of the synapse is excitatory (g_{EE}), and inhibitory (g_{IE}) if it receives input from an inhibitory neuron like an inter-neuron. Regardless, each type of synaptic current has the following form.

$$I_{syn,i} = g_{syn,i} \cdot (V - V_{syn,i}) \tag{6.12}$$

$$I_{syn} = \sum I_{syn,i} \tag{6.13}$$

where $g_{syn,i}$ is either g_{EE} or g_{IE}. In [81] and [108], the excitatory synapses were modelled as AMPA-mediated ($V_{syn} = 0$) and the inhibitory synapses were $GABA_B$-mediated ($V_{syn} = -80$).

6.1.1 Network level extension

In the present thesis, we investigate the M-current-induced synchrony in a network of identical neurons that are synaptically coupled. We consider only one type of hippocampal neuron; the CA3 pyramidal neuron. Thus all the synapses in the network will be excitatory. As described in [81, 108], we will assume these are AMPA-mediated. The synaptic current is thus modelled as:

$$I_{syn} = g_{syn}(t) \cdot (V - V_{syn}) \tag{6.14}$$

For an AMPA-mediated synapse, V_{syn} is set to 0 mV [36] in Eq. (6.14) with the conductance $g_{syn}(t)$ modelled as follows

$$g_{syn}(t) = g_{syn} \cdot s(t), \tag{6.15}$$

where g_{syn} is maximal synaptic conductance and s is the synaptic variable denoting the fraction of open channels. s is modelled with Destexhe kinetics as described in section 3.4

$$\frac{ds}{dt} = \alpha_s(V_{pre}) \cdot (1 - s) + \beta_s(V_{pre}) \cdot s, \tag{6.16}$$

where the V_{pre} refers to the voltage of the pre-synaptic neuron. The corresponding rate functions are taken from [81], giving us:

$$\frac{ds}{dt} = 5\left(1 + \tanh\left(\frac{V_{pre}}{4}\right)\right) \cdot (1 - s) + \frac{s}{2} \tag{6.17}$$

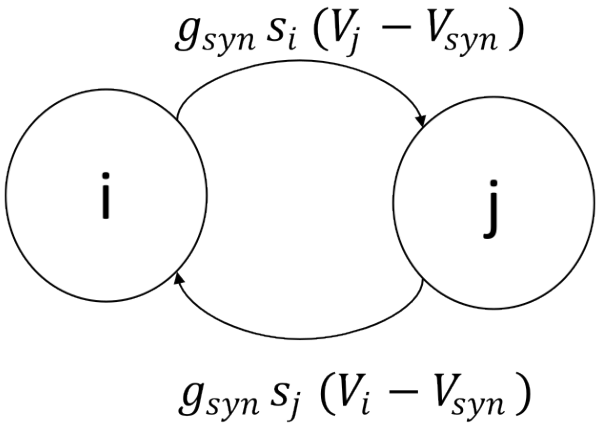


Figure 6.2: Synaptically coupled RTM model neurons

For a network of N neurons, we define a coupling matrix W describing the connectivity architecture within the network (which neurons are connected) and the relative strengths of the coupling. Each entry W_{ij} is a value between 0 and 1, with 0 indicating that neuron i and j are not connected and 1 indicating they are connected at the maximum strength as illustrated in Figure 6.2. The corresponding model for a network of N RTM model neurons that are coupled with an excitatory synapse is described by:

$$\begin{aligned}\frac{dV_i}{dt} &= I_{app} - g_L(V_i - V_L) - g_M w_i(V_i - V_K) - g_{Na} m_i^3 h_i(V_i - V_{Na}) \\ &\quad - g_K n_i^4(V_i - V_K) - \frac{g_{syn}}{N}\sum_{j=1}^{N} W_{ij} s_j (V_i - V_{syn})\end{aligned}$$

$$\frac{dX_i}{dt} = \alpha_{X_i}(1 - X_i) + \beta_{X_i} X_i \qquad X = \{m, h, w, n\} \tag{6.18}$$

$$\frac{ds_i}{dt} = 5\left(1 + \tanh\left(\frac{V_i}{4}\right)\right)(1 - s_i) - \frac{s_i}{2} \qquad i = \{1, 2, .., N\}$$

In Eq. (6.18), g_{syn} is normalized by N to reflect the individual contributions from the other cells.

6.2 Effect of M-current on the steady-state behaviour (bifurcation analysis)

In Section 3.3, we discussed how a neuron may transition from rest to a state of repetitive firing by applying a sufficiently strong constant external current. This transition typically occurs through a bifurcation—either through a saddle node on an invariant circle (SNIC) or a subcritical Hopf bifurcation (H.B). Based on the manner of transition to periodic firing, the excitability of a neuron can be classified as either type I, associated with a SNIC bifurcation, or type II, associated with a Hopf bifurcation. Cholinergic suppression of the M-current has been shown to switch pyramidal neurons from exhibiting type II to type I excitability. [39, 126]. In particular, an M-current induced Bogdanov Takens bifurcation underlies this switch in neuronal excitability [36], which was studied for a general conductance based model in [4]. The Bogdanov Takens is a co-dimension 2 bifurcation, that arises through the variation of the I_{app} and g_M. We reproduce this result for the RTM model presented in [4] by plotting two sets of bifurcation curves in the (I_{app}, g_M) and (I_{app}, V) parameter space respectively.

In Figure 6.3, we plot the two-parameter bifurcation curves where the applied current (I_{app}) and g_M are varied. The transition from type I to type II occurs around the Bogdanov Takens point (labelled B.T) at $g_M \simeq 0.03$. As g_M increases, the two fold points merge at a cusp point (labelled C.P). Additionally, we see a curve of Hopf points emerging from the B.T point. These curves additionally provide insight into suitable values of the externally applied current (I_{app}) that allow the RTM model neuron to exhibit stable limit cycle oscillations for a given maximum value of g_M. We use this in Section 6.3 to identify appropriate parameters for deriving a phase model approximation of the RTM model.

In Figure 6.4 we plot the steady states as the M-current conductance (g_M) increased, demonstrating a change in the qualitative dynamics as the M-current is increased. In particular, we can see that at $g_M = 0$, when there is no M-current, the stable oscillations emerge as the stable equilibrium is destroyed in a saddle-node bifurcation. This corresponds to a SNIC bifurcation indicating Class I excitability. This switches to Class II excitability when g_M is increased to 5. In this case, we see oscillations emerge through a Hopf Bifurcation as a stable equilibrium becomes unstable.

We further demonstrate this switch in the dynamics by plotting the spiking frequencies for various amplitudes of the constant current, also known as the the frequency-current (F/I) curves, at the two different values of g_M, illustrated in Figure 6.5. In the absence of an M-current, the model neuron transitions readily from rest to spiking, beginning at arbitrarily low frequencies in response to small currents, characteristic of a type I neuron.

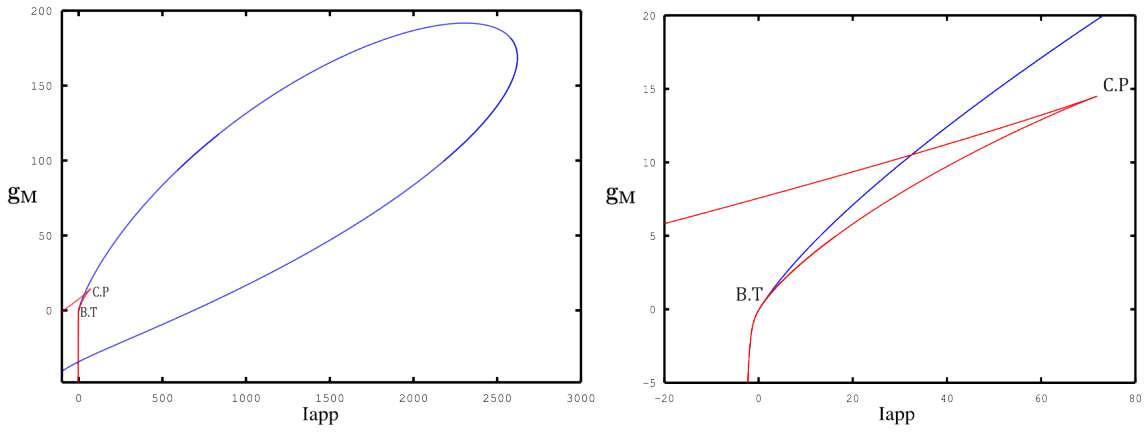


Figure 6.3: Bifurcation curves in (I_{app}, g_M) parameter space. *Left.* Full two-parameter bifurcation diagram *Right.* Zoomed-in view near the red curves, highlighting the region relevant to our analysis.

The firing frequencies are also highly sensitive to the applied current, with the neuron exhibiting a broad frequency range as the current increases. In contrast, when the M-current conductance is sufficiently large ($g_M = 5$), the neuron begins firing at a minimum positive frequency and exhibits a relatively narrow frequency band over the same range of applied currents.

6.3 Parameter choice for phase model approximation

To derive a phase model approximation of the RTM model, we require each neuron in Eq. (6.18) to be an oscillator in the absence of coupling ($g_{syn} = 0$), i.e., they must exhibit *stable* periodic oscillations in isolation (see Chapter 4).

This means the neuron must receive a large enough input (I_{app}) that can set it into a state of repetitive firing. Based on our bifurcation study in the previous section, we identify two values of g_M for which the intrinsic properties of the neuron change significantly; $g_M = 0$ and 5. We also consider two additional points between $g_M = 0$ and 5 and beyond $g_M = 5$ in our bifurcation study, $g_M = 2$ and 10 respectively.

The bifurcation analysis in Figure. 6.4, suggests that an external current, I_{app}, of 60 μA is sufficient to initiate stable limit cycles in an RTM model neuron with M-current

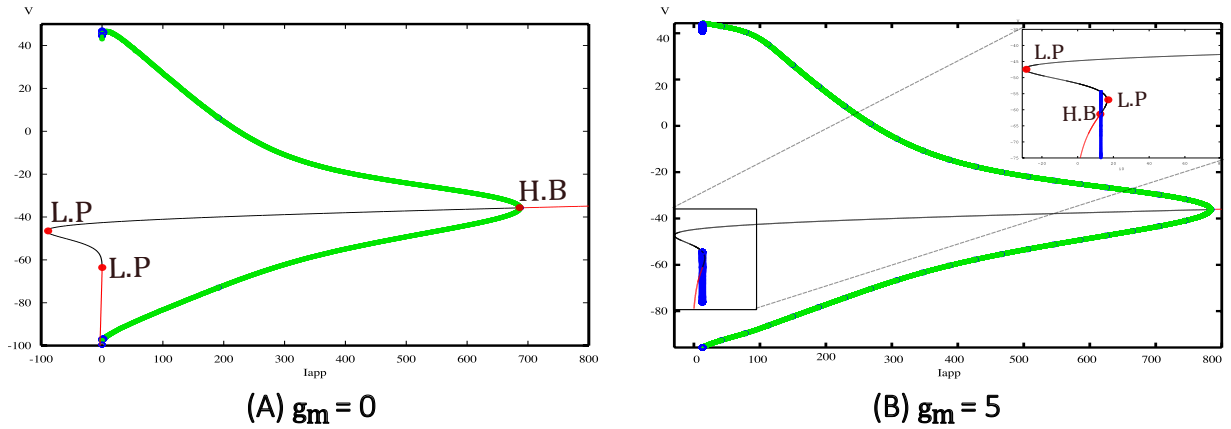


Figure 6.4: Steady states as a function of current (I_{app}) for the RTM model at two values of g_M, before and after the Bogdanov Takens point (B.T). The red curves indicate stable points and the black curves indicate unstable points. The green curves above and below the fixed-point curve (in black) correspond to the maximum and minimum voltages along the periodic orbits. **(A)** One parameter bifurcation curve for g_M before the BT point ($g_M = 0$) when the neuron is exhibiting type I dynamics or class I excitability. The oscillations are born via a saddle-node on an invariant circle. **(B)** The bifurcation curve for g_M after the B.T point, when the neuron is type II (or class II), oscillations are born via a Hopf bifurcation (labelled H.B). Although the limit points still exist, the branch of periodic solutions are emerging from the Hopf point rather than the limit point. Numerical limitations prevented us from demonstrating the connection between the blue lines.

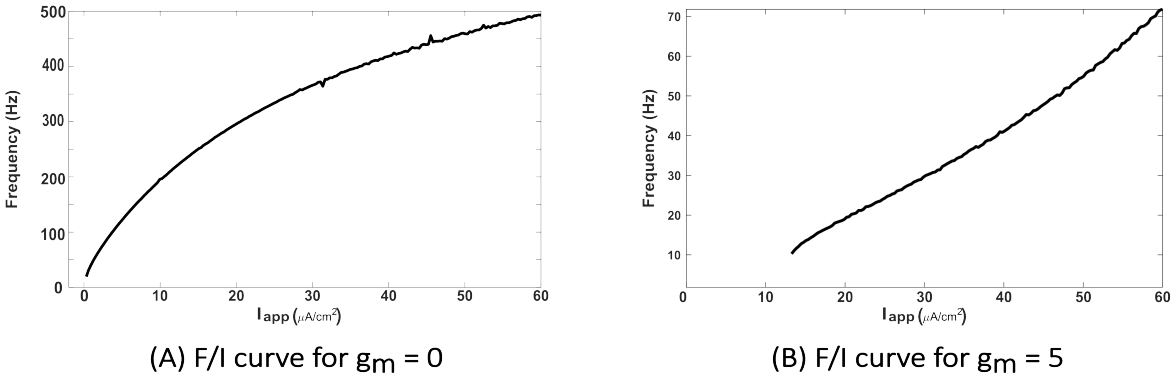


Figure 6.5: Frequency-Current curves for the RTM model neuron at different values of g_M. **(A)** F/I curve at $g_M = 0$. The firing frequency can start at arbitrarily low values for I_{app} near 0 μA . This is a neuron with type I excitability. **(B)** F/I curve at $g_M = 5$. The firing frequency starts a finite value and has a relatively narrow range of values for the same range of applied currents. This is a neuron with type II excitability.

conductances g_M ranging from 0 to 15 mS/cm^2. We verify this in Figure 6.6, which shows simulations of the RTM model with different M-current conductances (g_M) and external current inputs (I_{app}) ranging between 1 and 60 μA. In panel (D), when the M-current conductance is increased to 10 mS/cm^2, applying an external current of 30 μA can no longer trigger the onset of limit cycle oscillations. This is in agreement with our bifurcation analysis. Increasing the input current to 60 μA, the neuron exhibits a stable limit cycle. An external current of 60 μA also gives rise to stable limit cycles for values of the M-current conductance below 10 mS/cm^2.

In order to derive a phase model reduction, the coupling should be sufficiently weak. The coupling strength ε is corresponds to g_{syn} in our model. As seen in Chapters 4 and 5, Theorem 4.2.1 requires that g_{syn} be sufficiently weak, but does not explicitly quantify how small it should be. In [4], this value is chosen to be 0.3. In our work, this is chosen to be 0.2.

A description of all the currents, parameters and their kinetics for the RTM model is summarized in Tables 6.1, 6.4 & 6.3 respectively. The synaptic parameters, g_{syn} and τ_{syn}, the range of g_M values we consider for our analysis and the appropriate I_{app} are summarized in Table 6.5.

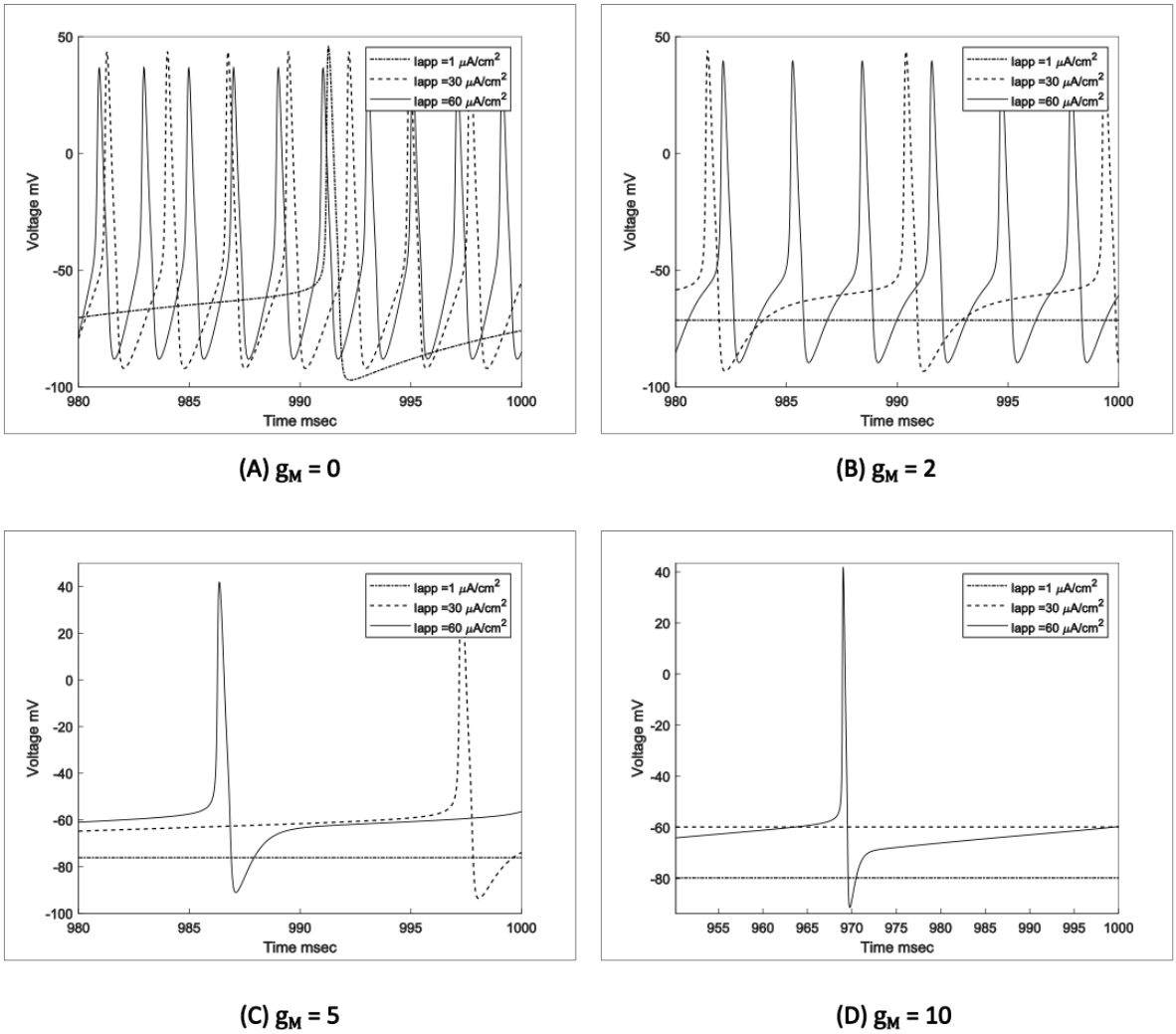


Figure 6.6: Simulations for a single reduced Traub Miles neuron evaluated at different values of the M-current conductance. Each panel displays three time series corresponding to a fixed g_M under the effect of different values of the applied current ($I_{app} = 1, 30, 60\ \mu A$). **(A)**When g_M is set to 0 mS/cm^2, a periodic solution can be obtained by applying $1, 30, 60\ \mu A$ **(B)** When g_M is set to 2 mS/cm^2, a periodic solution can be obtained by applying $30, 60\ \mu A$ **(C)** When g_M is set to 5 mS/cm^2, a periodic solution can be obtained by applying $30, 60\ \mu A$ **(D)** When g_M is set to 10 mS/cm^2, a periodic solution can be obtained by applying $60\ \mu A$.

Current	Current Description	Kinetics
I_{Na}	Transient Na^+ current	$g_{Na}m^3h(V-V_{Na})$
I_K	Delayed Rectifier K^+ current	$g_K n^4(V-V_K)$
I_M	Muscarinic K^+ current	$g_M w(V-V_K)$
$I_{synaptic}$	Synaptic current	$g_{syn}s(V-V_{syn})$
I_L	Leakage Current	$g_L(V-V_L)$

Table 6.1: Description of the ionic currents in Eq. (6.1)

Gating variable X	α_X	β_X
m	$\frac{0.32(54+V)}{1-\exp\left(-\frac{54+V}{4}\right)}$	$\frac{0.28(V+27)}{\exp\left(\frac{V+27}{5}\right)-1}$
n	$\frac{0.032(V+52)}{1-\exp\left(\frac{V+52}{5}\right)}$	$0.5\exp\left(\frac{-(57+V)}{40}\right)$
h	$0.128\exp\left(\frac{-(V+50)}{18}\right)$	$\frac{4}{1+\exp\left(-\frac{V+27}{5}\right)}$
s	$5(1+\tanh\left(\frac{V}{4}\right))$	$\frac{1}{2}$

Table 6.2: Kinetics for the rate functions.

Gating variable X	w_∞	τ_∞
w	$\frac{1}{1+\exp\left(\frac{-(V+35)}{10}\right)}$	$\frac{400}{3.3\exp\left(\frac{V+35}{20}\right)+\exp\left(-\frac{V+35}{20}\right)}$

Table 6.3: Kinetics for the M-current.

Conductivity (mS/cm^2)	Value	Reversal Potential (mV)	Value
g_L	0.1	V_L	-67
g_{Na}	100	V_{Na}	50
g_K	80	V_K	-100
		V_{syn}	0

Table 6.4: Parameters for Eq. (6.18)

Parameter	Value
I_{app}	60 μA
g_M	{0,2,5} mS/cm^2
τ_s	2 ms^{-1}
V_{syn}	0 mV

Table 6.5: Parameter values for phase model analysis

Chapter 7

Results

In Chapter 5, we determined conditions that can guarantee the asymptotic stability of a symmetric cluster associated with a phase difference ψ. In this chapter we will numerically derive the interaction function for the RTM neuron model described in Chapter 6. We then use this to present stability predictions of admissible symmetric clusters for different network sizes equipped with a nearest neighbour and all-to-all type of coupling. Finally, we verify these predictions by performing numerical simulations of the full RTM model.

7.1 Methods

7.1.1 Numerical simulations

All model simulations were carried out using a 2nd-order Runge Kutta algorithm (ODE23) in MATLAB using default numerical parameters [2]. The model parameter values are as described in Chapter 6. The number of time steps for all simulations was set to 1.5×10^4, with two exceptions. First, in the case of a pair of weakly coupled RTM model neurons, the time steps were increased to 3×10^4. Second, when simulating a network of 300 model neurons, the number of time steps was reduced to 8000 due to computational limitations.

We present our simulation results in three ways. For smaller networks, the voltage traces of all the neurons in the network are plotted versus time. For larger networks ($N > 4$), the results are also presented as *raster plots*, which provide information about spike times of the neuron—the times at which a neuron fires an action potential. These are generated by finding the times corresponding to the peak voltages for each neuron

throughout the simulation. We do this on MATLAB using the *findpeaks* function [1] and defining a minimum threshold so that we avoid picking the times when the voltage trace reaches a local minimum. This threshold was defined to be at -10 mV during our simulations. For larger networks, raster plots are useful for identifying neurons that synchronize their spiking, as indicated by nearly identical spike times.

Additionally, we present a visual representation of the clustering that arises in the network. These visualizations consist of a collection of nodes, each representing a model neuron, with lines connecting nodes that are involved in symmetric, reciprocal synaptic coupling. Each node is assigned a specific colour, and nodes sharing the same colour correspond to model neurons that belong to the same cluster in the periodic solution.

Modelling the effect of acetylcholine (ACh)

In our analysis, we assume that the ACh only affects the M-current. The effect of ACh is thus simulated by changing the membrane conductance of the M-current, in particular the maximal conductance value, g_M. As discussed in Chapter 2 and Section 3.3, the M-current is down-regulated in the presence of ACh. In Chapter 6, we identified two values of g_M, at which the corresponding RTM model neuron exhibited qualitatively different dynamics. Specifically, at $g_M = 0$, the RTM model neuron showed Class I dynamics, while at $g_M = 5$, it exhibited Class II dynamics. Accordingly, we set the parameter g_M to 0 to simulate a neuron under the effect of a 'high' concentration of ACh. A neuron under the effect of a 'low' concentration of ACh is simulated by increasing the parameter g_M to 5.

Choice of initial conditions

In order to more easily verify if a particular $n-$cluster solution occurs in the network simulation, especially in the case of multi-stability, we choose initial conditions that are close to that solution. The initial condition for each neuron is chosen as follows:

$$X_i = \left(V_i, h_i, m_i, w_i, n_i, s_i\right) = \left(V_i, 0, 0, 0, 0, 0\right), \tag{7.1}$$

where V_i is chosen from an interval (I) centered around the resting potential $-70mV$ in this case we consider $I = [-80mV, -60mV]$. Since we are seeking an $n-$cluster, we divide I uniformly into n sub-intervals.

$$I = \cup_{j=1}^{n} I_j = \cup_{j=1}^{n} [-80 - a \cdot (j-1), -80 - a \cdot (j)), \tag{7.2}$$

where $a = \frac{-80+60}{n}$. Each neuron belonging to the same cluster is given an initial voltage chosen from one of the intervals in I. To ensure we are not picking each neuron in the cluster to start exactly with the same voltage but with small enough differences, we make use of the *rand* function in MATLAB.

Measuring phase difference

In order to more easily verify whether the simulations match the predictions of the phase model analysis, we define a measure of the phase difference between neurons. This is defined using the spike times corresponding to each neuron, recorded during the simulation. We store these times in order to make raster plots, but we can use them to find the phase difference. We measure the phase $\phi_i(t)$ of a neuron X_i at a timestep t is as follows

$$\phi_i(t) = \frac{t - t_{i,lap}}{t_{i,nap} - t_{i,lap}} \cdot 2\pi \tag{7.3}$$

In (7.3), $t_{i,lap}$ and $t_{i,nap}$ refer to the last and next action potential respectively which we take from the spike times [25]. The phase difference $\psi_i(t)$ is defined as

$$\psi_i(t) = \phi_{i+1}(t) - \phi_i(t) \qquad i \mod N \tag{7.4}$$

In our simulations, $\psi_i(t_{final-1})$ is recorded as the steady state phase difference for the corresponding cluster solution.

Equivalently, we may infer the phase differences from the firing order of the clusters displayed on the raster plots. This relationship is described in Appendix C.1. For larger networks, we opted for the latter method to verify the phase differences.

7.1.2 Phase model calculation

In Chapter 6, we proposed a value for the externally applied current such that the corresponding RTM neuron model (6.5) exhibits stable limit cycles. For a high dimensional conductance-based model like the RTM model, it is impossible to analytically derive an interaction function H (see (4.36)). As a result, we resort to a numerical derivation of the function. Using XPPAUT [30], we can numerically solve for the adjoint system, (4.29), of a neuron exhibiting limit cycles and consequently their interaction function, (4.15). The interaction function H can then be approximated by a truncated Fourier series that is

readily available to us from XPPAUT:

$$H(\phi) \approx a + a_1 \cos\phi + b_1 \sin\phi + a_2 \cos 2\phi + b_2 \sin 2\phi + \sum_{i=3}^{N} (a_n \cos n\phi + b_n \sin n\phi) \quad (7.5)$$

The interaction function H was calculated in this manner for four distinct values of the maximal M-current conductance, g_M, each corresponding to a different strength of the M-current:

$$g_M = \{0, 2, 3.13, 5\} \quad (7.6)$$

The values in (7.6) were chosen based on the results for the RTM model obtained in [4] and in Chapter 6, where we identified $g_M = 0$ and $g_M = 5$ as two different strength of the M-current, at which the the corresponding neuron model exhibited qualitatively different dynamics. In particular, [4] showed that the in-phase and anti-phase solutions were stable for a pair of RTM model neurons at $g_M = 5$ and 0 respectively, but were both unstable for the intermediate values of g_M near 2. During our analysis, we identified two intermediate values, $g_M = 2$ and $g_M = 3.13$, as potential points near which the anti-phase and in-phase solutions respectively switch in their stability.

The numerical approximation of the interaction function corresponding to the four different values of g_M in (7.6), is summarized in Appendix C.2, where a 30-term approximation was chosen to minimize the computational burden while maintaining accuracy in the evaluation of the function, H.

Using the numerical approximation of the interaction function, H_{g_M}, corresponding to a fixed level of the M-current strength (determined by g_M), we compute the appropriate μ_j, (5.22), to perform the stability analysis as described in Chapter 5.

7.2 A pair of reduced Traub-Miles model neurons

In this section, we review the phase model analysis for our model of a pair of synaptically coupled pyramidal neurons located within the CA3 sub-hippocampal region. In Chapter 6, we presented the Reduced Traub-Miles model (RTM) of an excitatory pyramidal neuron with an additional potassium current known as the M-Current (I_M). For a pair of RTM model neurons coupled with an excitatory synapse, the corresponding model is given by setting $N = 2$ in Eq. (6.18):

$$\begin{aligned}
\frac{dV_1}{dt} &= I_{app} - g_L(V_1 - V_L) - g_M(V_1 - V_K) - g_{Na}m^3h(V_1 - V_{Na}) \\
&\quad - g_K n^4(V_1 - V_K) - g_{syn}s_2(V_1 - V_{syn}) \\
\\
\frac{dV_2}{dt} &= I_{app} - g_L(V_2 - V_L) - g_M(V_2 - V_K) - g_{Na}m^3h(V_2 - V_{Na}) - \\
&\quad g_K n^4(V_2 - V_K) - g_{syn}s_1(V_2 - V_{syn}) \qquad (7.7) \\
\\
\frac{ds_i}{dt} &= 5\left(1 + \tanh\left(\frac{V_i}{4}\right)\right)(1 - s_i) - \frac{s_i}{\tau_s} \qquad i = 1, 2
\end{aligned}$$

7.2.1 Phase difference model

We study the system (7.7) in detail by considering the corresponding phase-difference model (See Chapter 4):

$$\frac{d\psi}{dt} = -\varepsilon(H(\psi) - H(-\psi)) = -2\varepsilon(H_{odd}(\psi)), \qquad (7.8)$$

where the interaction function H has been calculated as described in Section 7.1.2. If we directly substitute the truncated Fourier series approximation of H in Eq. (7.8), all of the cosine terms cancel out leaving only the sine terms. In Eq. (7.8), ψ is the phase difference between the two model neurons defined as $\theta_2 - \theta_1$ where θ_i describes the phase of the model neuron (See definition in Chapter 4). Since Eq. (7.8) is one dimensional system, it can be analyzed graphically as we show below. H_{odd} is $2\pi-$periodic, so we only consider $\psi \in [0, 2\pi)$.

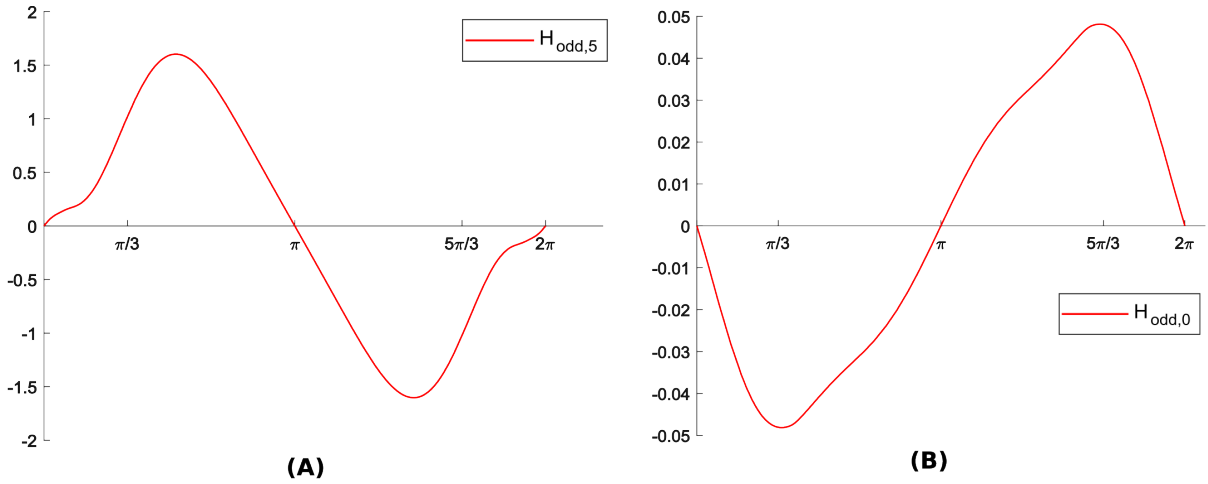


Figure 7.1: H_{odd}, in Eq. (7.8), is plotted for **(A)** $g_M = 5$ and **(B)** $g_M = 0$. In both cases, $\psi = 0$ and $\psi = \pi$ are the only fixed points for a pair of weakly coupled RTM model neurons. The stability analysis is discussed in the main text

Existence of equilibrium solutions

An equilibrium solution for Eq. (7.8) corresponds to ψ^* such that $\dot{\psi}|_{\psi=\psi^*} = 0$. For the equivalent neuron model, this describes a periodic solution where the two neurons will repetitively spike with a fixed phase difference of ψ^*. Through the phase model analysis at different values of g_M, we identified $g_M = 3.13$ as a possible transition point where the sign of the interaction function, H, evaluated at 0 changes. H_{odd} is plotted separately for $g_M = \{2, 3.13\}$ in Figure 7.2, and for $g_M = \{0, 5\}$ in Figure 7.1, to determine the equilibrium solutions of Eq.(7.8), or equivalently, the zeros of H_{odd}.

When g_M is set 0 or 5, $\psi = 0$ and $\psi = \pi$ are the only fixed points, as illustrated respectively in panels (B) and (A) in Figure 7.1. For the values $g_M = 2$ and $g_M = 3.13$, in addition to the fixed points at 0 and π, we observe fixed points within the interval $(0, \pi)$ and, by symmetry, within $(\pi, 2\pi)$ as well. These points are labelled 'a', 'b', 'c' and 'd', 'e', 'f', respectively, in panel (A) of Figure 7.2. Note that the pair of points (a,f), (b,e) and (c,d), all share the following relationship due to the anti-symmetry and periodicity of H_{odd}:

$$y = 2\pi - x, \tag{7.9}$$

where $(x, y) = \{(\text{a,f}), (\text{b,e}), (\text{c,d})\}$.

Analyzing the subplots in panels (B) and (C), the fixed point, 'a', lies within an interval $\left(\frac{\pi}{13}, \frac{\pi}{12}\right)$. Similarly points 'c' and 'b' lie within intervals $\left(43\frac{\pi}{52}, 10\frac{\pi}{12}\right)$ and $\left(13\frac{\pi}{24}, 9\frac{\pi}{16}\right)$

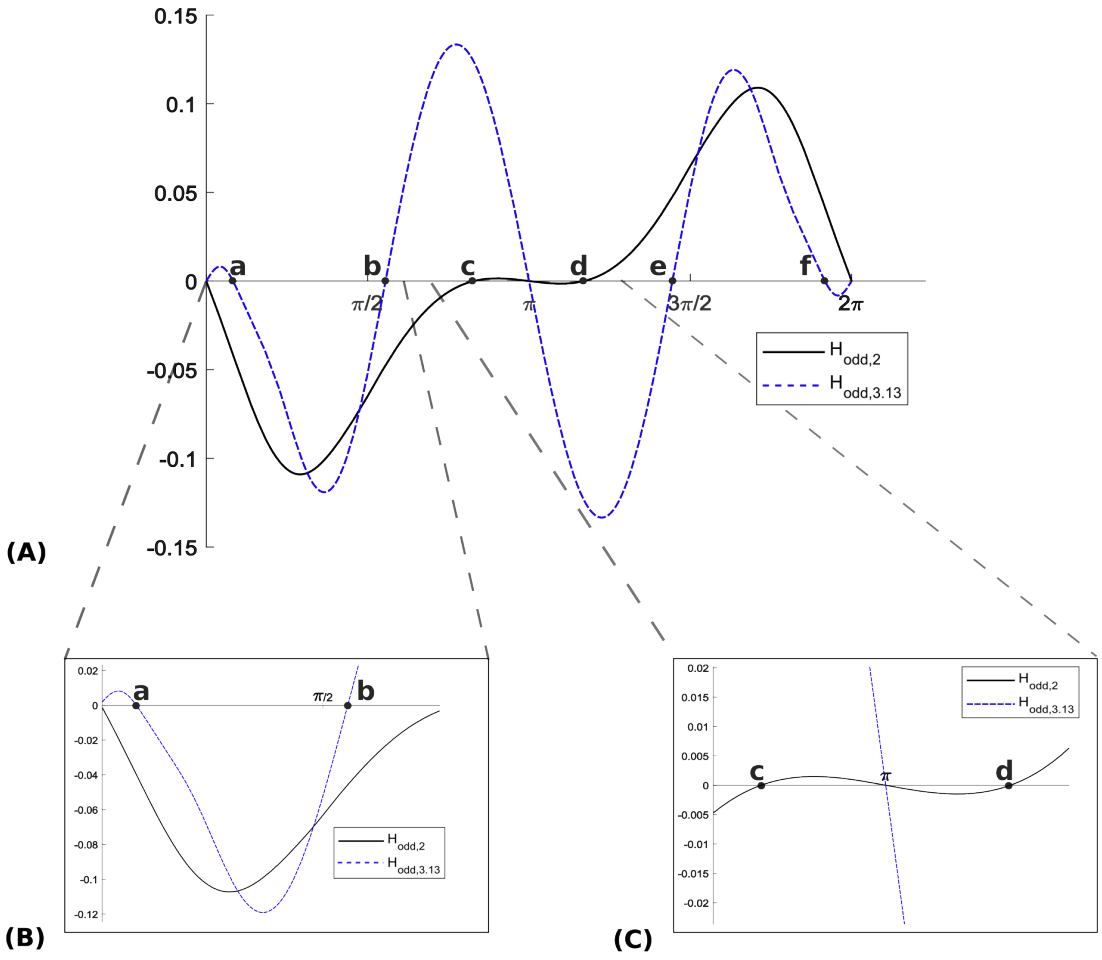
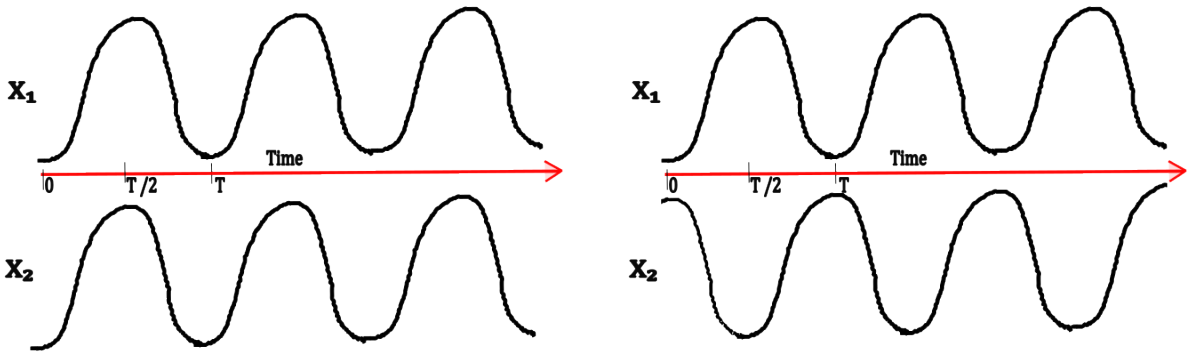


Figure 7.2: **(A)** H_{odd}, in Eq. (7.8), is plotted for $g_M = 2$ and 3.13. The subplots show behaviour near 0 and π. In both cases, 0 and π are fixed points to the system. **(B)** When g_M is set to 3.13, the system also exhibits additional fixed points labelled 'a' (and 'f') and 'b' (and 'e') near 0 (near 2π) and $\frac{\pi}{2}$ (near $3\frac{\pi}{2}$) respectively. **(C)** When g_M is set to 2, the system also exhibits additional fixed points labelled 'c' and 'd' near π.

respectively. The intervals associated with the points 'd', 'e' and 'f' can be determined using the relation in Eq.(7.9).

Recall when two neurons oscillate with a phase difference $\psi = 0$, they are defined as an *in-phase* or a *fully synchronized state*, as illustrated in Figure 7.3a. They spike in unison. When two neurons oscillate with a phase difference $\psi = \psi^* = \pi$, their spikes are out of phase by half a period as illustrated in Figure 7.3b, where we see neuron X_2 spikes at $t = 0$ and neuron X_2 spikes at $t = \frac{T}{2}$. In both cases, the timings between the spikes are symmetric, i.e., the duration of time starting from the spike time of X_1 to the that of X_2 is the same as the time duration from when neuron X_2 spikes to when neuron X_1 spikes.

In the phase difference model, if ψ is the phase difference from neuron X_2 to neuron X_1, then $2\pi - \psi$ is the phase difference from neuron X_1 to neuron X_2, denoted by ψ_1 and ψ_2 respectively. Symmetry in the spike timing is equivalent to having identical phase differences ψ_i for $i = \{1, 2\}$. We can see how for a pair of model neurons there is symmetry for $\psi^* = \pi$, but for $\psi^* \neq \{0, \pi\}$, the symmetry is broken. For ψ^* associated with the points labelled 'a','b' and 'c' in Figure 7.2, the timing between the spikes are non-symmetric, since $\psi^* \neq 2\pi - \psi^*$ thus implying that $\psi_1 \neq \psi_2$. These solutions are more generally referred to as 'out-of-phase' solutions.



(a) Voltage traces for neurons in-phase, $\psi^* = 0$. Both X_1 and X_2 spike at the same times ($t = \frac{T}{2}$).

(b) Voltage traces for neurons in anti-phase, $\psi^* = \pi$. X_2 spikes at $t = 0$, whereas X_1 spikes at $t = \frac{T}{2}$.

Figure 7.3: Schematic of voltage traces corresponding to an in-phase and anti-phase solution for a pair neurons

Stability Analysis of equilibrium solutions

To determine the stability of an equilibrium solution ψ^*, we determine whether the derivative of the function H_{odd} is positive or negative at ψ^*. Due to the negative sign in Eq. (7.8), the equilibrium solution ψ^* is locally asymptotically stable, if $H'_{odd}(\psi^*)$ is positive and unstable if it is negative.

7.2.2 Phase model predictions

In Figure 7.1, we see a dramatic switch in the behaviour near 0 and π as we move from $g_M = 0$ to $g_M = 5$ as illustrated in panels (B) and (A) respectively. Particularly, the stabilities of the in-phase and anti-phase solutions switch with the in-phase being stable for $g_M = 5$ and the anti-phase state being stable for $g_M = 0$. In Figure 7.2, we see that the in-phase solution remains unstable until $g_M = 3.13$, whereas the stability of the anti-phase state loses stability near $g_M = 2$ as illustrated in panels (B) and (C) respectively. The case of $g_M = 2$ is interesting since both the in-phase and anti-phase states are unstable and the additional fixed points, 'c' and 'd', identified in Figure 7.2, panel (C), are stable. The stability analysis for the in-phase and anti-phase states corresponding to the system in Eq. (7.7) is summarized in Table 7.1.

Value of g_M	Phase Difference ψ	Stability Analysis
0	0	Unstable
	π	Stable
2	0	Unstable
	π	Unstable
3.13	0	Stable
	π	Unstable
5	0	Stable
	π	Unstable

Table 7.1: Phase model predictions for a pair of RTM model neurons at different values of g_M $(= \{0, 2, 5\})$.

We also note that for $g_M = 3.13$, the basin of attraction corresponding to the in-phase solution is relatively small. Instead, the stable fixed point ('b') identified in Figure 7.2, panel (B), has a larger basin of attraction, and may dominate during the simulations.

7.2.3 Numerical studies

We now verify the phase model predictions from Table 7.1 by carrying out numerical simulations for the pair of RTM neurons with the coupling strength $g_{syn}(= \varepsilon)$ set to 0.2 mS/cm^2. The voltage traces for the coupled model neurons at the different levels of M-current are presented in Figure 7.4.

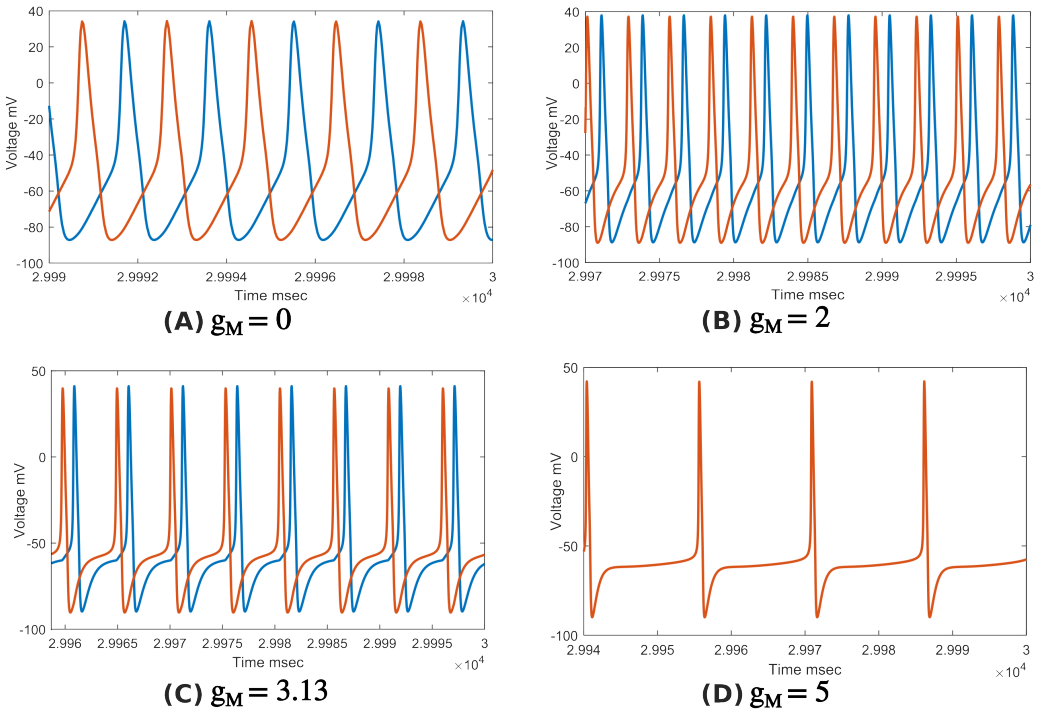


Figure 7.4: Numerical simulations for a pair of RTM neurons at different strengths of the M-Current, with g_{syn} set to 0.2. **(A)** The cells oscillate in anti-phase when g_M set to 0. **(B)** g_M is set to 2 and the cells oscillate in an out-of-phase solution,associated with a phase difference that is close to the equilibrium point 'c', identified in panel (C) of Figure 7.2. **(C)** g_M is set to 3.13 and the cells oscillate in an out-of-phase solution, associated with a phase difference close to the equilibrium solution 'b', identified in panel (B) of Figure 7.2. **(D)** The cells synchronize when g_M is set to 5.

For $g_M = 5$, illustrated in panel (D), as predicted the neurons synchronize indicating the stability of the in-phase solution. When g_M is set 0 or 2, we see that the neurons

desynchronize. In particular, in the absence of M-current ($g_M = 0$), the neurons tend to oscillate in anti-phase as illustrated in panel (A). When M-current is provided at a 'low' level by increasing g_M to 2, the neurons exhibit a different phase-locked state, illustrated in panel (B), which was associated with a phase difference (calculated using Eq. (7.3)) closer in value to the additional stable equilibrium solution,'c', identified in $(\frac{\pi}{2}, \pi)$ in Figure 7.2, panel (C).

At $g_M = 3.13$, we were unable to obtain the expected in-phase solutions. Although, other phase-locked solutions are observed which was associated with a phase difference (calculated using Eq. (7.3)) closer in value to the additional stable equilibrium, 'b', identified in Figure 7.2, panel (B).

The simulations agreed with the phase model predictions for a pair of weakly coupled RTM model neurons, with g_{syn} set to 0.2, and supplied with an M-current at strengths corresponding to $g_M = 0, 2$ and 5. When the M-current strength is set at the specific strength corresponding to $g_M = 3.13$, the predictions did not seem to agree, in particular regarding the stability of the in-phase solution. This point ($g_M = 3.13$) was identified as the point where the sign of the derivative H' evaluated at 0, becomes positive thereby indicating the stability of the in-phase solution. However our simulations did not verify the in-phase stability pointing to a possible discrepancy in the approximation of H for this specific value. It may be possible that more terms may be required in the approximation of the interaction function corresponding to values of g_M that are very close to a critical point. Additionally, it may be that $g_M = 3.13$ is extremely close to a bifurcation (where the stability of the in-phase changes), and as such the phase model may be an unreliable tool in determining existence and stability of solutions for a system corresponding to a set of parameters chosen within a small neighbourhood of a transition point. Alternatively, it could also be that for this strength of the M-current, a coupling strength of 0.2 might be too strong. Without further investigation, we do not to consider $g_M = 3.13$, in our analysis moving forward and focus on the predictions and corresponding results for the values of $g_M = \{0, 2, 5\}$.

Based on the results for a pair of weakly coupled RTM model neurons, we propose three qualitative levels of ACh, whose descriptions are summarized in Table 7.2. In Table 7.2, g_M^* is the point associated with a Bogdanov Takens bifurcation, beyond which the neuronal dynamics switches to Class II and the anti-phase solution loses stability. $\hat{g}_M$ is the point where the neurons begin to synchronize. Our phase model approximation predicts this point to occur at $\hat{g}_M = 3.13$, which disagreed with numerical simulations. However, in general, we expect the framework outlined in Table 7.2 to remain consistent across different neuron models incorporated with an M-current. In the context of our model and for our analysis, $g_M = 0, 2$ and 5 are identified with low, intermediate and high

Level of ACh	M-current conductivity	Description
High	$g_M > g_M^*$	The anti-phase solution is stable and neuron has Class I dynamics
Intermediate	$g_M^* > g_M > \hat{g}_M$	Both in-phase and antiphase solutions are unstable. Neuron has Class II dynamics
Low	$g_M < \hat{g}_M$	The in-phase solution is stable and the neuron has Class II dynamics.

Table 7.2: Neuronal behaviour at different Levels of ACh

levels of ACh respectively. These observations and results are consistent with numerical findings demonstrated for the same model in [4].

7.3 A network of arbitrary size with all-to-all global homogeneous coupling

We now consider a network of reduced Traub Miles (RTM) model neurons equipped with weak all-to-all coupling, such that each cell receives a synaptic input from every other cell within the population at the same intensity.

$$\frac{dV_i}{dt} = I_{app} - I_{ionic}(V) - \frac{g_{syn}}{N}\sum_{j=1}^{N} s_j(V_i - V_{syn}) \tag{7.10}$$
$$\frac{ds_i}{dt} = 5\left(1 + \tanh\left(\frac{V_i}{4}\right)\right)(1 - s_i) - \frac{s_i}{2} \qquad i = \{1, 2, .., N\}$$

The coupling strength ε associated with Eq. (7.10), is defined by the maximal synaptic conductance, g_{syn}, normalized by N to reflect the individual contributions from the other cells. The condition guaranteeing the stability for a symmetric cluster solution for a network of this form is reviewed in Chapter 5 (see Section 5.2.2). A significant implication of this condition is that the stability for a symmetric $n-$cluster solution, where the phase differences are equal ($\psi_i = \psi$), is independent of size of the network N and is implicitly dependent on ψ (See Eqs. (5.26) and (5.27)). Essentially for a network with global homogeneous coupling, any symmetric division of the network into n clusters is an admissible $n-$cluster solution with stability described by Eq. (5.27). As a result, the phase model predictions are also applicable for symmetric $n-$cluster solutions, where the adjacent phase differences ψ are not necessarily equal. An all-to-all coupling architecture is adopted as a way to study the high connectivity within the CA3 recurrent network under different strengths of the $M-$currents.

7.3.1 Phase model predictions

We use the phase model approximation of Eq. (7.10) to predict the stability of symmetric $n-$cluster solutions for the network. Table 7.3 summarizes which symmetric $n-$ clusters are stable for a network given by Eq. (7.10).

If N is divisible by n, then a corresponding network of size N, admits a symmetric $n-$cluster solution. The columns $2-4$ in Table 7.3 correspond to the network at a particular strength of the M-current (indicated by g_M) and each row summarizes the stability trend for a specific $n-$ cluster. For a given value of n, we compute Eq.(5.27) for each g_M, and if

Table 7.3: Phase model predictions for $n-$ clusters ($n = \{1, .., 15\}$) across different values of g_M in a network with *global homogeneous coupling*. The solutions that were verified numerically are marked with a *.

Cluster Size	Value of g_M		
n	0	2	5
15	Unstable	Unstable	Unstable
14	Unstable	Unstable	Unstable
13	Unstable	Unstable	Unstable
12	Unstable	Unstable	Unstable
11	Unstable	Unstable	Unstable
10	Unstable	Unstable	Unstable
9	Unstable	Unstable	Unstable
8	Unstable	Unstable	Unstable
7	Stable*	Stable*	Unstable
6	Stable*	Stable*	Unstable
5	Stable*	Stable*	Unstable
4	Stable*	Stable*	Unstable
3	Unstable	Unstable	Unstable
2	Unstable	Unstable*	Unstable*
1	Unstable*	Unstable*	Stable*

it is positive, we mark the corresponding $n-$cluster as a predicted stable solution for some appropriate network at particular strength of the M-current.

The phase model predicts that the in-phase solution ($n = 1, \psi = 0$) follows the same stability trend as a pair of weakly coupled RTM model neurons, which is in line with the fact that the stability condition for the in-phase solution only depends on the sign of $H'(0)$. We expect this stability trend to be consistent across all networks and coupling architectures satisfying periodic boundary conditions. The in-phase solution is also the only symmetric solution predicted to be stable when the M-current conductance is increased to $g_M = 5$. When g_M is set to 0 or 2, the phase model predicts that there are multiple stable $n-$cluster solutions ranging from 4 to 7 clusters.

7.3.2 Numerical studies

We studied networks for $N = 4 - 15$ and 24 , equipped with an all-to-all coupling such that each weight w_i in Eq. 5.21 is set to 1. In Table 7.3, a stable $n-$cluster solution is marked by *, if we observed a symmetric $n-$cluster for at least one N and corresponding ψ through our simulations.

When g_M is set to 0 or 2, we found multiple $n-$cluster solutions that were predicted to be stable for each network size. The $4-, 5-$ and $6-$clusters were obtained for networks of $10, 12, 15$ and 24 RTM model neurons, with g_M set to 0 and are presented in Figure 7.5. In Figure 7.5, panels (A)-(C) display the voltage traces corresponding to $4-, 6-$ and $5-$ cluster solutions respectively. The remaining panels, (D)-(I), below each voltage trace illustrate how a network organizes itself into the n clusters. As an example, consider the panel (D), which shows a network of 24 RTM model neurons equipped with all-to-all connections exhibiting a stable $4-$cluster solution. Each node in the ring schematic corresponds to a neuron[1]. Nodes with the same colour represent neurons that belong to the same cluster at the steady state. Each colour also corresponds to one of the traces in the voltage trace plot (panel (A)) identified through the same colour. The raster plots also portray the same information, but with a time component. We can determine the sequence in which each of the 4 clusters spike in one cycle. In this case, the 4 clusters for a network of 24 neurons are given by:

$$
\begin{aligned}
C_1 &= \{1, 5, 9, .., 21\} \\
C_2 &= \{2, 6, 10, .., 22\} \\
C_3 &= \{3, 7, 11, .., 23\} \\
C_4 &= \{4, 8, 12, .., 24\}
\end{aligned}
$$

In panel (D), the raster plot indicates that the firing order is $C_1 - C_2 - C_3 - C_4$ with $\psi = \frac{\pi}{2}$. The same solution $\left(\psi = \frac{\pi}{2}\right)$ is also observed in panel (G), for a network of size $N = 12$. For $\psi = \frac{3\pi}{2}$, the firing order would be reversed $C_4 - C_3 - C_2 - C_1$. Now consider the $6-$cluster

[1]IMPORTANT: The figure does not represent a physical network. The illustration simply shows what neurons are connected and that it has periodic boundary conditions.

solutions obtained for $N = 24$ illustrated in panel (E). The clusters are given by:

$$
\begin{aligned}
C_1 &= \{1, 7, 13, .., 19\} \\
C_2 &= \{2, 8, 14, .., 20\} \\
C_3 &= \{3, 9, 15, .., 21\} \\
C_4 &= \{4, 10, 16, .., 22\} \\
C_5 &= \{5, 11, 17, .., 23\} \\
C_6 &= \{6, 12, 18, .., 24\}
\end{aligned}
$$

with an ordering of $C_1 - C_2 - C_3 - C_4 - C_5 - C_6$ corresponding to $\psi = \frac{\pi}{3}$. The same solution $\left(\psi = \frac{\pi}{3}\right)$ is also observed for a 12 neuron network illustrated in panel (H). We were unable to find the other $4-$ and $6-$ cluster solutions numerically.

An example of an $n-$cluster with different ordering is illustrated in panels (F) and (I) for a network of 15 and 10 RTM model neurons respectively. Following the same scheme as before, the clusters are given by: $C_i = \{i, i + 5, .., N - n - i\}$ for $i = \{1, 2, 3, 4, 5\}$. In panel (F), the clusters fire in the order of $C_5 - C_4 - C_3 - C_2 - C_1$ corresponding to a phase difference of $\psi = \frac{2\pi}{5}$. The ordering is reversed in the case in (I), with an ordering of $C_1 - C_2 - C_3 - C_4 - C_5$ corresponding to $\psi = \frac{8\pi}{5}$. The colours are assigned in order to match the order of the voltage traces presented in panel (C). Note that the $5-$cluster solution can also take on other orderings as well, such as those associated with $\psi = \frac{4\pi}{5}(C_1 - C_4 - C_2 - C_4 - C_3)$ and $\psi = \frac{6\pi}{5}(C_1 - C_3 - C_5 - C_2 - C_4)$ which we did not find numerically.

Increasing the g_M to 5, the system strongly tends to a synchronized solution, with all[2] other states verified to be unstable (by initializing the system close to the cluster solution as discussed in Section 7.1). The synchronization of the network is demonstrated in Figure 7.6.

Next, we considered a network with no M-current ($g_M = 0$), initialized in a stable cluster solution, and introduced transient perturbations during the time interval $[8000, 8050]$. The transient perturbations were in the form of an increased external current pulse applied to a subset of the cells. The perturbations could switch the network between different realizations of the same $n-$clusters. This could either be a change to the firing order, or a change in the cells that belong to the initial clusters. We present a few of these transitions that were observed for the networks $N = 12, 15$ and 24.

[2]In this case we confirmed that an $n-$cluster corresponding to one ψ is unstable, we did not check it for all values of ψ

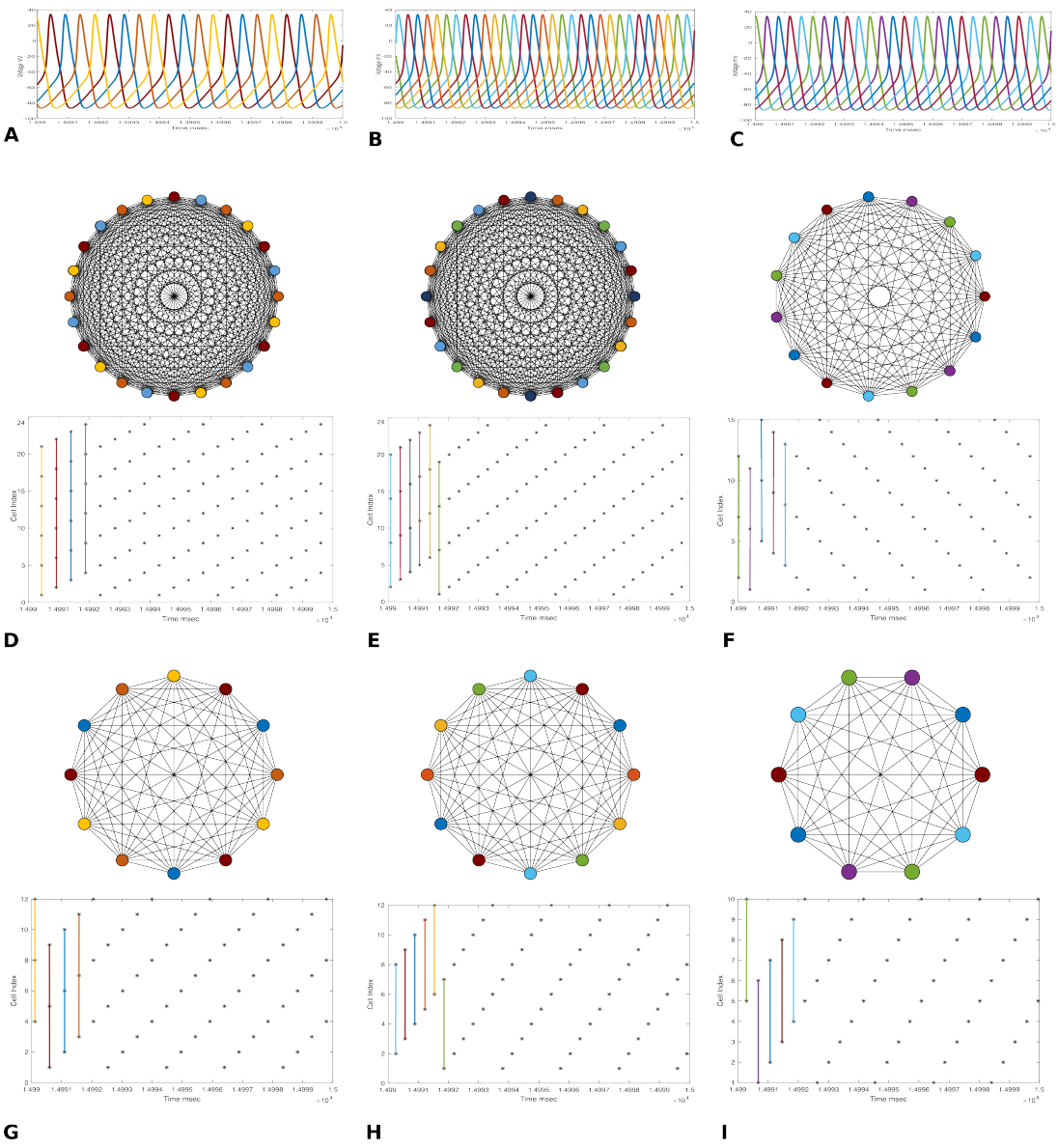


Figure 7.5: Multiple stable cluster solutions obtained for a network of reduced Traub-Miles model neurons of sizes $N = 10, 12, 15$ and 24. In the network, cells are coupled to every other cell with equal synaptic weights ($k = \lfloor \frac{N}{2} \rfloor$,$p = 1$). In each illustration, nodes sharing the same colour represent neurons belonging to the same cluster. The voltage traces are presented for a **(A)** 4−cluster, **(B)** 6−cluster and **(C)** 5−cluster solutions. A stable 4−cluster solution is illustrated for a network of **(D)** 24 cells and **(G)** 12 cells, both associated with $\psi = \frac{\pi}{2}$. A stable 6− cluster is illustrated in a network of **(E)** 24 cells and **(H)** 12 cells, both associated with $\psi = \frac{\pi}{3}$. **(F)** A stable 5−cluster solution is illustrated for a network of 15 cells associated with $\psi = \frac{2\pi}{5}$. **(I)**A different stable 5−cluster is illustrated for a network of 10 cells with $\psi = \frac{8\pi}{5}$. The order of cluster firing is discussed in the main text.

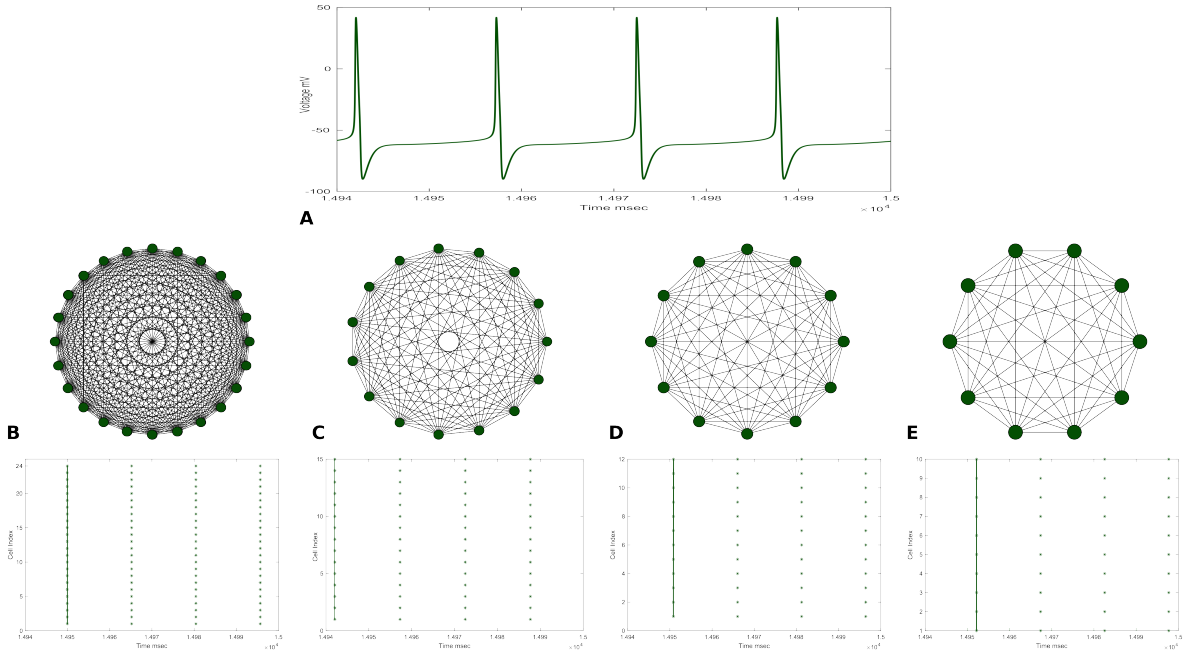


Figure 7.6: Synchronization of a network of RTM model neurons, when g_M is set to 5. **(A)** The voltage trace associated with an in-phase solution. The in-phase solution is illustrated for a network of **(B)** 24 cells, **(C)** 15 cells, **(D)** 12 cells and **(E)** 10 cells through raster plots and node diagrams.

In Figure 7.7, panel (A) shows a network of 24 RTM model neurons, initialized in a stable $4-$cluster associated with $\psi = \frac{\pi}{2}$ and a firing order given by $C_1 - C_2 - C_3 - C_4$. Applying a transient pulse to a subset of the cells can switch the network to a new stable $4-$cluster solution, either with a different ordering given by: $C_1 - C_4 - C_2 - C_3$, as shown in panel (B), or a different arrangement of cluster cells as shown in panel (C). In panel (A), the solution is initialized with clusters, C_2 and C_4, given by: $\{2, 6, 10, 14, 18, 22\}$ and $\{4, 8, 12, 16, 20, 24\}$ respectively. In panel (C), clusters C_2 and C_4 recruit different cells in the new stable solution given by: $\{2, 10, 12, 14, 22, 24\}$ and $\{4, 6, 8, 16, 18, 20\}$ respectively.

Now consider a network initialized in a stable $6-$cluster solution with firing order given by: $C_1 - C_2 - C_3 - C_4 - C_5 - C_6$ which is displayed in panel (D) of Figure 7.7. A transient perturbation, applied to a subset of the cells, can switch the initial state to a new stable cluster solution in three ways as demonstrated through panels (E)-(G). Panel (E) is a stable $6-$cluster solution with a different firing order given by: $C_1 - C_2 - C_6 - C_3 - C_4 - C_5$. Panel (F) shows a stable $6-$cluster solution where the clusters formed in the initial state (panel

(D)) change. In panel (F), the cluster C_6 changes from $\{6, 12, 18, 24\}$ to $\{6, 12, 16, 17\}$, the cluster C_2 changes from $\{2, 8, 14, 20\}$ to $\{2, 14, 19, 24\}$, and the cluster C_4 changes from $\{4, 10, 16, 22\}$ to $\{4, 8, 10, 22\}$. Panel (G) shows a stable 6−cluster solution where there is a change to both the firing order and the arrangement of cells in the clusters. In panel (G), the clusters C_4, C_2 and C_6 change to $\{4, 6, 16, 18\}$, $\{2, 12, 14, 24\}$ and $\{8, 10, 20, 22\}$ respectively. The firing order is given by: $C_1 - C_2 - C_3 - C_6 - C_5 - C_4$. A description of the results associated with $N = 12$ and 15 are discussed in Appendix C.3.

The simulations were repeated with g_M set to 5, where we observed that the synchronized solution persisted under the same transient current pulses used in the $g_M = 0$ case.

7.3.3 Prediction failure in the anti-phase and 3− cluster solutions

During our simulations, we observed that the 2−cluster ($\psi = \pi$) and 3−cluster solutions were actually stable when g_M is set to 0, contradicting the predictions of the phase model (See Table 7.3). In particular, we observed the 2−clusters ($\psi = \pi$) consistently for a network of 4 neurons (See Figure 7.8) and 3−clusters for a network of $6, 12, 15$ and 24 neurons as well (See Figure 7.9).

Further investigation revealed that using a minimum of a 100 Fourier terms in the approximation of the interaction function, H, could numerically classify the anti-phase solution as a stable solution for $g_M = 0$. For the 3−cluster solution, using a minimum of 105 terms, classifies it as a stable solution. This suggested that in the higher connectivity schemes, where more connections are involved, the higher order terms in our approximations are significant. We compared the eigenvalues for the anti-phase and 3−cluster solutions computed for a different approximations of H in Tables 7.4 and 7.5 respectively. We see that μ_1 in both cases remained consistent across the different approximations. How-

	Number of terms	
μ_j	30	100
μ_0	−0.0093	0.0013
μ_1	0.0392	0.0392

Table 7.4: μ_j for $n = 2$

	Number of terms		
μ_j	30	100	105
μ_0	−0.0111	−0.0006	0.0001
μ_1	0.0267	0.0265	0.0267

Table 7.5: μ_j for $n = 3$

ever, μ_0 changes dramatically across the different approximations of H. The parameter μ_0

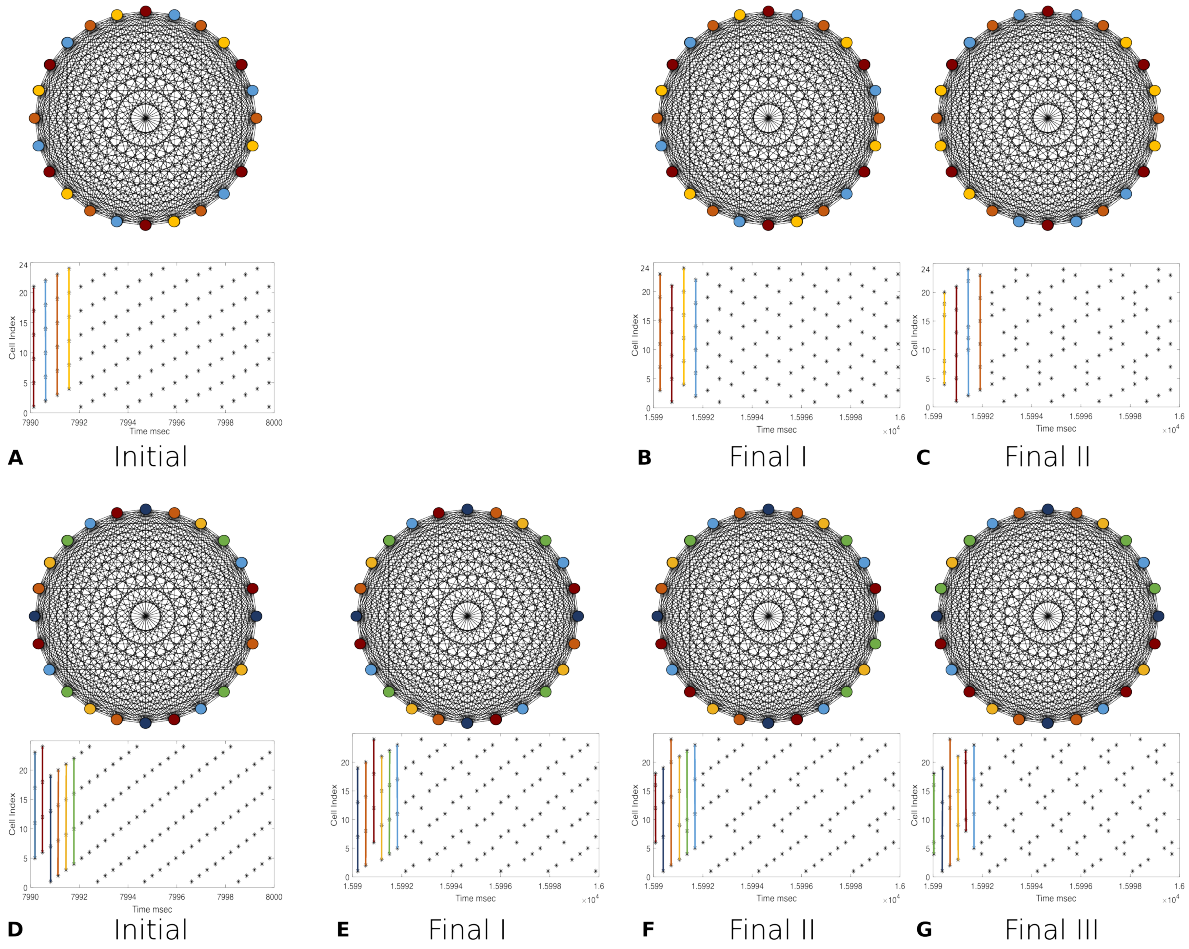


Figure 7.7: Multistability when g_M is set to 0, in a network of 24 RTM model neurons with globally homogeneous coupling. **(A)** The network is initialized in a stable 4−cluster with a firing order: $C_1 - C_2 - C_3 - C_4$, where $C_i = \{i, i+4, \ldots, 19+i\}$. **(B)** A transient perturbation, in the form a current pulse, applied to a subset of the cells alters the firing order to $C_1 - C_4 - C_2 - C_3$. **(C)** Applying the pulse to a different subset of cell, can switch the network to a stable 4−cluster solution where the cells belonging to C_2 and C_4 change to $\{2, 10, 12, 14, 22, 24\}$ and $\{4, 6, 8, 16, 18, 20\}$ resp. **(D)** The network is initialized in a stable 6−cluster with a firing order: $C_1 - C_2 - C_3 - C_4 - C_5 - C_6$, where $C_i = \{i, i+6, \ldots, 17+i\}$. **(E)** A transient perturbation, in the form a current pulse, applied to subset of the cells alters the firing order to $C_1 - C_2 - C_6 - C_3 - C_4 - C_5$. **(F)** Applying a perturbation to a different subset of cells can also switch the network to a stable 6−cluster solution where the cells belonging to cluster C_6, C_2 and C_4 change to $\{6, 11, 16, 18\}$,$\{2, 13, 20, 24\}$ and $\{4, 8, 10, 22\}$. **(G)** The perturbation can also switch the network to a stable 6−cluster solution where the cells belonging to cluster C_6, C_2 and C_4 change to $\{8, 10, 20, 22\}$,$\{2, 12, 14, 24\}$ and $\{4, 6, 16, 18\}$ and the firing order changes to $C_1 - C_2 - C_3 - C_6 - C_5 - C_4$.

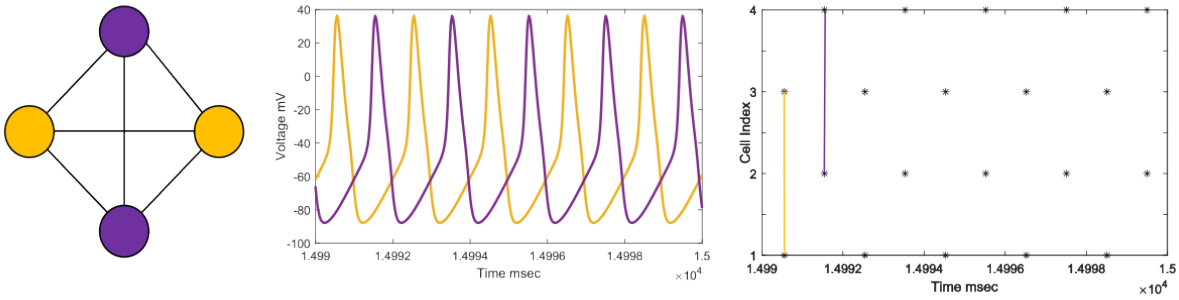


Figure 7.8: Anti-phase ($\psi = \frac{\pi}{2}$) obtained for a network of 4 neurons equipped with all-all homogeneous coupling at $g_M = 0$, contradicting the phase model prediction in Table 7.9

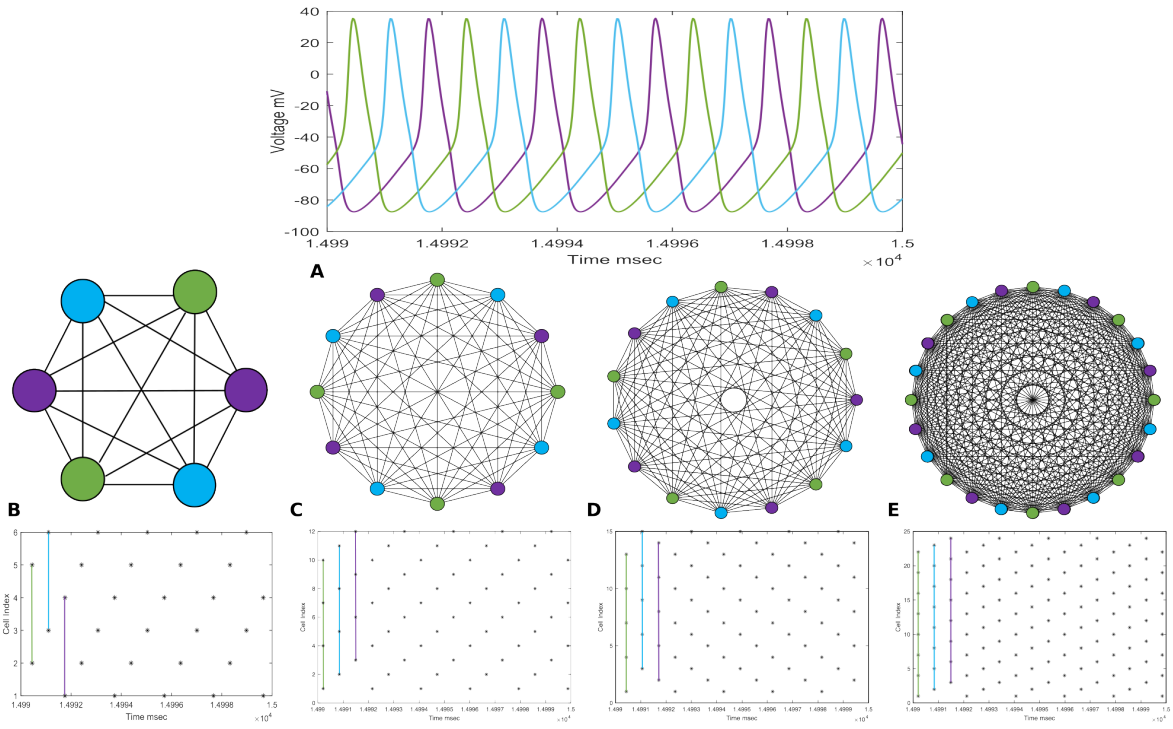


Figure 7.9: A 3−cluster obtained for a network of $6, 12, 15$ and 24 neurons equipped with all-all homogeneous coupling at $g_M = 0$. The voltage trace for the solution is presented in **(A)**. A 3−cluster solutions are illustrated in a network of **(A)** 3 cells, **(B)**12 cells and **(E)** 24 cells, all associated with $\psi = 2\frac{\pi}{3}$. **(D)** A 3−cluster solution obtained for a network of 15 cells associated with $\psi = 4\frac{\pi}{3}$.

comes from the following sum, described in Eq. 5.27.

$$\mu_0 = \sum_{k=0}^{n-1} H'\left(k\frac{2\pi}{n}\right) \tag{7.11}$$

Breaking this down further, we evaluate this sum for a $2-$cluster and $3-$cluster solution.

$$2 \text{ cluster} : \; H'(0) + H'(\pi) \tag{7.12}$$

$$3 \text{ cluster} : \; H'(0) + H'\left(2\frac{\pi}{3}\right) + H'\left(4\frac{\pi}{3}\right) \tag{7.13}$$

Both $H'(\pi)$ and $H'(\frac{2\pi}{3})$ are positive, whereas $H'(0)$ and $H'(4\frac{\pi}{3})$ are negative. These individual values are displayed in Table 7.6, for different approximations of H. We see that the approximation greatly varies as we jump from 30 to 100 and so on, in the evaluation of H' especially at 0. The failure in our predictions for these solutions, using a 30 term approximation, is thus attributed to the significance in the magnitude of $H'(0)$ in relation to $H'(\pi)$, $H'(\frac{2\pi}{3})$ and $H'(\frac{4\pi}{3})$.

	Number of terms			
	30	100	105	200
$H'(0)$	-0.0289	-0.0183	-0.0176	-0.0104
$H'(\pi)$	0.0196	0.0196	0.0195	0.0195
$H'(2\frac{\pi}{3})$	0.0723	0.0722	0.0722	0.0722
$H'(4\frac{\pi}{3})$	-0.0545	-0.0545	-0.0546	-0.0547

Table 7.6: Evaluation of the derivative of the interaction function, H at $0, \pi, 2\frac{\pi}{3}$ and $4\frac{\pi}{3}$ under increasing number of Fourier terms used in the approximation.

When we compared the remaining predictions for $n-$clusters, where $n > 3$ and the interaction function, H, was approximated by 200 terms (this is the maximum number of terms available to us from XPPAUT), the stabilities were consistent with the 30 term approximation. As the size of the cluster, n, increases, the corresponding μ_j and μ_0 are composed of an increasing amount of terms, that keep track of the phase differences for a single cell to all of its neighbours. As an example, for $n = 8$, the sum in Eq. (7.11) consists of terms that play a role in the stability of $2-$ and $4-$ cluster solutions. Additionally, the extra terms also classify the stability of different $8-$ cluster solutions that are considered in a nearest neighbours coupling. As we will see that not all $8-$cluster solutions in the nearest neighbours case are stable for $g_M = 0$ (determined by the negative value of $H'_{odd}(\psi)$), which

contributes to the instability of any $8-$cluster solution in the globally homogeneous case. As such, for the larger $n-$cluster solutions, the burden of destabilizing the solution is shared among other terms, in addition to $H'(0)$, and so is more forgiving of the error in its approximation.

Based on this, we revise our prediction step in the next section, where we consider a special case of the all-to-all coupling with distance dependent synaptic weights, and use a $100-$term approximation of the interaction function, H.

7.4 A network of arbitrary size with all-to-all globally heterogeneous coupling

In this section we consider a network of reduced Traub-Miles (RTM) model neurons equipped with weak all-to-all distance dependent coupling. A description for this coupling is given in Section 5.2.2.

$$\frac{dV_i}{dt} = I_{app} - I_{ionic}(V) - \frac{g_{syn}}{N}\sum_{j\neq i}^{N} p^{(j-i)modN} s_j(V_i - V_{syn}) \tag{7.14}$$
$$\frac{ds_i}{dt} = 5\left(1+\tanh\left(\frac{V_i}{4}\right)\right)(1-s_i) - \frac{s_i}{2} \qquad i = \{1,2,..,N\}$$

If p is set to 1, then Eq. (7.14) reduces to Eq. (7.10). In contrast to the nearest neighbours and all-to-all global homogeneous coupling, the heterogeneity in the coupling ($p \neq 1$) makes it difficult to derive some minimal condition that is independent of the size of the network (N) or cluster (n) to guarantee asymptotic stability. Instead we need to compute all the eigenvalues, μ_j given by Eq. (5.16). We consider this type of coupling, as way to study the recurrent connections within CA3, with a globally heterogeneous distribution of synaptic weights. We call this distance-dependent since the weight of the coupling, w_i, from each cell decreases monotonically with i. The stability analysis is summarized in Tables 7.7 and 7.8.

7.4.1 Phase model predictions

We use the phase model approximation of Eq. (7.14)[3] to predict the stability of symmetric $n-$cluster solutions, where the phase differences between adjacent cells are equal ($\psi_i = \psi$), for a network of size N. Setting $p = 0.5$, the stability predictions for the symmetric clusters are summarized in Tables 7.7 and 7.8 for networks $N = 4, 5, 6, 8, 10, 12, 20$ and 24. A periodic solution where adjacent cells are spiking with a phase difference (ψ) in the form of $\frac{2\pi k}{N}$ for some $k \in \{1, 2, .., N\}$ is admissible for a network of size N. In Tables 7.7 and 7.8, for a given value of the M-current conductance (g_M), the stability trend is summarized in each row corresponding to a (N, ψ) pair by computing Eq. (5.16).

As expected, the stability trend for the in-phase is identical to that of a pair of weakly coupled neurons, due to the fact that the stability criteria for the in-phase ($n = 1, \psi = 0$)

[3]Based on our observations in the previous section, we use a $100-$ term approximation of the H function to determine the stability predictions.

is independent of the size of the network N and the coupling architecture. When g_M is set to 5, up until $N = 10$, the phase model predictions are identical to the case of the global homogeneous coupling with the in-phase state being the only stable solution. Beyond $N = 10$, the phase model predicts that at least one splay solution is stable in addition to the synchronized state.

When g_M is set to 0 or 2, the phase model predicts that there are multiple stable $n-$cluster solutions. As observed in the previous section, the phase model predicted that $n-$clusters ranging from $n = 2$ to $n = 7$ were stable for a globally homogeneous coupled network ($p = 1$). In this case, the phase model predicts there are also stable $n-$cluster solutions for $n > 7$, corresponding to some ψ, for appropriate networks ($N > 7$).

As opposed to the global homogeneous case, for a given g_M, a particular $n-$cluster solution can differ in stability for the same network (N) but with different values of ψ. For example, consider $N = 8$, when there is no M-current ($g_M = 0$), the phase model predicts that an $8-$cluster solution (splay state) with $\psi = \frac{\pi}{4}$ is unstable but stable if $\psi = 3\frac{\pi}{4}$. An $n-$cluster solution associated with the same ψ can also differ in stability across networks with different sizes, N. As an example, consider $N = 12$ in Table 7.7, when $g_M = 5$, the phase model predicts that a $12-$cluster with $\psi = \frac{\pi}{6}$ is stable. The same solution is predicted to be unstable for $N = 24$ in Table 7.8, at $g_M = 5$.

7.4.2 Numerical studies

We studied networks $N = 4 - 16$ and 24 equipped with distance dependent coupling where p in Eq. (7.14), is set to 0.5. In Table 7.7, an $n-$cluster associated with a specific network size, N, and phase difference, ψ, is marked by * for a specific value of g_M, if we observed it during our simulations.

When g_M is set to 0, we obtained multiple $n-$cluster solutions that were predicted to be stable for each N. In particular, we obtained the anti-phase ($n = 2$, $\psi = \pi$) and $3-$cluster solutions for $N = 6, 8, 16$ and 24. The phase model also predicts that an $8-$cluster solution corresponding to $\psi = 3\frac{\pi}{4}$ (or $5\frac{\pi}{4}$) is stable when g_M is set to 0 for $N = 8$ and 16. We obtained these solutions for both networks. The anti-phase ($n = 2$, $\psi = \pi$), $3-$cluster and $8-$cluster solutions that were obtained for $g_M = 0$, are presented and discussed in Appendix C.4 as well.

When g_M is increased to 5, just as we had for a network with globally homogeneous synaptic weights, networks fully synchronize ($\psi = 0$) with globally heterogeneous weights. For $N > 8$, the phase model also predicts an additional splay solution for the network. In particular, it predicts a splay state in which adjacent cells spike with a phase difference

Table 7.7: Phase model predictions across different values of $g_M = \{0, 2, 5\}$ in RTM networks equipped with *distance-dependent coupling with* $p = 0.5$.

Network Size	Phase Difference	Value of g_M			Cluster Size
N	ψ	0	2	5	n
4	0	Unstable*	Unstable*	Stable*	1
	$\frac{\pi}{2}, 3\frac{\pi}{2}$	Stable*	Stable*	Unstable	4
	π	Stable*	Unstable	Unstable	2
5	0	Unstable*	Unstable*	Stable*	1
	$2\frac{\pi}{5}, 8\frac{\pi}{5}$	Stable	Stable*	Unstable	5
	$4\frac{\pi}{5}, 6\frac{\pi}{5}$	Stable*	Stable	Unstable	5
6	0	Unstable*	Unstable*	Stable*	1
	$\frac{\pi}{3}, 5\frac{\pi}{3}$	Stable	Stable	Unstable	6
	$2\frac{\pi}{3}, 4\frac{\pi}{3}$	Stable*	Stable*	Unstable	3
	π	Stable	Unstable	Unstable	2
8	0	Unstable*	Unstable*	Stable*	1
	$\frac{\pi}{4}, 7\frac{\pi}{4}$	Unstable	Unstable	Unstable	8
	$\frac{\pi}{2}, 3\frac{\pi}{2}$	Stable*	Stable*	Unstable	4
	$3\frac{\pi}{4}, 5\frac{\pi}{4}$	Stable*	Stable	Unstable	8
	π	Stable*	Unstable	Unstable	2
12	0	Unstable*	Unstable*	Stable*	1
	$\frac{\pi}{6}, 11\frac{\pi}{6}$	Unstable	Unstable	Stable*	12
	$\frac{\pi}{3}, 5\frac{\pi}{3}$	Stable	Stable	Unstable	6
	$\frac{\pi}{2}, 3\frac{\pi}{2}$	Stable*	Stable*	Unstable	4
	$5\frac{\pi}{6}, 7\frac{\pi}{6}$	Stable	Stable	Unstable	12
	$2\frac{\pi}{3}, 4\frac{\pi}{3}$	Stable*	Stable*	Unstable	3
	π	Stable*	Unstable	Unstable	2
16	0	Unstable*	Unstable*	Stable*	1
	$\frac{\pi}{8}, 15\frac{\pi}{8}$	Unstable	Unstable	Stable*	16
	$\frac{\pi}{4}, 7\frac{\pi}{4}$	Unstable	Unstable	Unstable	8
	$3\frac{\pi}{8}, 13\frac{\pi}{8}$	Stable	Stable	Unstable	16
	$\frac{\pi}{2}, 3\frac{\pi}{2}$	Stable*	Stable*	Unstable	4
	$5\frac{\pi}{8}, 11\frac{\pi}{8}$	Unstable	Unstable	Unstable	16
	$3\frac{\pi}{4}, 5\frac{\pi}{4}$	Stable*	Stable	Unstable	8
	$7\frac{\pi}{8}, 9\frac{\pi}{8}$	Stable	Unstable	Unstable	16
	π	Stable*	Unstable	Unstable	2

Table 7.8: Phase model predictions across different values of $g_M = \{0, 2, 5\}$ in RTM networks equipped with *distance-dependent coupling with* $p = 0.5$.. *Continuation from Table 7.7*

Network Size N	Phase Difference ψ	g_M			Cluster Size n
		$g_M = 0$	$g_M = 2$	$g_M = 5$	
24	0	Unstable*	Unstable*	Stable*	1
	$\frac{\pi}{12}, 23\frac{\pi}{12}$	Unstable	Unstable	Stable*	24
	$\frac{\pi}{6}, 11\frac{\pi}{6}$	Unstable	Unstable	Unstable	12
	$\frac{\pi}{4}, 7\frac{\pi}{4}$	Unstable	Unstable	Unstable	8
	$\frac{\pi}{3}, 5\frac{\pi}{3}$	Stable	Stable*	Unstable	6
	$5\frac{\pi}{12}, 19\frac{\pi}{12}$	Stable	Stable	Unstable	24
	$\frac{\pi}{2}, 3\frac{\pi}{2}$	Stable*	Stable*	Unstable	4
	$7\frac{\pi}{12}, 11\frac{\pi}{12}$	Stable	Stable	Unstable	24
	$5\frac{\pi}{6}, 7\frac{\pi}{6}$	Stable	Stable	Unstable	12
	$2\frac{\pi}{3}, 4\frac{\pi}{3}$	Stable*	Stable*	Unstable	3
	$3\frac{\pi}{4}, 5\frac{\pi}{4}$	Stable	Stable	Unstable	8
	π	Stable*	Unstable	Unstable	2

of $\psi = 2\frac{\pi}{N}$ or $(2N-2)\frac{\pi}{N}$. These type of solutions were obtained for $N = 12, 16$ and 24 and presented in Figure 7.10. In each case illustrated in panels (A)-(C), cells within the network, spike in the order of $C_1 - C_2 - \cdots - C_{N-1} - C_N$ corresponding to $2\frac{\pi}{N}$ for $N = 12, 16$ and 24 respectively.

Next, we initialized a network with no $M-$current ($g_M = 0$) in one of the predicted stable $n-$cluster solutions and applied transient perturbations in the form of an increased external current pulse, to a subset of the cells during the time interval $[8000, 8050]$. The perturbations can switch the network into a different stable $n-$cluster or a different realization of the initial one. In Figure 7.11, panels (A) and (C) show the raster plot for a network of 8 and 16 cells respectively, each initialized in a stable $4-$ cluster solution corresponding to $\psi = \frac{\pi}{2}$ (with a firing order : $C_1 - C_2 - C_3 - C_4$). Panels (B) and (D) show one case, in which the both networks switch from the initial $4-$cluster solution to a different realization corresponding to an inter-cluster phase difference of $\psi = 3\frac{\pi}{2}$. The final solution is predicted to be a stable solution in Table 7.7, and reverses the firing order $(C_1 - C_4 - C_3 - C_2)$. Panels (C) and (D) show a second possibility, in which by perturbing a different subset of cells, the network switches to an $8-$cluster solution corresponding to a phase difference $\psi = 7\frac{\pi}{4}$ (with a firing order : $C_1 - C_6 - C_3 - C_8 - C_5 - C_2 - C_7 - C_4$), which is a reverse of the solution associated with $\psi = 3\frac{\pi}{4}$.

Similarly, for a network of 12 RTM model neurons with no M-current ($g_M = 0$) , initialized in a stable $4-$cluster solution with an inter-cluster phase difference of $\psi = \frac{\pi}{2}$, a transient perturbation can reverse the firing order of the initial state and switch the network to a different stable $4-$cluster solution associated with $\psi = 3\frac{\pi}{2}$. The network can also switch into different stable $12-$cluster solutions by applying the perturbation to a different subset of cells, associated with a ψ that is either $5\frac{\pi}{6}$or $7\frac{\pi}{6}$. The solutions for this network is further discussed in Appendix C.4.

When g_M is increased to 5, networks initialized in the synchronized state persist under the transient perturbations. However, for a network of size $N > 8$ (from Table 7.7), initialized in a splay solution, applying a perturbation to at least half the cells could synchronize the network. This is illustrated in panels (A)-(C) in Figure 7.12 respectively, for a network of 12 ,16 and 24 cells , initialized in a splay solution, synchronize after a perturbation is applied to half of the cells.

In our simulations for $g_M = 0$, we also observed solutions where the network switched into a symmetric $n-$cluster with heterogeneous adjacent phase differences (ψ_i). Although, our predictions in Table 7.7 do not apply, the phase model, in general under periodic boundary conditions, may still admit these solutions, however more work needs to be done to verify these solutions. In Figure 7.13, panel (A) shows the transition of a network of 8 cells initialized in an anti-phase solution to a $4-$cluster solution with clusters, as per usual, given by $C_i = \{i, i+4\}$ for $i = \{1, 2, 3, 4\}$. The order in which the clusters fire, however, is different and given by: $C_1 - C_4 - C_3 - C_2$, which is not a predicted solution since this implies unequal phase differences.

Recall that ψ_i is the phase difference between cell $i+1 \pmod N$ and cell i, ($\psi_i = \theta_{i+1} - \theta_i$). Then the $4-$cluster solution obtained in the final state could correspond to a solution with the following phase difference distributions.

$$\vec{\psi} = \left[3\tfrac{\pi}{4}, \tfrac{\pi}{4}, 3\tfrac{\pi}{4}, \tfrac{\pi}{4}, 3\tfrac{\pi}{4}, \tfrac{\pi}{4}, 3\tfrac{\pi}{4}, \tfrac{\pi}{4}\right] \tag{7.15}$$

Note that (7.15) still satisfies periodic boundary conditions and also corresponds to the firing order observed. The same transition is also observed for networks of 16 and 24 cells initialized in a predicted stable $4-$cluster solution $\left(\psi = \frac{\pi}{2}\right)$, illustrated in panels (C) and (D) respectively in Figure 7.13.

In panel (B), a network of 12 cells, initialized in an anti-phase solution, switches to a $4-$cluster solution with a firing order given by: $C_1 - C_3 - C_2 - C_1$. We propose the following phase difference distribution between each cell:

$$\vec{\psi} = \left[3\tfrac{\pi}{4}, \tfrac{\pi}{4}, \tfrac{\pi}{4}, 3\tfrac{\pi}{4}, 3\tfrac{\pi}{4}, \tfrac{\pi}{4}, \tfrac{\pi}{4}, 3\tfrac{\pi}{4}\right] \tag{7.16}$$

The verification of whether the solutions described by (7.15) and (7.16), are indeed phase model predicted stable solutions, is left for future work.

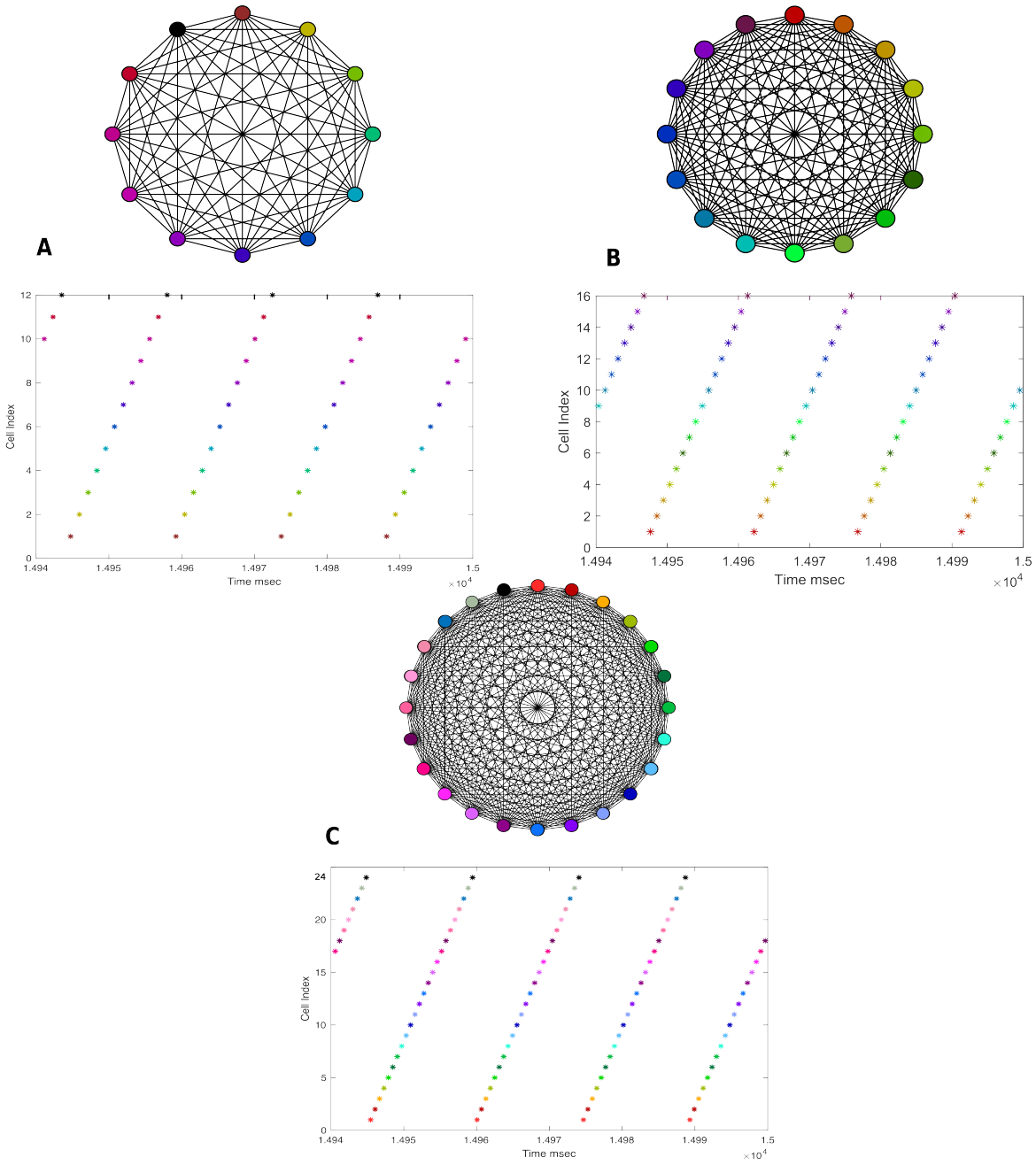


Figure 7.10: Demonstration of splay state solutions for RTM networks equipped with distance-dependent coupling ($p = 0.5, k = \lfloor N/2 \rfloor$) with g_M set to 5. **(A)** A splay solution for a network of 12 cells, spiking with a phase difference $\psi = \frac{\pi}{6}$. **(B)** A splay solution for 16 cells with a phase difference $\psi = \frac{\pi}{8}$. **(C)** A splay solution obtained for a network of 24 neurons with $\psi = \frac{\pi}{12}$. In each case, the cells fire in the order of $1 - 2 - 3 - \cdots - N$ as illustrated through the raster plots.

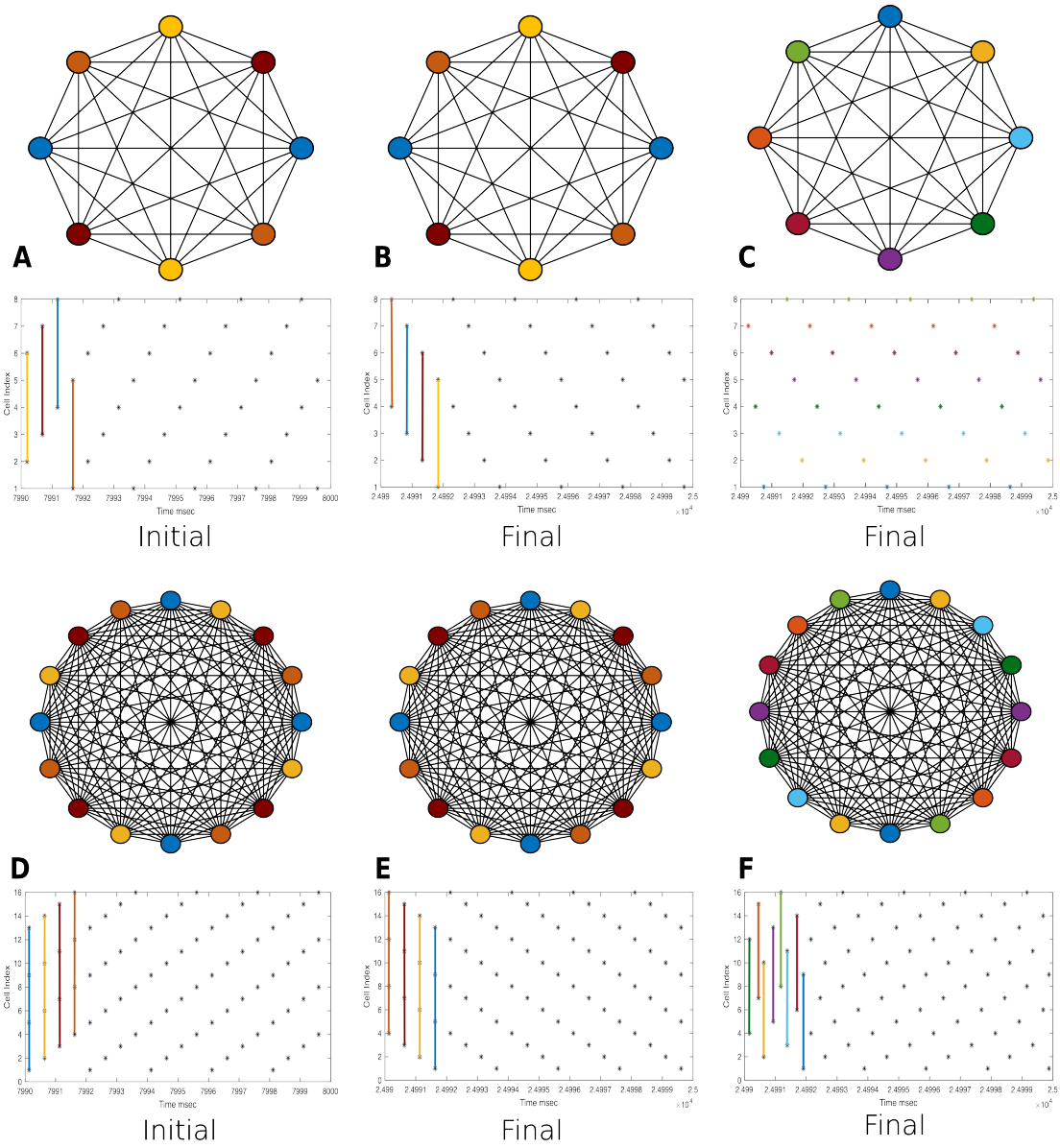


Figure 7.11: Multistability in a network of RTM model neurons, equipped with global distance dependent coupling ($p = 0.5$), when g_M is set to 0. In each case, the network is initialized in a stable cluster solution and a transient perturbation is applied to a subset of the cells during time $t \in [8000, 8050]$. **(A)** Network of 8 cells is initialized in a stable $4-$cluster solution $\left(\psi = \frac{\pi}{2}\right)$. **(B)** The perturbation reverses the firing order of the spiking cells from (A), switching the network to a different stable $4-$cluster solution $\left(\psi = 3\frac{\pi}{2}\right)$. **(C)** A perturbation applied to a different subset of cells, can switch the initial state in (A) to a stable $8-$cluster $\left(\psi = 7\frac{\pi}{4}\right)$. **(D)** Network of 24 cells is initialized in a stable $4-$cluster solution $\left(\psi = \frac{\pi}{2}\right)$. **(E)** The perturbation switches the network in (D) to a different stable $4-$cluster solution $(\psi = 3\frac{\pi}{2})$ **(F)** The network in (D) can also switch to a stable $8-$cluster $\left(\psi = 7\frac{\pi}{4}\right)$.

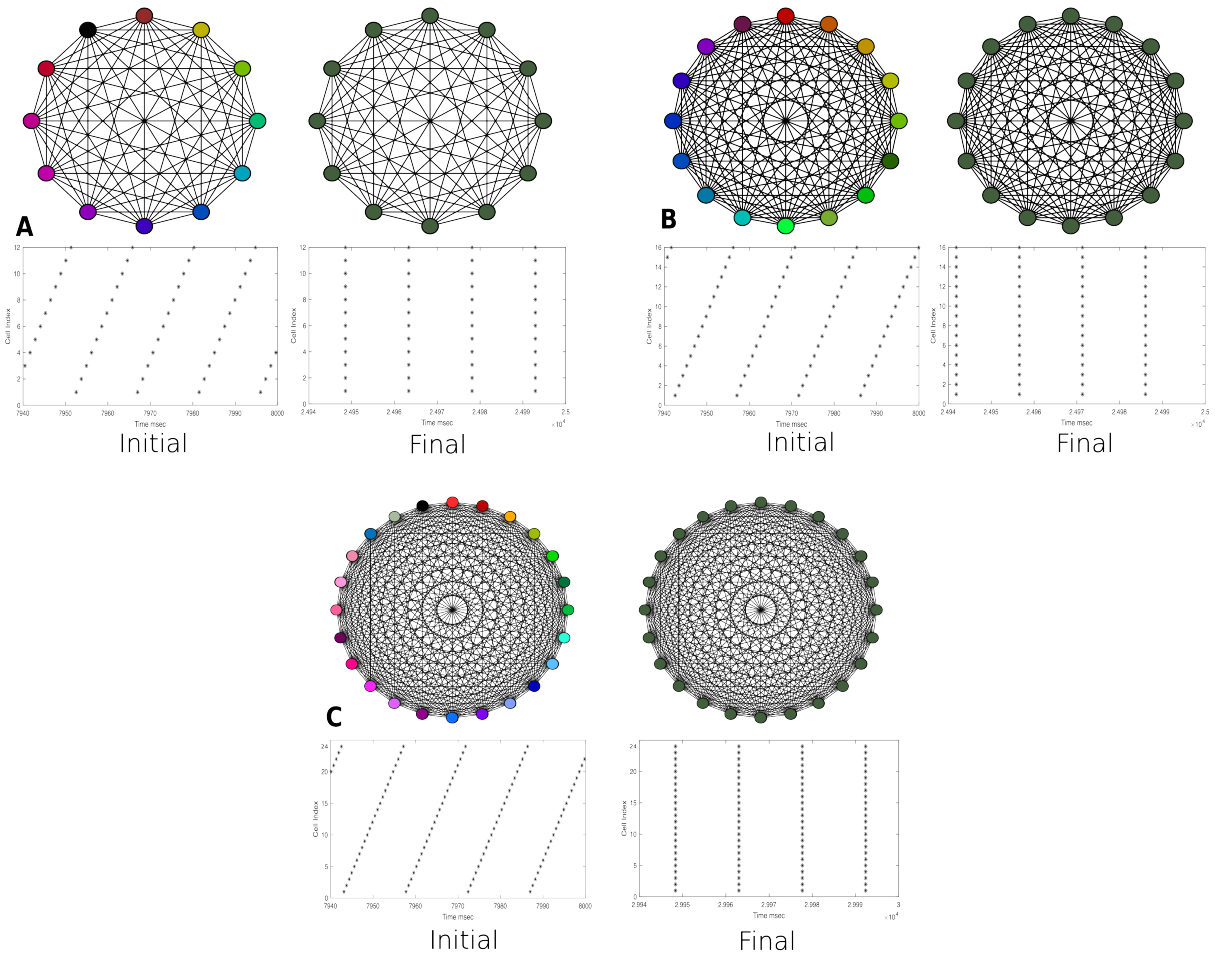


Figure 7.12: Multistability in a network of RTM model neurons with g_M set to 5, and with globally heterogeneous synaptic weights. A transient perturbation is applied during time $t \in [8000, 8050]$ to a network initialized in a stable splay solution. **(A)** Network of 12 cells, initialized in a stable splay solution $\left(\psi = \frac{\pi}{6}\right)$, synchronizes when 6 of the cells are perturbed transiently. **(B)** Network of 16 cells, initialized in a stable splay solution $\left(\psi = \frac{\pi}{8}\right)$, synchronizes when 8 of the cells are perturbed transiently. **(C)** Network of 24 cells, initialized in a stable splay solution $\left(\psi = \frac{\pi}{12}\right)$, synchronizes when 12 of the cells are perturbed transiently.

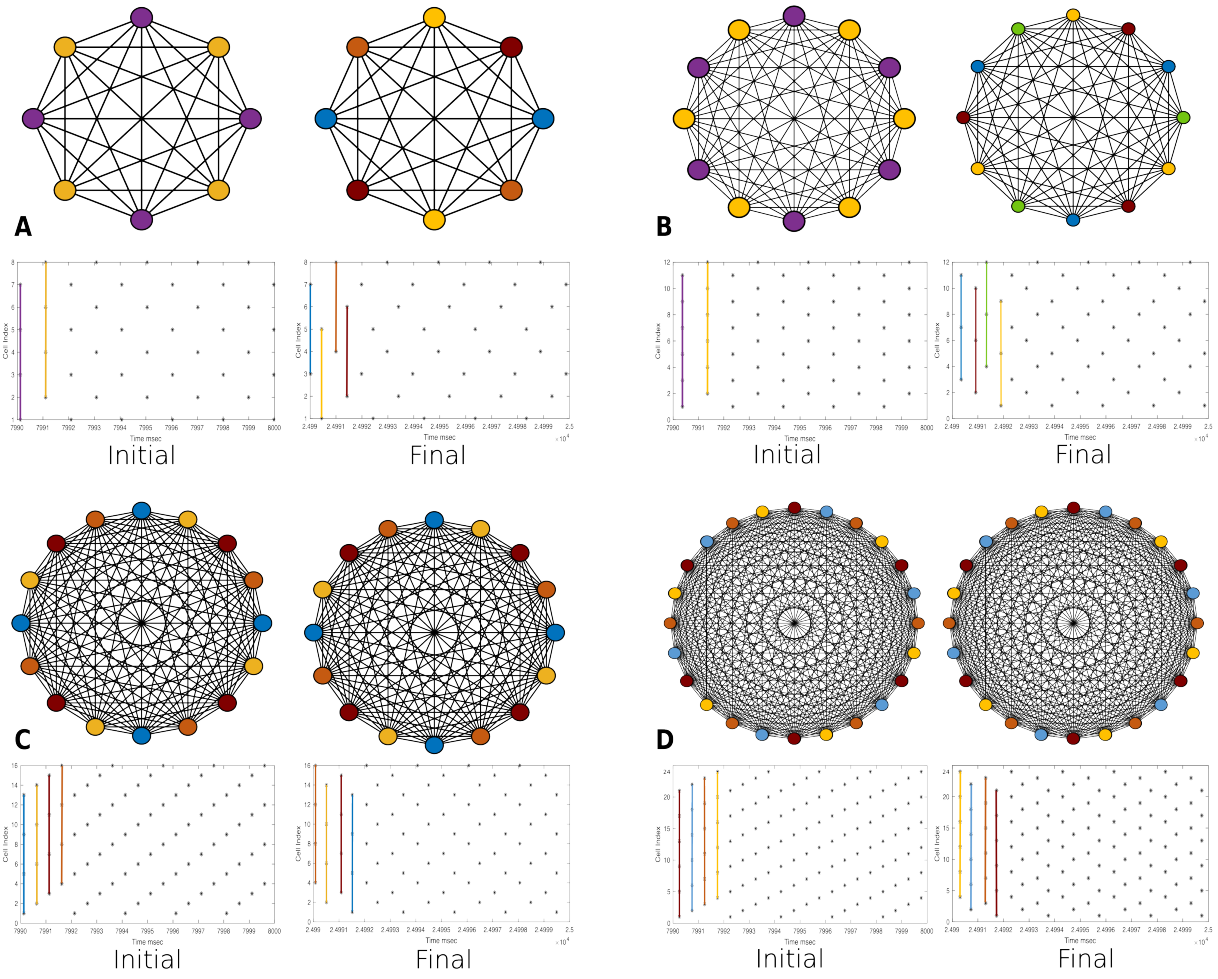


Figure 7.13: Demonstration of transitions between cluster solutions for a network of RTM model neurons, equipped with nearest neighbours coupling, with g_M set to 0. In this case, the network is initialized in a stable cluster solution as predicted by the phase model, and under the transient current pulse, it will switch to a symmetric cluster solution where the phase differences between adjacent cells are heterogeneous. **(A)** A network of 12 cells is initialized in an anti-phase solution with each cluster C_i defined by $\{i, i+2, \ldots, N-2+i\}$ for $i = \{1, 2\}$. Applying a transient pulse can switch it to a $4-$cluster solution with clusters C_i defined by $\{i, i+4\}$ for $i = \{1, 2, 3, 4\}$ and a firing order: $C_1 - C_4 - C_2 - C_3$.**(B)** A network of 24 cells is initialized in an anti-phase solution with each cluster C_i defined by $\{i, i+2, \ldots, N-2+i\}$ for $i = \{1, 2\}$. Applying a transient pulse can switch it to a $4-$cluster solution with clusters C_i defined by $\{i, i+4\}$ for $i = \{1, 2, 3, 4\}$ and a firing order: $C_1 - C_3 - C_2 - C_4$. **(C)** A network of 12 cells is initialized in a stable $4-$cluster associated with $\psi = \frac{\pi}{2}$. The transient pulse changes the firing order from $C_1 - C_2 - C_3 - C_4$ to $C_1 - C_4 - C_2 - C_3$. **(D)** A network of 12 cells is initialized in a stable $4-$cluster associated with $\psi = \frac{\pi}{2}$. The transient pulse changes the firing order from $C_1 - C_2 - C_3 - C_4$ to $C_1 - C_4 - C_2 - C_3$.

7.5 A network of arbitrary size with nearest neighbour coupling

We now consider a network of reduced Traub Miles (RTM) model neurons equipped with weak nearest neighbours coupling, such that each neuron X_i will synaptically excite its adjacent neighbours X_{i-1} and X_{i+1} with $i \pmod N$.

$$\frac{dV_i}{dt} = I_{app} - I_{ionic}(V) - \frac{g_{syn}}{2} \cdot \left(s_{(i-1) \mod N}(V_i - V_{syn}) + s_{(i+1) \mod N}(V_i - V_{syn})\right) \quad (7.17)$$
$$\frac{ds_i}{dt} = 5(1 + \tanh(\frac{V_i}{4}))(1 - s_i) - \frac{s_i}{2} \qquad i = \{1, 2, .., N\}$$

In this case, the coupling strength ε associated with Eq. (7.17), is defined by the maximal synaptic conductance, $g_{syn}/2$, since each neuron will receive contributions from two neighbours. The conditions guaranteeing the stability of a phase-locked solution for this network of this form is reviewed in Chapter 5. In particular, we learned that the stability of a symmetric $n-$ cluster solution for a network, where the adjacent phase differences are equal ($\psi_i = \psi$), is independent of the size of the network, N. In fact, the stability condition is identical to the case of pair of weakly coupled neurons. This type of coupling does not reflect the standard highly recurrent connections of the CA3 excitatory sub-network, but can provide insight on the implications of acetylcholine on a network with reduced connectivity.

7.5.1 Phase model predictions

Using the phase model approximation of Eq. (7.17) [4] , we predict the stability of symmetric $n-$ cluster solutions for an arbitrary network, where the adjacent cells repetitively spike with a phase difference of ψ. The predictions are summarized in Table 7.9 for $n = 1, 2, .., 10, 12, 15$. If N is divisible by n, then a corresponding network of size N can admit an $n-$cluster solution with $\psi = 2\frac{\pi k}{N}$ for some $k < N$. For a given strength of the M-current (determined by g_M), the stability trend of an $n-$ cluster is summarized in each row corresponding to a specific ψ by checking if the condition in Corollary 5.2.1.1 is satisfied.

[4]The stability criteria only depends on the sign of H'_{odd} evaluated at the identical phase difference (ψ) as established in Corollary 5.2.1.1. So the phase model approximation in this section uses the same number of terms as the case of a pair of weakly coupled neurons. (30 terms)

The in-phase solution, as expected, follows the same stability trend as the prior cases, with the whole network synchronizing as the M-current in the system increases. Unlike the previous cases, when g_M is set to 5, the phase model predicts that there are multiple stable $n-$cluster solutions beyond the splay state and the synchronized state. When g_M is set to 0 or 2, the phase model predictions are similar to the previous cases, with multiple stable $n-$ cluster solutions. Similar to the distance dependent case, for a given g_M, a particular $n-$cluster solution can differ in stability for differing values in ψ. For example, consider $n > 4$ and $n \neq 6$, for which there is at least one ψ corresponding to unstable, and one that is stable for each g_M. Unlike the distance dependent coupling case, an $n-$cluster solution associated with the same ψ is stable for all applicable networks $(n|N)$.

Recall that the predictions made in Table 7.9 are independent of N. If we consider a larger network of 24 (or 300 neurons), then based on the phase model analysis of networks of sizes 3 through 15, we can predict the stability of the $1-$cluster, $2-$clusters, $3-$clusters,$4-$clusters, $6-$clusters, $8-$clusters and $12-$clusters (along with 5 and 10 for $N = 300$) at different values of g_M.

7.5.2 Numerical studies

We verify the predictions from Table 7.9, by running simulations in MATLAB. We studied networks with $N = 5, 6, \ldots, 15$ with g_{syn} set to 0.2. In general, the symmetric cluster solutions that emerged in the simulations agreed with the phase model predictions. As a brief summary of the correspondence between our phase model predictions and numerical simulations, in Table 7.9, we marked the solutions that were verified through numerical simulations by an *.

When g_M was set to 0, we found multiple $n-$cluster solutions that were predicted to be stable. In particular, we obtained the anti-phase $(n = 2, \psi = \frac{\pi}{2})$, $3-$cluster and $5-$cluster solutions found for networks of arbitrary sizes. Although the phase model predicts stable $4-$cluster,$6-$cluster and $8-$cluster solutions, we were unable to obtain these solutions for an even network. We did, however, obtain the $4-$cluster for a network of 4 cells. In addition to this, we obtained splay states for $N = 7$ and 9. These solutions are presented and discussed in Appendix C.5.

When g_M was increased to 5, in addition to the fully synchronized solution ($\psi = 0$, not illustrated), we also found several non-trivial $n-$cluster solutions. Unlike the distance dependent case, we could find splay states for networks smaller than 10. As an example, consider Figure 7.14, where panels (A) and (B) show the splay states that were obtained

Phase Difference	Value of g_M			Cluster Size
ψ	0	2	5	n
0	Unstable*	Unstable*	Stable*	1
$2\frac{\pi}{15}, 28\frac{\pi}{15}$	Unstable	Unstable	Stable*	15
$\frac{\pi}{6}, 11\frac{\pi}{6}$	Unstable	Unstable	Stable*	12
$\frac{\pi}{5}, 9\frac{\pi}{5}$	Unstable	Unstable	Stable*	10
$2\frac{\pi}{9}, 16\frac{\pi}{9}$	Unstable	Unstable	Stable	9
$\frac{\pi}{4}, 7\frac{\pi}{4}$	Unstable	Unstable	Stable*	8
$2\frac{\pi}{7}, 12\frac{\pi}{7}$	Unstable	Unstable	Stable*	7
$4\frac{\pi}{15}, 26\frac{\pi}{15}$	Unstable	Unstable	Stable*	15
$\frac{\pi}{3}, 5\frac{\pi}{3}$	Unstable	Stable	Stable*	6
$2\frac{\pi}{5}, 8\frac{\pi}{5}$	Stable*	Stable*	Stable*	5
$4\frac{\pi}{9}, 14\frac{\pi}{9}$	Stable	Stable	Stable	9
$\frac{\pi}{2}, 3\frac{\pi}{2}$	Stable*	Stable*	Stable	4
$4\frac{\pi}{7}, 10\frac{\pi}{7}$	Stable	Stable	Unstable	7
$8\frac{\pi}{15}, 22\frac{\pi}{15}$	Stable	Stable	Unstable	15
$3\frac{\pi}{5}, 7\frac{\pi}{5}$	Stable	Stable	Unstable	10
$4\frac{\pi}{5}, 6\frac{\pi}{5}$	Stable*	Stable	Unstable	5
$6\frac{\pi}{7}, 8\frac{\pi}{7}$	Stable*	Stable	Unstable	7
$5\frac{\pi}{6}, 7\frac{\pi}{6}$	Stable	Stable	Unstable	12
$3\frac{\pi}{4}, 5\frac{\pi}{4}$	Stable	Stable*	Unstable	8
$2\frac{\pi}{3}, 4\frac{\pi}{3}$	Stable*	Stable*	Unstable	3
$8\frac{\pi}{9}, 10\frac{\pi}{9}$	Stable*	Unstable	Unstable	9
$14\frac{\pi}{15}, 16\frac{\pi}{15}$	Stable*	Unstable	Unstable	15
π	Stable*	Unstable*	Unstable*	2

Table 7.9: Phase model predictions for selected ψ across different values of $g_M(=\{0,2,5\})$ in a network with nearest neighbour coupling.

for a network of 5 and 7 cells, associated with $\psi = \frac{2\pi}{5}(C_1 - C_2 - C_3 - C_4 - C_5)$ and $\psi = \frac{12\pi}{7}(C_1 - C_7 - C_6 - C_5 - C_4 - C_3 - C_2)$ respectively.

We also obtained splay solutions for a network of 8 and 12 cells which are shown in Figure 7.15 corresponding to $\psi = \frac{2\pi}{N}$ where firing order of cells is $C_1 - C_2 - \cdots - C_N$. We also found non-trivial cluster solutions that were not splay states. Consider Figure 7.15, where panels (G),(H) and (I) show 6−clusters, 8−clusters and 12−clusters in a network of 24 cells. Panel (D) shows a 6−cluster in a network of 12 cells. In all cases, the cells fire in the same order, i.e., $\{C_1 - C_2 - \ldots C_N\}$ corresponding to $\psi = \frac{2\pi}{N}$ ($N = 12$ or 24

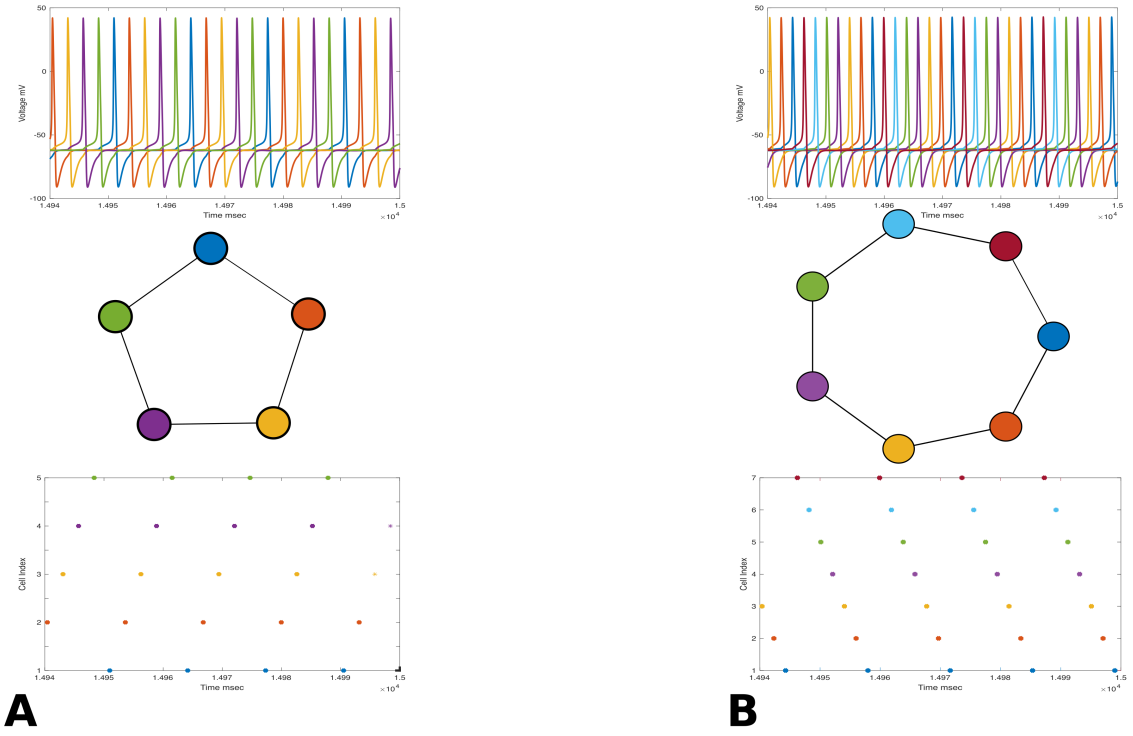


Figure 7.14: Splay states are obtained for a network of RTM model neurons, equipped with nearest neighbour coupling, with g_M set to 5. The solutions are presented in a similar format as Figure C.7. **(A)** A network of 5 cells spike individually corresponding to a $5-$cluster solution with $\psi = \frac{2\pi}{5}$. **(B)** A network of 7 cells exhibiting a $7-$cluster solution with $\psi = \frac{12\pi}{7}$.

accordingly).

A larger network of 300 RTM model neurons equipped with nearest neighbour coupling was considered next. This was done to demonstrate the independence of the predictions for a network equipped with nearest neighbour coupling, on its size, N. Accordingly, phase model predicts that the anti-phase, and the $n-$ cluster solutions for $n = 3$, 5, 6, 8 $\left(\psi = \frac{3\pi}{4}\right)$, 9 $\left(\psi = \frac{4\pi}{9}, \frac{8\pi}{9}\right)$, 10 $\left(\psi = \frac{3\pi}{10}\right)$, 12 $\left(\psi = \frac{5\pi}{6}\right)$ and 15 $\left(\psi = \frac{8\pi}{15}, \frac{14\pi}{15}\right)$ are stable when there is no M-current in the system, i.e., $g_M = 0$. We obtained an anti-phase $\left(\psi = \frac{\pi}{2}\right)$, $3-$cluster $\left(\frac{2\pi}{3}\right)$, $5-$cluster $\left(\psi = \frac{6\pi}{5}\right)$ and a $15-$cluster $\left(\psi = \frac{14\pi}{15}\right)$ solution as illustrated in panels (A),(B),(C) and (D) respectively in Figure 7.16. For each figure, we present a sub figure of a raster plot displaying the first n cells corresponding to each $n-$cluster solution, to verify the firing order.

When g_M is increased to 5, the phase model predicts that the in-phase ($\psi = 0$), 5-clusters, $6-$cluster, $8-$clusters $\left(\psi = \frac{\pi}{4}\right)$, $9-$clusters, $10-$clusters, $12-$clusters $\left(\psi = \frac{\pi}{6}\right)$ and the $15-$ clusters $\left(\psi = \frac{2\pi}{15}, \frac{4\pi}{15}\right)$ are stable. Through our simulations, we obtained a $5-$cluster $\left(\psi = \frac{2\pi}{5}\right)$, $6-$cluster $\left(\psi = \frac{\pi}{3}\right)$, $12-$cluster $\left(\psi = \frac{\pi}{6}\right)$ and a $15-$cluster $\left(\psi = \frac{2\pi}{15}\right)$ solution, which are illustrated in panels (A),(B),(C) and (D) respectively in Figure 7.17. For each figure, we present a sub figure of a zoomed display of the first n cells corresponding to each $n-$cluster solution, verifying the firing order and as a result the associated phase difference, ψ.

Finally, we tested the multistablity of the cluster solutions by applying a transient perturbation, in the form of a current pulse, to a subset of the cells in the network, initialized in one stable cluster solution, during the time interval $[8000, 8050]$. When g_M is set to 0, the anti-phase would remain persistent to these current pulses. Transitions induced by the transient current pulses, were observed for networks initialized in a stable $3-$ cluster solution. A transient current pulse applied to a subset of the cells could reverse the firing order of the cells forming a stable $3-$cluster solution associated with a different phase difference. Applying the perturbation to a different subset of cells can also switch networks to a stable $12-$cluster solution (if admissible). A third possibility could arise in which a perturbation to a subset of the cells could also switch the network to the anti-phase solution. These transitions were observed for a network of 12 and 24 RTM model neurons, which are presented and discussed in Appendix C.5.

When g_M is set to 5, networks initialized in the synchronized state persist under the transient perturbations. For networks initialized in a splay state, applying a perturbation to a subset of the cells, could synchronize the solution. This was observed for a network of 8 and 12 cells. This pulse-induced synchrony was also observed for a network of 12 cells that was initialized in a stable $6-$cluster state, associated with either $\psi = \frac{\pi}{6}$ or $\psi = \frac{\pi}{3}$.

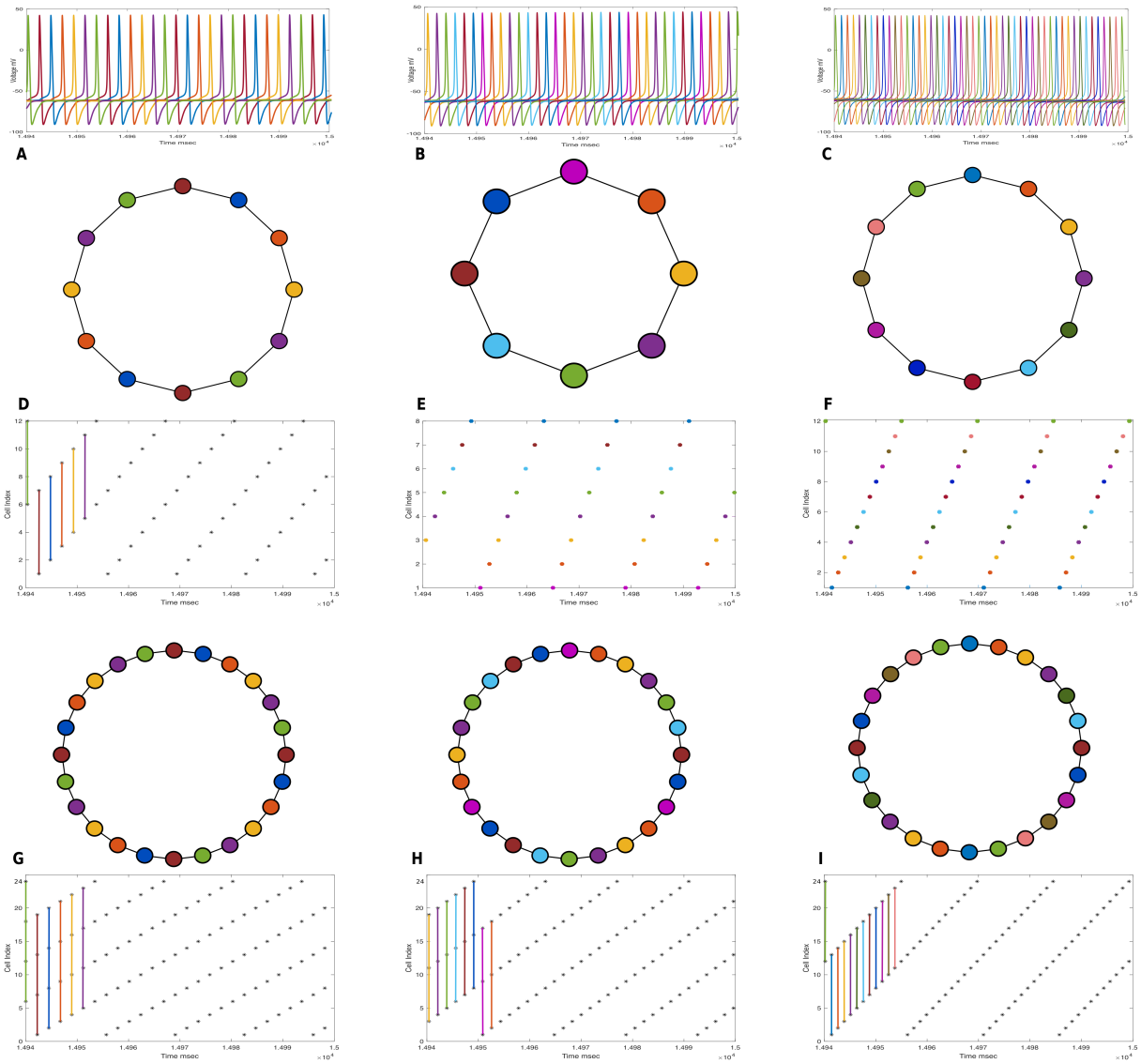


Figure 7.15: Multiple stable $n-$clusters are obtained for a network RTM model neurons, coupled in a nearest neighbour fashion, with g_M set to 5. The solutions for $n = 6, 8$ and 12 are presented in a similar format as Figure C.6. **(A)-(C)** display the representative voltage traces for each $n-$cluster. Panels **(D)** and **(G)** illustrate the $6-$cluster solution in a network of 12 and 24 cells resp, with $\psi = \frac{\pi}{3}$. Panels **(E)** and **(H)** demonstrate the $8-$cluster solution in a network of 8 and 24 cells resp with $\psi = \frac{\pi}{4}$. Panels **(F)** and **(I)** illustrate the $12-$cluster in a network of 12 and 24 cells resp, with $\psi = \frac{\pi}{6}$

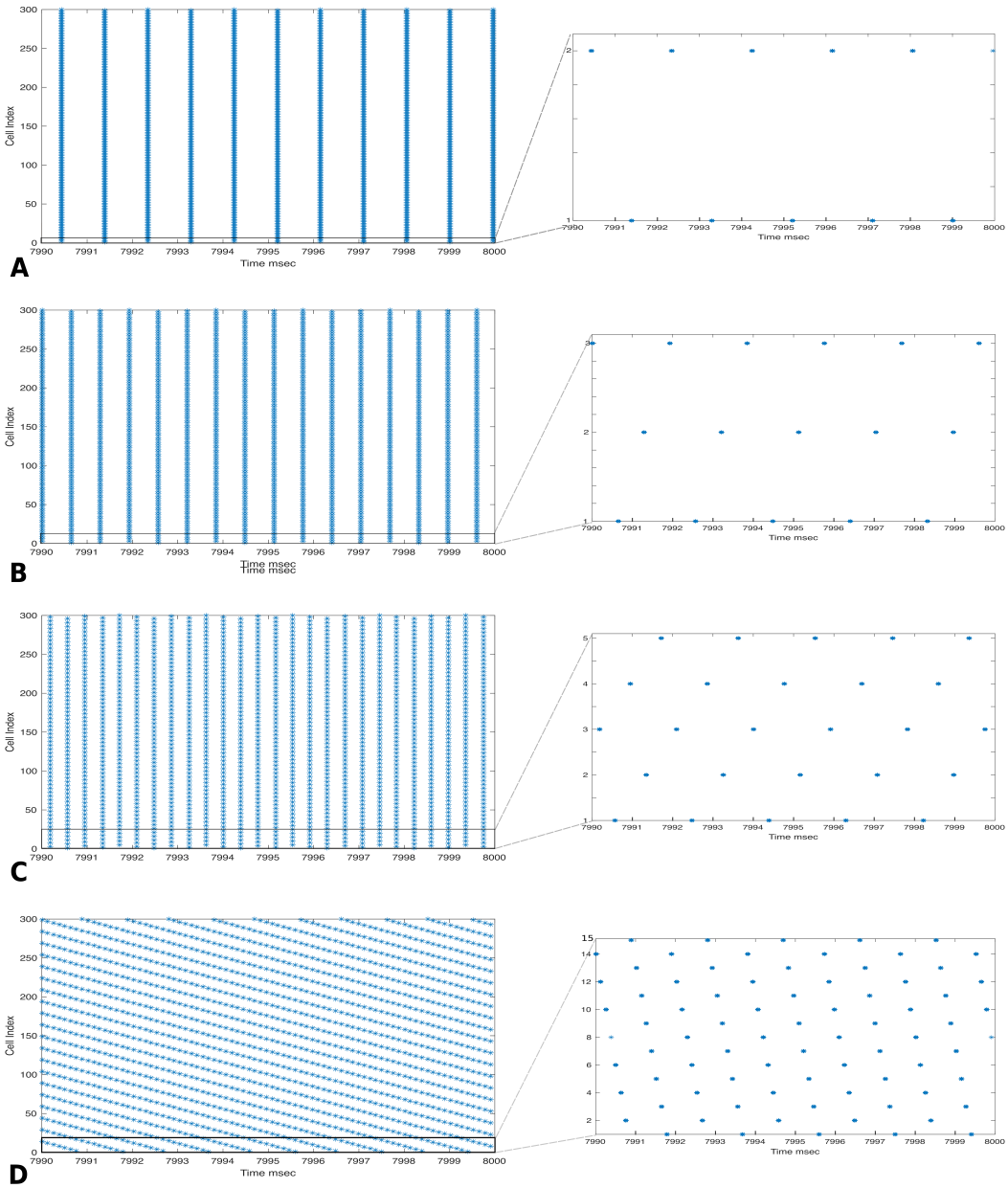


Figure 7.16: Demonstration of multistablity in a network of 300 model RTM neurons equipped with nearest neighbours coupling ($k = 1$), with g_M set to 0. Rasters are plotted for each $n-$cluster solution along with a sub-figure which displays the first n cells in the network. **(A)** Network exhibiting an anti-phase solution with two clusters formed. **(B)** A $3-$cluster solution is obtained with $\psi = \frac{2\pi}{3}$. **(C)** A $5-$cluster solution is obtained with $\psi = \frac{6\pi}{5}$. **(D)** A $15-$cluster solution obtained with $\psi = \frac{14\pi}{15}$

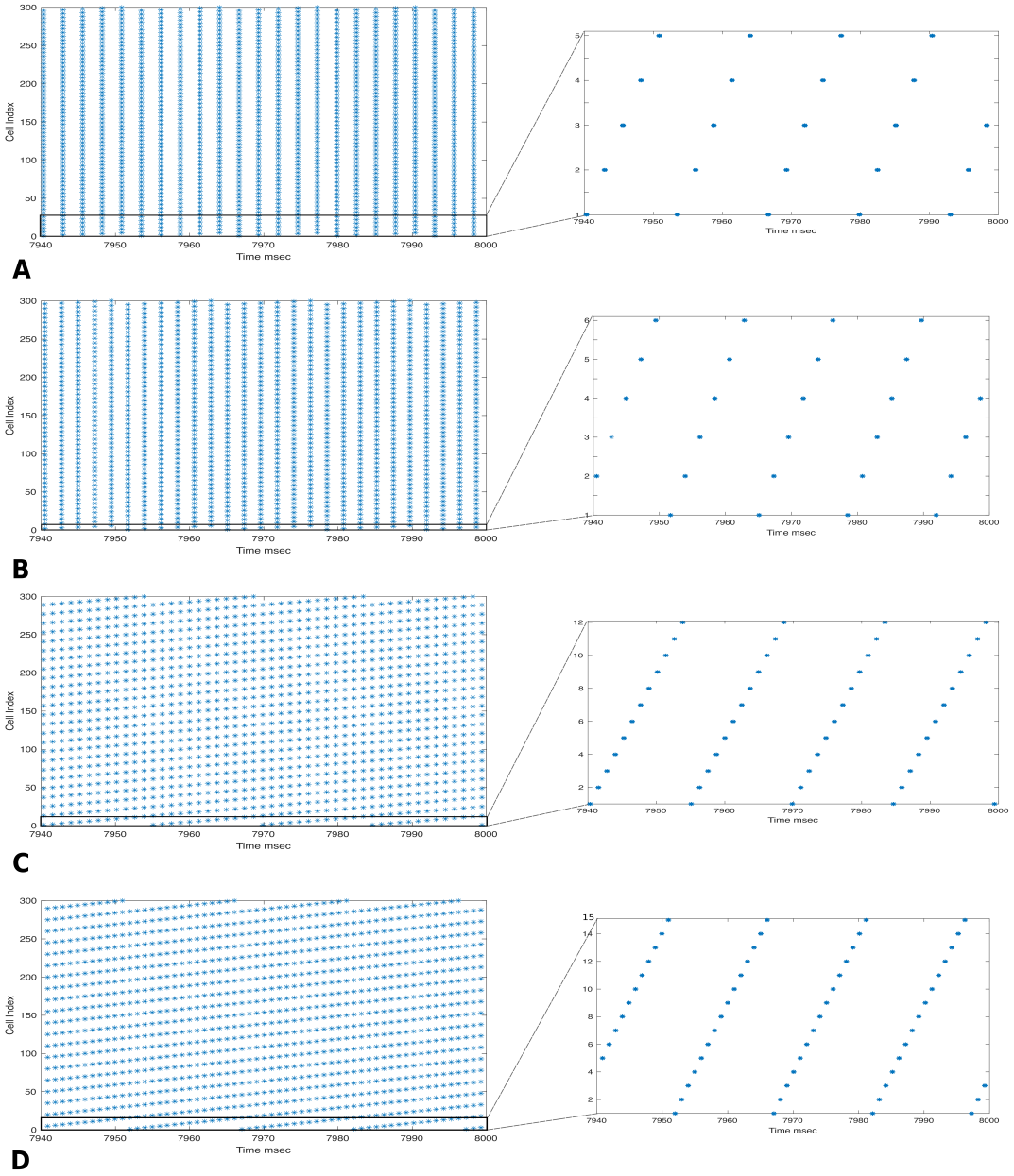


Figure 7.17: Demonstration of multistablity in a network of 300 model RTM neurons equipped with nearest neighbours coupling ($k = 1$), with g_M set to 5. Rasters are plotted for each $n-$cluster solution along with a sub-figure which displays the first n cells in the network. **(A)** Network exhibiting an $5-$cluster solution corresponding to $\psi = \frac{2\pi}{5}$. **(B)** A $6-$cluster solution obtained for the network with $\psi = \frac{\pi}{3}$. **(C)** A $12-$cluster solution is obtained with $\psi = \frac{\pi}{6}$. **(D)** A $15-$cluster solution is obtained with $\psi = \frac{2\pi}{15}$

These results are presented and further discussed in Appendix C.5.

The more interesting cases are the possible transitions obtained in a network of 24 cells, when g_M is set to 5, illustrated in Figure 7.18. Panel (A) depicts the network initialized in a stable 6−cluster solution associated with $\psi = \frac{\pi}{3}$. Applying a transient perturbation to a subset of the cells, can switch the network to a stable 12−cluster ($\psi = \frac{\pi}{6}$) or a stable 24−cluster solution ($\psi = \frac{\pi}{12}$), depicted in panels (B) and (E) respectively. Similarly, panels (C) and (D) show the network, initialized in a stable 8−cluster solution, associated with $\psi = \frac{\pi}{4}$, and a stable 12− cluster solution, associated with $\psi = \frac{\pi}{6}$ respectively. Similar to the 6−cluster solution, both initialized networks could separately switch to the stable 24−cluster solution associated with $\psi = \frac{\pi}{12}$, as illustrated in panel (E). For all three initial states displayed in panels (A),(C) and (D), the network can synchronize when a transient perturbation is applied to a different subset of cells as depicted in panel (F).

We now present an alternative to the stability analysis presented in Table 7.9. Based on our observations in Section 7.2, it is evident that within the domain $(0, \pi)$, the odd part of the interaction function, H_{odd}, exhibits a single extrema (maxima or minima) for both $g_M = 0$ and 5. For $g_M = 2$, however two extrema occur within this interval. We approximate the locations of these extrema and summarize the resulting stability behaviour in Figure 7.19. Panels (A)-(C), show the stability analysis for $g_M = 0, 2$ and 5 respectively. In each panel,a one-dimensional phase line is shown for ψ in $(0, \pi)$, with unstable regions highlighted in red and the stable regions highlighted in green. Essentially, this gives us a way to quickly check if a solution is stable, by calculating ψ and checking whether or not it belongs within the stable region. However, the main limitation of this approach is that for values of ψ near the extrema, a more careful analysis is required, as it can be difficult to determine the exact point at which the corresponding odd derivative vanishes. We can also see how for some n, we can find k such that $gcd(n, k) = 1$, $\psi = \frac{2\pi k}{n}$ and $H'_{odd}(\psi)$ lies within the positive intervals (marked by green) for $g_M = 0$ and $g_M = 5$, explaining the multistability seen for $g_M = 5$.

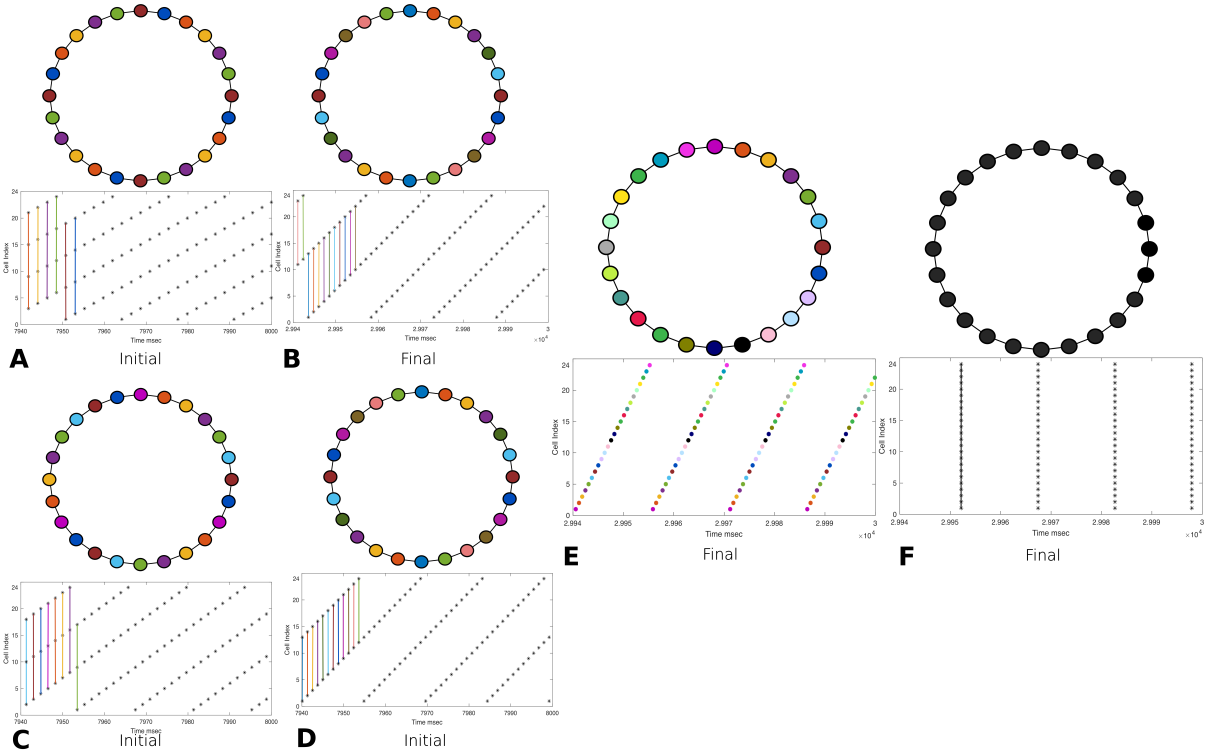


Figure 7.18: Demonstration of possible transitions between stable cluster solutions when g_M is set to 5, for a network of 24 RTM model neurons, equipped with nearest neighbour coupling. **(A)** The network is initialized in a stable 6− cluster solution ($\psi = \frac{\pi}{3}$) **(B)** A transient perturbation applied to a subset of cells in the network, can switch it to a stable 12−cluster solution associated with $\psi = \frac{\pi}{6}$ **(C)** The network is initialized in a stable 8− cluster solution associated with $\psi = \frac{\pi}{4}$. **(D)** The network is initialized in a stable 12− cluster solution associated with $\psi = \frac{\pi}{6}$. **(E)** A transient perturbation applied to subset of the cells in the network initialized in (A), (C) or (D), can switch them individually into a stable 24− cluster solution. **(F)** A transient perturbation applied to a different subset of the cells in the network initialized in (A), (C) or (D), can synchronize them.

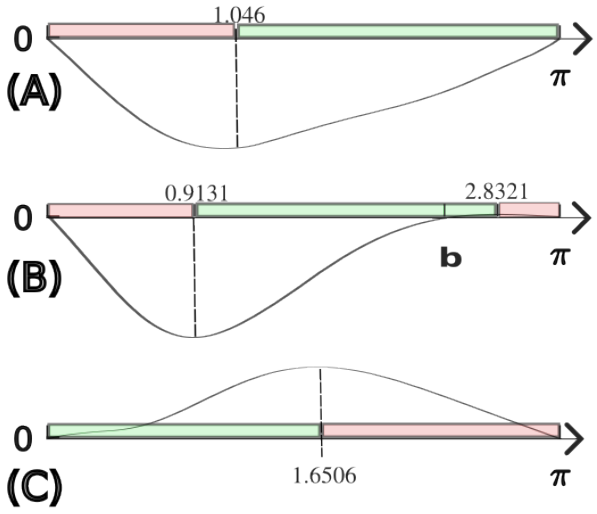


Figure 7.19: Stability analysis for nearest neighbours determined by the sign of H'_{odd} on $[0, \pi]$ for different values of g_M. In each panel, unstable regions are highlighted in red, while stable regions are shown in green. **(A)** When g_M is set to 0, around $\psi = 1.046$, H'_{odd} changes its sign from negative to positive, and the corresponding solution becomes stable. **(B)** When g_M is set to 2, the corresponding H'_{odd} changes sign twice, around $\psi = 0.9131$ and 2.8321. **(C)** At $g_M = 5$, it is essentially a reverse picture of $g_M = 0$, and H'_{odd} becomes negative around $\psi = 1.6506$, beyond which the corresponding cluster solutions are unstable.

Chapter 8

Discussion

In this study, we studied the effect of acetylcholine (ACh) on the synchrony of an excitatory hippocampal network with periodic boundary conditions, corresponding to a 1-dimensional ring. We examined special types of phase-locked solutions, known as cluster solutions, where individual cells fire repetitively, and form subgroups of neurons that fire synchronously.

Acetylcholine is an important neuromodulator that is essential for the learning and memory formation that occurs in the hippocampus. To study its effect, we introduced a biophysical, conductance-based model of a hippocampal pyramidal neuron in Chapter 6, the reduced Traub-Miles (RTM) model. The RTM neuron model was supplemented with a voltage dependent non-inactivating slow potassium current [36] called the muscarinic current (M-current), which is known to downregulate in the presence of ACh [54, 55, 126]. Using ideas introduced in Chapter 4 and 5, we derived a phase model approximation for the corresponding network of weakly coupled RTM model neurons (with the M-current) at a specific strength of the M-current conductance, to study the cluster solutions. We specifically focused on symmetric cluster solutions, in which the neurons organize themselves (temporally) into synchronous clusters, each spiking with fixed inter-cluster phase differences with one another. In this type of solution, the phase difference between adjacent neurons are equal and neurons belonging to the same cluster have a phase difference of zero. Each cluster also harbours an identical number of synchronized neurons [1]. We first applied this approach to a pair of synaptically coupled RTM model neurons and then extended the analysis to networks of weakly coupled identical neurons under different configurations of

[1] With the exception of all-to-all globally homogeneous coupling, where the adjacent phase differences were not necessarily identical.

coupling architecture.

In our work, cluster solutions in biophysical models of neuronal networks are linked to neural assemblies—groups of transiently synchronized neurons—which have been observed in the hippocampus and implicated in tasks involving spatial navigation as well as the encoding and storage of episodic memories [57, 27, 110, 121]. Using a phase model approach, we investigated the bidirectional role of acetylcholine (ACh) in neural assembly formation, focusing on the distinct assemblies supported by a network of pyramidal neurons in the CA3 region of the hippocampus under varying ACh levels (high vs. low).

The phase model analysis was first applied to a pair of RTM model neurons in Section 7.2, and the results are summarized as follows. When a pair of RTM model neurons are coupled with a weak excitatory synapse ($g_{syn} = 0.2 \ll 1$,$V_{syn} = 0$), the phase model predicts that they synchronize with stronger M-currents ($g_M = 5$), when the level of acetylcholine is 'low enough'. The neurons desynchronize, at 'higher levels' of acetylcholine ($g_M < 5$), into anti-phase ($g_M = 0$) and out-of-phase solutions ($g_M = 2$). These predictions agreed with our numerical simulations, and were consistent with the numerical results obtained for the same model in [4]. From a dynamical systems point of view, according to [4, 36], an excitatory neuron switches from Class II to Class I dynamics past the Bogdanov Takens (BT) point, brought about by a change in g_M. This result was also reproduced by plotting the bifurcation and frequency-current (F/I) curves in Chapter 6, demonstrating the Class I and Class II dynamics of the RTM model neuron at $g_M = 0$ and $g_M = 5$, respectively. The expected network level behaviour associated with the switch to Class II dynamics, is that neurons coupled together, with fast enough excitatory synaptic interactions, can synchronize [56] , which is observed in our results. We also find that the synchronized solution tends to occur for a value of g_M greater than the BT point, consistent with the findings in [4].

We then applied the phase model analysis to symmetric cluster solutions for a network of arbitrary size N, equipped with nearest-neighbour ($k = 1$) and all-to-all coupling ($k = \lfloor \frac{N}{2} \rfloor$, $p = 1, 0.5$), done in Sections 7.3–7.5. We focused on cluster solutions where the phase differences between adjacent spiking neurons were identical, $\psi_i = \psi$. In the network extension, we assumed that the system satisfied periodic boundary conditions, obtained through a symmetric and circulant form of coupling (see Eq. 5.3). In general, the stability trend for the in-phase solutions (full synchrony, $\psi = 0$) was independent of the size of the network, N, and coupling architecture,W, and thus, identical to the two neuron case. For non-trivial solutions ($\psi \neq 0$), the conditions of stability for an $n-$cluster solution, in a network with nearest neighbours or globally *homogeneous* coupling, depend only on the phase difference (ψ) or the number of clusters (n) respectively. When we introduce a globally monotonic heterogeneity in the synaptic weights, the conditions guaranteeing the

stability of a symmetric cluster solution, depend on *both* ψ and N.

For *low levels of acetylcholine* ($g_M = 5$), our results showed a significant difference in the number of stable cluster solutions with the *type of coupling* (different k and p) that was adopted by the network. When acetylcholine is 'low' ($g_M = 5$), networks, equipped with arbitrary circulant coupling architectures, could synchronize. As the number of excitatory connections decrease $\left(k : \lfloor \frac{N}{2} \rfloor \to 1\right)$, the network exhibits multistablity, marked by an increase in the number of stable symmetric cluster solutions, while still having the ability to synchronize. A similar trend is seen, in which the same number of excitatory connections are maintained $\left(k = \lfloor \frac{N}{2} \rfloor\right)$, but the coupling is changed from a globally homogeneous ($p = 1$) to a distance-dependent type ($p = 0.5$). Essentially, this means that for a given set of initial membrane voltages, depending on the coupling architecture, the network can either approach a non-trivial cluster solution $\left(k = 1 \text{ or } k = \lfloor \frac{N}{2} \rfloor \text{ and } p = 0.5\right)$ or it will fully synchronize $\left(k = \lfloor \frac{N}{2} \rfloor, p = 1\right)$. This presents the network with a mechanism to switch between neural assemblies, brought about by *changes to the number and/or strength of excitatory synaptic connections* under *low levels of ACh*. For example, consider a network, under low levels of ACh, equipped with a nearest neighbours or distance dependent coupling, initialized at a non-trivial cluster solution ($\psi \neq 0$). For the same set of initial conditions, the corresponding network will synchronize with all-to-all homogeneous excitatory coupling. According to [58, 61, 73, 114, 43], low levels of ACh during quiet waking (which follows active waking) and slow wave sleep, may facilitate the consolidation of previously encoded memories, in the CA3 network. In the context of our results, the initial set of membrane voltages could represent a specific stimulus associated with a memory, that is has been encoded into the CA3 network. The network may by default, start out with identical synaptic weights (globally homogeneous coupling), in which every neuron participates in the representation (synchronized network). By modifying the strengths of the synaptic connections in the network (changes to k and p), the same stimulus may be stored efficiently in the form of a unique neural assembly. This presents the network with pathways through which learning can be achieved by changing the the synaptic weights. In the context of slow wave sleep, the idea of the network approaching a default state identified by identical synaptic weights, prior to learning could also be linked to a renormalization hypothesis which is discussed in [40].

The multistability observed (and numerically verified) under low levels of ACh, in a network with nearest neighbour or distance-dependent coupling can be attributed to the heterogeneity in the synaptic weights—an idea that has been discussed in [87, 88, 9]. For each coupling configuration considered, a network initialized in the synchronized ($\psi = 0$) state, can persist under transient perturbations, applied as current pulses, to a subset of the cells. However, networks equipped with heterogeneous coupling (nearest neighbours

or distance-dependent), initially set in a stable non-trivial [2] solution were observed to synchronize in response to these same transient current pulses, applied to a specific number of cells. Additionally, networks with nearest neighbours coupling, initialized in a splay-state solution ($n = N$), could also switch to a different stable $n-$ cluster solution, if a different subset of cells received the current pulses. These results indicate that under low levels of ACh, the network is largely persistent in response to transient changes in the stimuli—consistent with Class II dynamics [74]—although this susceptibility can be modulated by the changes in the coupling, and consistent with the hypothesis outlined in [58, 61]. According to [63, 83, 118], the CA3 network can support the recall of previously learned patterns under low levels of ACh. In particular, CA3 can support a specific type of memory recall, known as *pattern completion* [14]. This has more to do with the fact that the suppression of ACh does not impair memory recall [64, 83]. Incorporating this view into our results may help explain the selective susceptibility observed in networks with heterogeneous connection weights. Suppose the CA3 network is initialized in some non trivial cluster solution, accomplished via heterogeneous connection weights. The set of incoming transient current pulses, simultaneously applied to a subset of the cells in this network, can be interpreted as the transient presentation of partial cue that may trigger the retrieval of the complete memory. As observed in our results, depending on the number of cells stimulated by this pulse, the initialized network may synchronize or switch to a different stable solution. The pulse-induced synchrony can be interpreted as the complete retrieval of the memory. If instead, the network switches to a different stable non-trivial cluster solution, this can be interpreted as an incomplete recovery of the memory. This interpretation also suggests a possible threshold in the number of cells that must be stimulated in the network, in order to retrieve the complete memory, which is a potential feature associated with pattern completion [14]. The stable cluster solution associated with the initialized network, could also represent an efficient neural assembly that was formed during consolidation.

As we *increase the level of ACh in the network* ($g_M : 5 \to 0$), the stability trends become a little complicated. Across all the coupling architectures considered, the network can de-synchronize into multiple stable $n-$cluster solutions. It is generally difficult to find a consistent metric to compare the total number of distinct stable solutions among the three cases. However, we can say for certain that when heterogeneity is introduced into the coupling architecture ($k = 1$ or $k = 1, p = 0.5$), a given network can admit a larger *number of clusters* (n). Although a network with globally homogeneous coupling supports fewer distinct values of n for which the corresponding $n-$cluster solutions are stable, it

[2] In this context, non-trivial solutions are referred to the $n-$cluster solutions outside of the in-phase solutions

may still exhibit a larger number of multiple realizations of the same $n-$cluster. This is due to the lack of constraints on the firing order of the clusters and the flexibility in which cells are recruited into each cluster, which is absent in the case of heterogeneous coupling.

Under high levels of ACh, the CA3 network can exhibit *multistablity* with the *same synaptic weights*. This presents the network with a mechanism to respond to different inputs, which may alter the average network frequency. Traditionally, high levels of ACh observed during active waking or REM sleep, have been linked to the encoding of new memories [61, 63, 60, 64]. In the context of our observations, the multistablity supported by high ACh ($g_M = 0$) may present the CA3 network with a predefined set of distinct patterns (cluster solutions) to choose from, in order to encode different memories. Additionally, the multistablity with the same synaptic weights can also present a mechanism for the network to transition between different cluster states. This was observed in our results, through the application of transient current pulses to a subset of the cells in the network, initialized at a stable cluster solution. In the simulations, the transient current pulse could switch the network to alternate stable cluster solutions. This observation was consistent across all simulations, regardless of network sizes, N, and coupling configuration, W. These results indicate that under high levels of ACh, the network is largely susceptible to transient changes in stimuli—consistent with Class I dynamics [74, 61, 117]—in contrast to the low ACh case. When the M-current is suppressed in the presence of acetylcholine, the behaviour of the CA3 network is primarily driven by recurrent excitation and external current inputs, in the absence of inhibition. This shift in dynamics may enhance the network's responsiveness to incoming signals, allowing it to flexibly encode new information. In particular, this observation may suggest a possible mechanism for *pattern separation*—encoding process primarily involving the dentate gyrus and the CA3, in which pairs of incoming stimuli with subtle differences, are encoded as two distinct representations with a low degree of similarity [92, 37]. In the context of our observations, the initial stable cluster solution may correspond to an activity pattern associated with a stimulus, 'A'. Suppose 'B' is a separate stimulus sharing subtle differences with 'A' . The differences may be conveyed through transient current pulses and subsequently encoded into a distinct $n-$cluster solution following the perturbation. In this interpretation, however, we assume that the stimuli are presented sequentially—'A' is encoded first, followed by 'B'.

As previously mentioned, the multistability can facilitate responses to different inputs, potentially altering the average network frequency. Such input-dependent differences in average frequency were clearly observed in a network of 300 neurons coupled via nearest neighbours, under both low and high levels of ACh. At first glance, the raster plots seemed to suggest a global synchronization among neurons. However, a closer inspection reveals that the network actually breaks up into distinct clusters. More broadly, the

results highlight a contrast in the average network frequency associated with each cluster solution, despite individual neurons maintaining the same spiking frequency under fixed levels of ACh. This provides insight into how individual spiking neurons contribute to the population rhythm through the formation of distinct clusters. In particular, large $n-$cluster solutions may give rise to population rhythms with smaller amplitudes, V_{max}/n, and higher frequencies, nf, where V_{max} and f are the amplitude and frequency associated with trace of the individual neuron.

As we know, different concentrations of ACh, have been associated with different frequency brain rhythms (theta, gamma, delta) emerging during specific physiological states [73, 38, 58]. In the context of our observations, a possible mechanism underlying the emergence of these distinct rhythms may be attributed to cholinergic modulation of the spiking frequency of individual neurons. The multistability observed under high levels of ACh may also make the network more susceptible to entrainment by external input rhythms, in contrast to the reduced susceptibility observed at low ACh levels. This key result is consistent with the hypothesis and computational findings of [117].

Using a phase model approximation, we demonstrated differences in the neural assemblies supported by a network of CA3 pyramidal neurons coupled via weak excitatory AMPA synapses, under varying levels of acetylcholine (ACh) and across three different coupling architectures. Overall, our results indicate that ACh likely plays a role in guiding neural assembly formation within the CA3 network—potentially linking specific assembly patterns to distinct behavioural states, particularly those related to the encoding, consolidation and retrieval of memories, which are hypothesized to occur at different levels of ACh. The stark contrast in the extent of multistability exhibited by the network at high versus low levels of ACh qualitatively supports the findings of [117], which identified two distinct frequency-dependent coding schemes for information processing corresponding to these ACh levels. However, our analysis—primarily exploratory in nature—was restricted to a specific class of solutions in which phase differences between neural oscillators were assumed to be uniform. Consequently, each cluster contained an identical number of neurons, spatially dispersed throughout the network. More complex cluster states may arise outside this assumption, and exploring them could offer a fuller picture of the role of ACh in shaping hippocampal network dynamics. For example, in [87], the authors studied model independent cluster solutions for a ring network equipped with asymmetrical coupling strengths which added more heterogeneity in the network structure, providing a more realistic view on the assembly formation. In [120], the focus was on spatially compact assemblies, where the cells belonging to the same cluster were also located near one another one on the $1-$dimensional ring. However this was suggested as a mechanism appropriate for a network of inhibitory neurons as opposed to one which is excitatory. In this context, it would be worthwhile to

explore such solutions for a network of GABAergic interneurons located within the CA3 region, which also contain an M-current. Additionally, our analysis also assumes specific periodic conditions which restrict the model neurons to the $1-$dimensional ring. Another possible next step could involve extending our analysis to $2-$dimensional networks, similar to the approach taken in [98], but in an acetylcholine-specific context.

One of the limitations in our neuron model, is the assumption that the only effect of acetylcholine at the cellular level is to down regulate the M-current. Acetylcholine also suppresses a calcium activated potassium current, I_{AHP} [3] [93] and the leak current, I_L [126]. Since neither current contribute to the switch in the neural class excitability, they were not considered in our analysis. In [4], it is shown that the simultaneous down-regulation of the leak and M-current would increase the value of g_M at which the excitability switch will occur. In our analysis, this may change $\hat{g}_M$ (See Table 7.2) to be larger than 0.03 (See Figure 6.3). This in turn, potentially creates a broader range of g_M, for which the corresponding network can exhibit multistability and an increased sensitivity to external inputs. We leave this exploration along with the effect of I_{AHP} current for future work.

Our analysis did not address the biophysical implications of intermediate ACh levels ($g_M = 2$). Previous studies [116], suggest that at these intermediate levels, the CA3 network exhibits travelling wave dynamics sensitive to input heterogeneities and may integrate both new and existing activity patterns. Exploring this intermediate acetylcholine regime is also left for future work.

One caveat of a phase model approximation is that it requires that the neurons are intrinsically oscillating and coupled via sufficiently weak synapses. To satisfy this condition, we incorporated a constant external current, I_{app}, into the model neuron, that was large enough to ensure intrinsic oscillations for all values of g_M between 0 and 5. However, this approach resulted in neurons firing at high frequencies—exceeding 500 Hz when g_M was set to 0—which is beyond the typical biophysical range associated with observed brain rhythms. To model more realistic firing rates, one possible approach would be to restrict the range of g_M and choose a smaller applied current. Alternatively, the applied current could be adjusted depending on the g_M value to maintain a fixed firing frequency or include inhibitory neurons in the network. The latter approach has been considered in [117], with a computational model. Another limitation of the phase model analysis is the reduced accuracy near possible critical transition points. In particular, the phase model predicted the synchrony of the pyramidal neurons would begin exactly around $g_M = 3.13$, a result that was not verified in our simulations. As argued in [106], a more detailed Fourier representation may be necessary for accurately analyzing networks with all-to-

[3] AHP here stands for afterhyperpolarization.

all coupling—an issue also observed in our results for the globally homogeneous case. While the assumption of weak coupling is not entirely biophysically unrealistic, a valuable direction could be to examine the persistence of these model predictions under stronger coupling conditions, particularly comparing behaviours under low versus high ACh levels. Finally, applying a phase model analysis to inhibitory interneuron networks incorporating the M-current could reveal whether their synchrony dynamics align with the numerical findings observed in pairs of inhibitory neurons, as reported in [4]. A further extension could then involve deriving a phase model for a mixed excitatory-inhibitory network and analyzing the corresponding cluster solutions [36], providing a more biophysically realistic model of the CA3 network.

In spite of its limitations, the phase model approach remains a powerful and insightful tool for analyzing synchrony in neuronal networks. It enables the reduction of high dimensional biophysical systems to simpler mathematical models, facilitating a systematic approach to the investigation of neural synchrony, under varying physiological conditions, such as different levels of acetylcholine.

References

[1] findpeaks. Available online at: https://www.mathworks.com/help/signal/ref/findpeaks.html, last accessed on 2025-04-20.

[2] ode23. Available online at: https://www.mathworks.com/help/matlab/ref/ode23.html, last accessed on 2025-03-25.

[3] XPP TUTORIAL IV. Available online at: https://sites.pitt.edu/~phase/bard/bardware/tut/xpptut4.html#average, last accessed on 2025-05-24.

[4] I. Al-Darabsah and S. A. Campbell. M-current induced Bogdanov–Takens bifurcation and switching of neuron excitability class. *The Journal of Mathematical Neuroscience*, 11(1):5, Feb. 2021.

[5] R. W. Aldrich, P. A. Getting, and S. H. Thompson. Inactivation of delayed outward current in molluscan neurone somata. *The Journal of Physiology*, 291:507–530, June 1979.

[6] P. Ashwin and J. W. Swift. The dynamics ofn weakly coupled identical oscillators. *Journal of Nonlinear Science*, 2(1):69–108, Mar. 1992.

[7] R. Bianchi and R. K. Wong. Carbachol-induced synchronized rhythmic bursts in CA3 neurons of guinea pig hippocampus in vitro. *Journal of Neurophysiology*, 72(1):131–138, July 1994.

[8] B. H. Bland, L. V. Colom, J. Konopacki, and S. H. Roth. Intracellular records of carbachol-induced theta rhythm in hippocampal slices. *Brain Research*, 447(2):364–368, May 1988.

[9] A. Bogaard, J. Parent, M. Zochowski, and V. Booth. Interaction of cellular and network mechanisms in spatiotemporal pattern formation in neuronal networks. *Journal of Neuroscience*, 29(6):1677–1687, 2009. Publisher: Soc Neuroscience.

[10] R. Boyce, S. D. Glasgow, S. Williams, and A. Adamantidis. Causal evidence for the role of REM sleep theta rhythm in contextual memory consolidation. *Science*, 352(6287):812–816, May 2016.

[11] R. Brette. What Is the Most Realistic Single-Compartment Model of Spike Initiation? *PLoS Computational Biology*, 11(4):e1004114, Apr. 2015.

[12] D. A. Brown and G. M. Passmore. Neural KCNQ (Kv7) channels. *British Journal of Pharmacology*, 156(8):1185–1195, Apr. 2009.

[13] G. Buzsáki. Theta oscillations in the hippocampus. *Neuron*, 33(3):325–340, Jan. 2002.

[14] J. H. Byrne, R. Heidelberger, and M. N. Waxham. *From Molecules to Networks: an Introduction to Cellular and Molecular Neuroscience*. Academic Press, 2014.

[15] S. A. Campbell and Z. Wang. Phase models and clustering in networks of oscillators with delayed coupling. *Physica D: Nonlinear Phenomena*, 363:44–55, Jan. 2018.

[16] S. Charpak, B. H. Gähwiler, K. Q. Do, and T. Knöpfel. Potassium conductances in hippocampal neurons blocked by excitatory amino-acid transmitters. *Nature*, 347(6295):765–767, Oct. 1990.

[17] K. S. Cole and A. L. Hodgkin. MEMBRANE AND PROTOPLASM RESISTANCE IN THE SQUID GIANT AXON. *The Journal of General Physiology*, 22(5):671–687, May 1939.

[18] M. Cole, M. D. Winkelman, J. C. Morris, J. E. Simon, and T. A. Boyd. Thalamic amnesia: Korsakoff syndrome due to left thalamic infarction. *Journal of the Neurological Sciences*, 110(1):62–67, July 1992.

[19] L. L. Colgin and E. I. Moser. Gamma oscillations in the hippocampus. *Physiology (Bethesda, Md.)*, 25(5):319–329, Oct. 2010.

[20] S. M. Crook, G. B. Ermentrout, and J. M. Bower. Spike frequency adaptation affects the synchronization properties of networks of cortical oscillations. *Neural Computation*, 10(4):837–854, May 1998.

[21] S. M. Crook, G. B. Ermentrout, M. C. Vanier, and J. M. Bower. The role of axonal delay in the synchronization of networks of coupled cortical oscillators. *Journal of Computational Neuroscience*, 4(2):161–172, Apr. 1997.

[22] P. Dayan and L. F. Abbott. *Theoretical Neuroscience: Computational and Mathematical Modeling of Neural Systems*. MIT press, 2005.

[23] T. Demiralp, C. Başar-Eroglu, and E. Başar. Distributed gamma band responses in the brain studied in cortex, reticular formation, hippocampus and cerebellum. *The International Journal of Neuroscience*, 84(1-4):1–13, Feb. 1996.

[24] A. Destexhe, Z. F. Mainen, and T. J. Sejnowski. Synthesis of models for excitable membranes, synaptic transmission and neuromodulation using a common kinetic formalism. *Journal of Computational Neuroscience*, 1(3):195–230, Aug. 1994.

[25] C. O. Diekman and D. B. Forger. Clustering predicted by an electrophysiological model of the suprachiasmatic nucleus. *Journal of Biological Rhythms*, 24(4):322–333, Aug. 2009.

[26] J. E. Dowling. *Neurons and Networks: an Introduction to Behavioral Neuroscience*. Harvard University Press, 2001.

[27] G. Dragoi and G. Buzsáki. Temporal Encoding of Place Sequences by Hippocampal Cell Assemblies. *Neuron*, 50(1):145–157, Apr. 2006.

[28] P. Dutar and R. A. Nicoll. Classification of muscarinic responses in hippocampus in terms of receptor subtypes and second-messenger systems: electrophysiological studies in vitro. *The Journal of Neuroscience: The Official Journal of the Society for Neuroscience*, 8(11):4214–4224, Nov. 1988.

[29] B. Ermentrout. Type I Membranes, Phase Resetting Curves, and Synchrony. *Neural Computation*, 8(5):979–1001, July 1996.

[30] B. Ermentrout. Simulating, analyzing, and animating dynamical systems: A guide to Xppaut for researchers and students (software, environments, tools). *Philadelphia: Society for Industrial and Applied Mathematics*, 2002.

[31] B. Ermentrout, M. Pascal, and B. Gutkin. The effects of spike frequency adaptation and negative feedback on the synchronization of neural oscillators. *Neural Computation*, 13(6):1285–1310, 2001. Publisher: MIT Press.

[32] G. B. Ermentrout, R. F. Galán, and N. N. Urban. Relating Neural Dynamics to Neural Coding. *Phys. Rev. Lett.*, 99(24):248103, Dec. 2007. Publisher: American Physical Society.

[33] G. B. Ermentrout and N. Kopell. Frequency plateaus in a chain of weakly coupled oscillators, I. *SIAM Journal on Mathematical Analysis*, 15(2):215–237, 1984. Publisher: SIAM.

[34] G. B. Ermentrout and N. Kopell. Fine structure of neural spiking and synchronization in the presence of conduction delays. *Proceedings of the National Academy of Sciences*, 95(3):1259–1264, 1998. Publisher: The National Academy of Sciences.

[35] G. B. Ermentrout and N. Kopell. Frequency Plateaus in a Chain of Weakly Coupled Oscillators, I. *SIAM Journal on Mathematical Analysis*, July 2006. Publisher: Society for Industrial and Applied Mathematics.

[36] G. B. Ermentrout and D. H. Terman. *Mathematical Foundations of Neuroscience*, volume 35 of *Interdisciplinary Applied Mathematics*. Springer, New York, NY, 2010.

[37] F. Faghihi and A. A. Moustafa. A computational model of pattern separation efficiency in the dentate gyrus with implications in schizophrenia. *Frontiers in Systems Neuroscience*, 9:42, 2015. Publisher: Frontiers Media SA.

[38] J. M. Fellous and T. J. Sejnowski. Cholinergic induction of oscillations in the hippocampal slice in the slow (0.5-2 Hz), theta (5-12 Hz), and gamma (35-70 Hz) bands. *Hippocampus*, 10(2):187–197, 2000.

[39] C. G. Fink, V. Booth, and M. Zochowski. Cellularly-Driven Differences in Network Synchronization Propensity Are Differentially Modulated by Firing Frequency. *PLoS Computational Biology*, 7(5):e1002062, May 2011.

[40] C. G. Fink, G. G. Murphy, M. Zochowski, and V. Booth. A dynamical role for acetylcholine in synaptic renormalization. *PLoS Computational Biology*, 9(3):e1002939, 2013. Publisher: Public Library of Science San Francisco, USA.

[41] A. Fisahn, F. G. Pike, E. H. Buhl, and O. Paulsen. Cholinergic induction of network oscillations at 40 Hz in the hippocampus in vitro. *Nature*, 394(6689):186–189, July 1998. Publisher: Nature Publishing Group.

[42] H. R. Friedman and P. S. Goldman-Rakic. Activation of the hippocampus and dentate gyrus by working-memory: a 2-deoxyglucose study of behaving rhesus monkeys. *The Journal of Neuroscience: The Official Journal of the Society for Neuroscience*, 8(12):4693–4706, Dec. 1988.

[43] S. Gais and J. Born. Low acetylcholine during slow-wave sleep is critical for declarative memory consolidation. *Proceedings of the National Academy of Sciences*, 101(7):2140–2144, 2004. Publisher: National Academy of Sciences.

[44] R. F. Galán. The Phase Oscillator Approximation in Neuroscience: An Analytical Framework to Study Coherent Activity in Neural Networks. In J. L. P. Velazquez and R. Wennberg, editors, *Coordinated Activity in the Brain: Measurements and Relevance to Brain Function and Behavior*, pages 65–89. Springer, New York, NY, 2009.

[45] R. F. Galán, G. B. Ermentrout, and N. N. Urban. Efficient Estimation of Phase-Resetting Curves in Real Neurons and its Significance for Neural-Network Modeling. *Phys. Rev. Lett.*, 94(15):158101, Apr. 2005. Publisher: American Physical Society.

[46] R. F. Galán, G. B. Ermentrout, and N. N. Urban. Predicting synchronized neural assemblies from experimentally estimated phase-resetting curves. *Neurocomputing*, 69(10):1112–1115, 2006.

[47] M. Ghoneim and S. Mewaldt. Effects of diazepam and scopolamine on storage, retrieval and organizational processes in memory. *Psychopharmacologia*, 44:257–262, 1975. Publisher: Springer.

[48] P. E. Gilbert and A. M. Brushfield. The Role of the CA3 Hippocampal Subregion in Spatial Memory: A Process Oriented Behavioral Assessment. *Progress in Neuro-Psychopharmacology & Biological Psychiatry*, 33(5):774–781, Aug. 2009.

[49] P. E. Gilbert, R. P. Kesner, and I. Lee. Dissociating hippocampal subregions: double dissociation between dentate gyrus and CA1. *Hippocampus*, 11(6):626–636, 2001.

[50] A. E. Gold and R. P. Kesner. The role of the CA3 subregion of the dorsal hippocampus in spatial pattern completion in the rat. *Hippocampus*, 15(6):808–814, 2005.

[51] D. Golomb and D. Hansel. The number of synaptic inputs and the synchrony of large, sparse neuronal networks. *Neural Computation*, 12(5):1095–1139, May 2000.

[52] R. M. Gray. Toeplitz and Circulant Matrices: A Review. *Foundations and Trends® in Communications and Information Theory*, 2(3):155–239, Jan. 2006.

[53] J. Haam and J. L. Yakel. Cholinergic modulation of the hippocampal region and memory function. *Journal of Neurochemistry*, 142(Suppl 2):111–121, Aug. 2017.

[54] J. V. Halliwell. M-current in human neocortical neurones. *Neuroscience Letters*, 67(1):1–6, June 1986.

[55] J. V. Halliwell and P. R. Adams. Voltage-clamp analysis of muscarinic excitation in hippocampal neurons. *Brain Research*, 250(1):71–92, Oct. 1982.

[56] D. Hansel, G. Mato, and C. Meunier. Synchrony in excitatory neural networks. *Neural Computation*, 7(2):307–337, Mar. 1995.

[57] K. D. Harris, J. Csicsvari, H. Hirase, G. Dragoi, and G. Buzsáki. Organization of cell assemblies in the hippocampus. *Nature*, 424(6948):552–556, 2003. Publisher: Nature Publishing Group UK London.

[58] M. E. Hasselmo. Neuromodulation: acetylcholine and memory consolidation. *Trends in Cognitive Sciences*, 3(9):351–359, Sept. 1999.

[59] M. E. Hasselmo, B. P. Anderson, and J. M. Bower. Cholinergic modulation of cortical associative memory function. *Journal of Neurophysiology*, 67(5):1230–1246, 1992. Publisher: American Physiological Society Bethesda, MD.

[60] M. E. Hasselmo and J. McGaughy. High acetylcholine levels set circuit dynamics for attention and encoding and low acetylcholine levels set dynamics for consolidation. In *Progress in Brain Research*, volume 145 of *Acetylcholine in the Cerebral Cortex*, pages 207–231. Elsevier, Jan. 2004.

[61] M. E. Hasselmo and M. Sarter. Modes and models of forebrain cholinergic neuromodulation of cognition. *Neuropsychopharmacology: Official Publication of the American College of Neuropsychopharmacology*, 36(1):52–73, Jan. 2011.

[62] M. E. Hasselmo and E. Schnell. Laminar selectivity of the cholinergic suppression of synaptic transmission in rat hippocampal region CA1: computational modeling and brain slice physiology. *The Journal of Neuroscience: The Official Journal of the Society for Neuroscience*, 14(6):3898–3914, June 1994.

[63] M. E. Hasselmo, E. Schnell, and E. Barkai. Dynamics of learning and recall at excitatory recurrent synapses and cholinergic modulation in rat hippocampal region CA3. *The Journal of Neuroscience: The Official Journal of the Society for Neuroscience*, 15(7 Pt 2):5249–5262, July 1995.

[64] M. E. Hasselmo, B. P. Wyble, and G. V. Wallenstein. Encoding and retrieval of episodic memories: role of cholinergic and GABAergic modulation in the hippocampus. *Hippocampus*, 6(6):693–708, 1996.

[65] V. Hedges. *Introduction to Neuroscience*. Michigan State University, 2022.

[66] A. L. Hodgkin. The local electric changes associated with repetitive action in a non-medullated axon. *The Journal of Physiology*, 107(2):165–181, Mar. 1948.

[67] A. L. Hodgkin and A. F. Huxley. The components of membrane conductance in the giant axon of Loligo. *The Journal of Physiology*, 116(4):473–496, Apr. 1952.

[68] A. L. Hodgkin and A. F. Huxley. Currents carried by sodium and potassium ions through the membrane of the giant axon of Loligo. *The Journal of Physiology*, 116(4):449–472, Apr. 1952.

[69] A. L. Hodgkin and A. F. Huxley. The dual effect of membrane potential on sodium conductance in the giant axon of Loligo. *The Journal of Physiology*, 116(4):497–506, Apr. 1952.

[70] A. L. Hodgkin and A. F. Huxley. A quantitative description of membrane current and its application to conduction and excitation in nerve. *The Journal of Physiology*, 117(4):500–544, Aug. 1952.

[71] F. C. Hoppensteadt and E. M. Izhikevich. *Weakly Connected Neural Networks*, volume 126 of *Applied Mathematical Sciences*. Springer, New York, NY, 1997.

[72] H. Hu, K. Vervaeke, and J. F. Storm. Two forms of electrical resonance at theta frequencies, generated by M-current, h-current and persistent Na+ current in rat hippocampal pyramidal cells. *The Journal of Physiology*, 545(3):783–805, Dec. 2002.

[73] Q. Huang, C. Liao, F. Ge, J. Ao, and T. Liu. Acetylcholine bidirectionally regulates learning and memory. *Journal of Neurorestoratology*, 10(2):100002, June 2022.

[74] E. M. Izhikevich. *Dynamical systems in neuroscience: the geometry of excitability and bursting*. Computational neuroscience. MIT Press, Cambridge, Mass, 2007. OCLC: ocm65400606.

[75] D. Johnston. Passive cable properties of hippocampal CA3 pyramidal neurons. *Cellular and Molecular Neurobiology*, 1(1):41–55, Mar. 1981.

[76] D. Johnston, J. J. Hablitz, and W. A. Wilson. Voltage clamp discloses slow inward current in hippocampal burst-firing neurones. *Nature*, 286(5771):391–393, July 1980.

[77] E. R. Kandel, J. H. Schwartz, T. M. Jessell, S. Siegelbaum, A. J. Hudspeth, S. Mack, and others. *Principles of Neural Science*, volume 4. McGraw-hill New York, 2000.

[78] K. M. Kerr, K. L. Agster, S. C. Furtak, and R. D. Burwell. Functional neuroanatomy of the parahippocampal region: the lateral and medial entorhinal areas. *Hippocampus*, 17(9):697–708, 2007.

[79] C. A. Kitt, C. Höhmann, J. T. Coyle, and D. L. Price. Cholinergic innervation of mouse forebrain structures. *The Journal of Comparative Neurology*, 341(1):117–129, Mar. 1994.

[80] S. Knudstrup, M. Zochowski, and V. Booth. Network burst dynamics under heterogeneous cholinergic modulation of neural firing properties and heterogeneous synaptic connectivity. *European Journal of Neuroscience*, 43(10):1321–1339, 2016. Publisher: Wiley Online Library.

[81] N. Kopell, G. B. Ermentrout, M. A. Whittington, and R. D. Traub. Gamma rhythms and beta rhythms have different synchronization properties. *Proceedings of the National Academy of Sciences of the United States of America*, 97(4):1867–1872, Feb. 2000.

[82] E. Kreyszig. *Introductory Functional Analysis with Applications*. John Wiley & Sons, Jan. 1991. Google-Books-ID: AQtMEAAAQBAJ.

[83] J. Kukolja, C. M. Thiel, and G. R. Fink. Cholinergic stimulation enhances neural activity associated with encoding but reduces neural activity associated with retrieval in humans. *Journal of Neuroscience*, 29(25):8119–8128, 2009. Publisher: Society for Neuroscience.

[84] Y. Kuramoto. Chemical Turbulence. In Y. Kuramoto, editor, *Chemical Oscillations, Waves, and Turbulence*, pages 111–140. Springer, Berlin, Heidelberg, 1984.

[85] J. M. Lassalle, T. Bataille, and H. Halley. Reversible inactivation of the hippocampal mossy fiber synapses in mice impairs spatial learning, but neither consolidation nor memory retrieval, in the Morris navigation task. *Neurobiology of Learning and Memory*, 73(3):243–257, May 2000.

[86] I. Lee and R. P. Kesner. Encoding versus retrieval of spatial memory: double dissociation between the dentate gyrus and the perforant path inputs into CA3 in the dorsal hippocampus. *Hippocampus*, 14(1):66–76, 2004.

[87] Y.-X. Li. Clustering in neural networks with heterogeneous and asymmetrical coupling strengths. *Physica D: Nonlinear Phenomena*, 180(3-4):210–234, 2003. Publisher: Elsevier.

[88] Y.-X. Li, Y.-q. Wang, and R. Miura. Clustering in small networks of excitatory neurons with heterogeneous coupling strengths. *Journal of Computational Neuroscience*, 14:139–159, 2003. Publisher: Springer.

[89] Y. Lu, M. Sarter, M. Zochowski, and V. Booth. Phasic cholinergic signaling promotes emergence of local gamma rhythms in excitatory–inhibitory networks. *European Journal of Neuroscience*, 52(6):3545–3560, 2020. Publisher: Wiley Online Library.

[90] L. Luo. *Principles of Neurobiology*. Garland Science, Sept. 2020. Google-Books-ID: r576DwAAQBAJ.

[91] A. Lysakowski, B. H. Wainer, G. Bruce, and L. B. Hersh. An atlas of the regional and laminar distribution of choline acetyltransferase immunoreactivity in rat cerebral cortex. *Neuroscience*, 28(2):291–336, 1989.

[92] A. D. Madar, L. A. Ewell, and M. V. Jones. Pattern separation of spiketrains in hippocampal neurons. *Scientific Reports*, 9(1):5282, 2019. Publisher: Nature Publishing Group UK London.

[93] D. V. Madison, B. Lancaster, and R. A. Nicoll. Voltage clamp analysis of cholinergic action in the hippocampus. *Journal of Neuroscience*, 7(3):733–741, Mar. 1987.

[94] I. G. Malkin. Methods of Poincare and Liapunov in theory of non-linear oscillations. *Gostexizdat, Moscow*, 1949.

[95] I. G. Malkin. Some problems of the theory of nonlinear oscillations,(Russian) Gosudarstv. *Izdat. Tehn.-Teor. Lit., Moscow*, 1956.

[96] S. Mewaldt and M. Ghoneim. The effects and interactions of scopolamine, physostigmine and methamphetamine on human memory. *Pharmacology Biochemistry and Behavior*, 10(2):205–210, 1979. Publisher: Elsevier.

[97] J. Miller, H. Ryu, Z. Teymuroglu, X. Wang, V. Booth, and S. A. Campbell. Clustering in Inhibitory Neural Networks with Nearest Neighbor Coupling. In T. Jackson and A. Radunskaya, editors, *Applications of Dynamical Systems in Biology and Medicine*, pages 99–121, New York, NY, 2015. Springer.

[98] J. Miller, H. Ryu, X. Wang, V. Booth, and S. A. Campbell. Patterns of synchronization in 2D networks of inhibitory neurons. *Frontiers in Computational Neuroscience*, 16:903883, 2022. Publisher: Frontiers Media SA.

[99] M. Mishkin. Memory in monkeys severely impaired by combined but not by separate removal of amygdala and hippocampus. *Nature*, 273(5660):297–298, 1978.

[100] G. Mm and M. Sp. Studies on human memory: the interactions of diazepam, scopolamine, and physostigmine. *Psychopharmacology*, 52(1), Mar. 1977. Publisher: Psychopharmacology (Berl).

[101] R. Morris, D. G. Amaral, T. Bliss, K. Duff, and J. O'Keefe. *The Hippocampus Book*. Oxford university press, 2024.

[102] P. Munkres and others. Introduction to Topology. 2005. Publisher: MIT Course Number.

[103] L. Nadel, J. Willner, and E. M. Kurz. Cognitive Maps and Environmental Context. In *Context and Learning*. Psychology Press, 1985. Num Pages: 22.

[104] E. Nyhus and T. Curran. Functional role of gamma and theta oscillations in episodic memory. *Neuroscience & Biobehavioral Reviews*, 34(7):1023–1035, 2010.

[105] J. O'keefe and L. Nadel. Précis of O'Keefe & Nadel's The hippocampus as a cognitive map. *Behavioral and Brain Sciences*, 2(4):487–494, 1979. Publisher: Cambridge University Press.

[106] K. Okuda. Variety and generality of clustering in globally coupled oscillators. *Physica D: Nonlinear Phenomena*, 63(3):424–436, Mar. 1993.

[107] D. Olton, C. Wible, K. Pang, and Y. Sakurai. Hippocampal cells have mnemonic correlates as well as spatial ones. *Psychobiology*, 17:228–229, Sept. 2013.

[108] M. S. Olufsen, M. A. Whittington, M. Camperi, and N. Kopell. New roles for the gamma rhythm: population tuning and preprocessing for the Beta rhythm. *Journal of Computational Neuroscience*, 14(1):33–54, 2003.

[109] R. C. O'Reilly and J. L. McClelland. Hippocampal conjunctive encoding, storage, and recall: avoiding a trade-off. *Hippocampus*, 4(6):661–682, Dec. 1994.

[110] E. Pastalkova, V. Itskov, A. Amarasingham, and G. Buzsáki. Internally generated cell assembly sequences in the rat hippocampus. *Science (New York, N.Y.)*, 321(5894):1322–1327, Sept. 2008.

[111] L. Perko. *Differential Equations and Dynamical Systems*, volume 7. Springer Science & Business Media, 2013.

[112] M. R. Picciotto, M. J. Higley, and Y. S. Mineur. Acetylcholine as a neuromodulator: cholinergic signaling shapes nervous system function and behavior. *Neuron*, 76(1):116–129, Oct. 2012.

[113] P. F. Pinsky and J. Rinzel. Intrinsic and network rhythmogenesis in a reduced traub model for CA3 neurons. *Journal of Computational Neuroscience*, 1(1):39–60, June 1994.

[114] B. H. Rasch, J. Born, and S. Gais. Combined blockade of cholinergic receptors shifts the brain from stimulus encoding to memory consolidation. *Journal of Cognitive Neuroscience*, 18(5):793–802, 2006. Publisher: MIT Press.

[115] J. Rinzel and G. B. Ermentrout. Analysis of neural excitability and oscillations. *Methods in Neuronal Modeling*, 2:251–292, 1998. Publisher: MIT press Cambridge, MA.

[116] J. P. Roach, E. Ben-Jacob, L. M. Sander, and M. R. Zochowski. Formation and dynamics of waves in a cortical model of cholinergic modulation. *PLoS Computational Biology*, 11(8):e1004449, 2015. Publisher: Public Library of Science San Francisco, CA USA.

[117] J. P. Roach, B. Eniwaye, V. Booth, L. M. Sander, and M. R. Zochowski. Acetylcholine mediates dynamic switching between information coding schemes in neuronal networks. *Frontiers in Systems Neuroscience*, 13:64, 2019. Publisher: Frontiers Media SA.

[118] J. P. Roach, L. M. Sander, and M. R. Zochowski. Memory recall and spike-frequency adaptation. *Physical Review E*, 93(5):052307, 2016. Publisher: APS.

[119] E. T. Rolls. A theory of hippocampal function in memory. *Hippocampus*, 6(6):601–620, 1996.

[120] H. Ryu, J. Miller, Z. Teymuroglu, X. Wang, V. Booth, and S. A. Campbell. Spatially localized cluster solutions in inhibitory neural networks. *Mathematical Biosciences*, 336:108591, 2021. Publisher: Elsevier.

[121] Y. Sakurai. Hippocampal and neocortical cell assemblies encode memory processes for different types of stimuli in the rat. *Journal of Neuroscience*, 16(8):2809–2819, Apr. 1996.

[122] W. B. Scoville and B. Milner. LOSS OF RECENT MEMORY AFTER BILATERAL HIPPOCAMPAL LESIONS. *Journal of Neurology, Neurosurgery, and Psychiatry*, 20(1):11–21, Feb. 1957.

[123] R. Siciliano. The hodgkin-huxley model. *Its Extensions, Analysis and Numerics*, 2012.

[124] L. R. Squire. Memory and the hippocampus: A synthesis from findings with rats, monkeys, and humans. *Psychological Review*, 99(2):195–231, 1992.

[125] K. Stiefel, B. Gutkin, and T. Sejnowski. Cholinergic modulation of spike generating dynamics in cortical pyramidal neurons. In *Society for Neuroscience Abstract*, volume 29, 2003.

[126] K. M. Stiefel, B. S. Gutkin, and T. J. Sejnowski. Cholinergic Neuromodulation Changes Phase Response Curve Shape and Type in Cortical Pyramidal Neurons. *PLOS ONE*, 3(12):e3947, Dec. 2008. Publisher: Public Library of Science.

[127] K. M. Stiefel, B. S. Gutkin, and T. J. Sejnowski. The effects of cholinergic neuromodulation on neuronal phase-response curves of modeled cortical neurons. *Journal of Computational Neuroscience*, 26(2):289–301, Apr. 2009.

[128] D. W. Straughan. Neurotransmitters and the Hippocampus. In R. L. Isaacson and K. H. Pribram, editors, *The Hippocampus: Volume 1: Structure and Development*, pages 239–268. Springer US, Boston, MA, 1975.

[129] S. H. Strogatz. *Nonlinear Dynamics and Chaos: with Applications to Physics, Biology, Chemistry, and Engineering (Studies in Nonlinearity)*, volume 1. Westview press, 2001.

[130] R. D. Traub. Repetitive firing of Renshaw spinal interneurons. *Biological Cybernetics*, June 1977.

[131] R. D. Traub. Simulation of intrinsic bursting in CA3 hippocampal neurons. *Neuroscience*, 7(5):1233–1242, May 1982.

[132] R. D. Traub and R. Miles. *Neuronal Networks of the Hippocampus*. Cambridge University Press, Cambridge, 1991.

[133] C. H. Vanderwolf. Hippocampal electrical activity and voluntary movement in the rat. *Electroencephalography and Clinical Neurophysiology*, 26(4):407–418, Apr. 1969.

[134] Z. Wang and S. A. Campbell. Phase models and clustering in networks of oscillators with delayed, all-to-all coupling. *IFAC-PapersOnLine*, 48(12):105–110, Jan. 2015.

[135] J. H. Williams and J. A. Kauer. Properties of carbachol-induced oscillatory activity in rat hippocampus. *Journal of Neurophysiology*, 78(5):2631–2640, Nov. 1997.

[136] A. T. Winfree. *The Geometry of Biological Time*, volume 2. Springer, 1980.

[137] Y. Zhou, T. Vo, H. G. Rotstein, M. M. McCarthy, and N. Kopell. M-Current Expands the Range of Gamma Frequency Inputs to Which a Neuronal Target Entrains. *The Journal of Mathematical Neuroscience*, 8(1):13, Dec. 2018.

APPENDICES

Appendix A

Appendix for Chapter 3

Faraday's Constant (F) : 9.648×10^4 C.mol^{-1}
Ideal Gas Constant (R) : 8.3145 J mol^{-1} K^{-1}

Bogdanov Takens Bifurcation

It is a co-dimension two bifurcation, associated with an equilibrium point that has a zero eigenvalue with algebriac multiplicity two and geometric multiplicity one.

Cusp Bifurcation

When three stable equilibirum points coalesce into one.

Appendix B

Appendix for Chapter 4

Theorem B.0.1. ***Fredholm Alternative****[82]. Suppose that*

$$\mathcal{L}x = \frac{dx}{dt} + A(t)x = f(t) : x \in \mathbb{R}^N \tag{B.1}$$

where the matrix $A(t)$ and the vector function $f(t)$ are continuous and T-periodic. Then there is a continuous T-periodic solution $x(t)$ to (B.1) if an only if

$$\frac{1}{T}\int_0^T Z(t) \cdot f(t)dt = 0 \tag{B.2}$$

for each T-periodic solution $Z(t)$ to the adjoint problem to (B.1)

$$\mathcal{L}^* x = -\frac{dZ}{dt} + \{A(t)\}^T Z = 0 \tag{B.3}$$

where $\{A(t)^T\}$ is the transpose of the matrix $A(t)$.

Appendix C

Appendix for Chapter 7

C.1 How to determine the firing order of cluster solutions

Consider a symmetric $n-$cluster solution corresponding to a network of N model neurons as described in Chapter 5. Recall that the cells in the network are arranged along a one-dimensional ring satisfying periodic boundary conditions (5.5). In the phase model reduction, each cell,i, maybe described by its phase θ_i. Assume that phase differences between adjacent cells, ψ_i, are all identical, ψ.

The idea is to create a mapping from θ_i to $[0, 2\pi)$ at fixed time t, once the network has settled into its $n-$cluster solution. By default we assign θ_1 to 0, and then depending on ψ and N, the remaining oscillators,θ_i, will be assigned the following values.

$$\theta_i = (i-1)\cdot\psi\cdot \pmod{2\pi} \tag{C.1}$$

Applying Eq. C.1 to the network exhibiting a symmetric cluster solution, we see that if θ_i and θ_j map to the same phase, then they will belong to the same cluster, that is, their phase difference, $\theta_j - \theta_i$, is 0. The firing order can be determined by arranging the oscillators in increasing order of their corresponding mappings in Eq. C.1.

As an example, consider the splay solution for network of 4 cells. For a symmetric cluster, there are two possible equilibrium points, ψ, associated with this solution, $\psi = \frac{\pi}{2}$

and $\psi = 3\frac{\pi}{2}$. Applying the algorithm in (C.1) for each one, we find:

$$\textit{For } \psi = \frac{\pi}{2}: \tag{C.2}$$

$$\begin{aligned}\theta_1 &= 0\\ \theta_2 &= \frac{\pi}{2}\\ \theta_3 &= \pi\\ \theta_4 &= 3\frac{\pi}{2}\end{aligned}$$

$$\textit{For } \psi = 3\frac{\pi}{2}: \tag{C.3}$$

$$\begin{aligned}\theta_1 &= 0\\ \theta_2 &= 3\frac{\pi}{2}\\ \theta_3 &= \pi\\ \theta_4 &= \frac{\pi}{2}\end{aligned}$$

Arranging the oscillators, θ_i, in an increasing order of the reassigned values in (C.2) and (C.3), we conclude that the firing order corresponding to $\psi = \frac{\pi}{2}$ is $1-2-3-4$ and for $\psi = 3\frac{\pi}{2}$, is $1-4-3-2$. This is also true for any $4-$cluster solution obtained for a network $N = 4 \cdot k$.

C.2 Numerical computation of interaction function

When we derive the interaction function numerically from XPPAUT, there is no explicit dependence on the M-current conductance parameter g_M. This would mean that we need to manually change this parameter each time we want to compute an interaction function for the neuron under a specific level of influence under the M-current. As a result, we consider a discrete set of g_M values and compute the interaction function for each one as described in Section 7.1.

In the absence of coupling, for a given value of g_M, each neuron in (6.18) has a unique [1] stable limit cycle. The period of the limit cycle for an RTM model neuron at different values of g_M is summarized in C.1.

[1] upto a scalar multiple

M-Current : g_M	Period of oscillations: T
0	2.025
2	3.14
3.13	5.87
5	14.55

Table C.1: Period of the limit cycles exhibited by the RTM model neuron corresponding to different values of g_M

C.2.1 Fourier approximation of interaction function

With the period T measured for each limit cycle solution corresponding to a given value of g_M, we may now derive the interaction function, H. The steps taken to numerically solve the linear adjoint system and consequently derive the corresponding interaction function using XPPAUT are outlined in [3]. On XPPAUT, once we have the interaction function, we can obtain a finite fourier approximation of H. In order to use the function for stability analysis, we utilize a minimum number of terms that best accurately captures the behaviour of the H function. In Figure C.1, we present the Fourier approximations for four different interaction functions associated with $g_M = 0, 2, 3.13$ and 5 respectively.

In order to preserve accuracy and minimize computational difficulty in the approximation of H, we choose a 30-term approximation.

C.3 Appendix for Section 7.3

In Figure C.2 , panel (A) shows a network of 12 neurons, initialized in a stable 4 cluster solution associated with $\psi = \frac{\pi}{2}$ and a firing order of $C_1-C_2-C_3-C_4$. Applying a transient pulse to a subset of the cells can switch the network to a different 4 cluster solution in two ways: I) where the firing order switches from $C_1 - C_2 - C_3 - C_4$ to $C_1 - C_4 - C_2 - C_3$ as illustrated in panel (B) and II) where the cells for cluster C_2 and C_4 change. In particular C_2 changes from $\{2, 6, 10\}$ to $\{2, 10, 12\}$ and C_4 changes from $\{4, 8, 12\}$ to $\{4, 6, 8\}$ as illustrated in panel (C). Similarly, consider a network initialized in a stable $6-$cluster solution with a firing order: $C_1-C_2-C_3-C_4-C_5-C_6$ as shown in panel (D). A transient pulse can alter the firing order of the solution into two arrangements: I) $C_1 - C_6 - C_4 - C_2 - C_5 - C_3$, as shown in panel (E) and II) $C_1 - C_6 - C_2 - C_4 - C_5 - C_3$, as shown in panel (F).

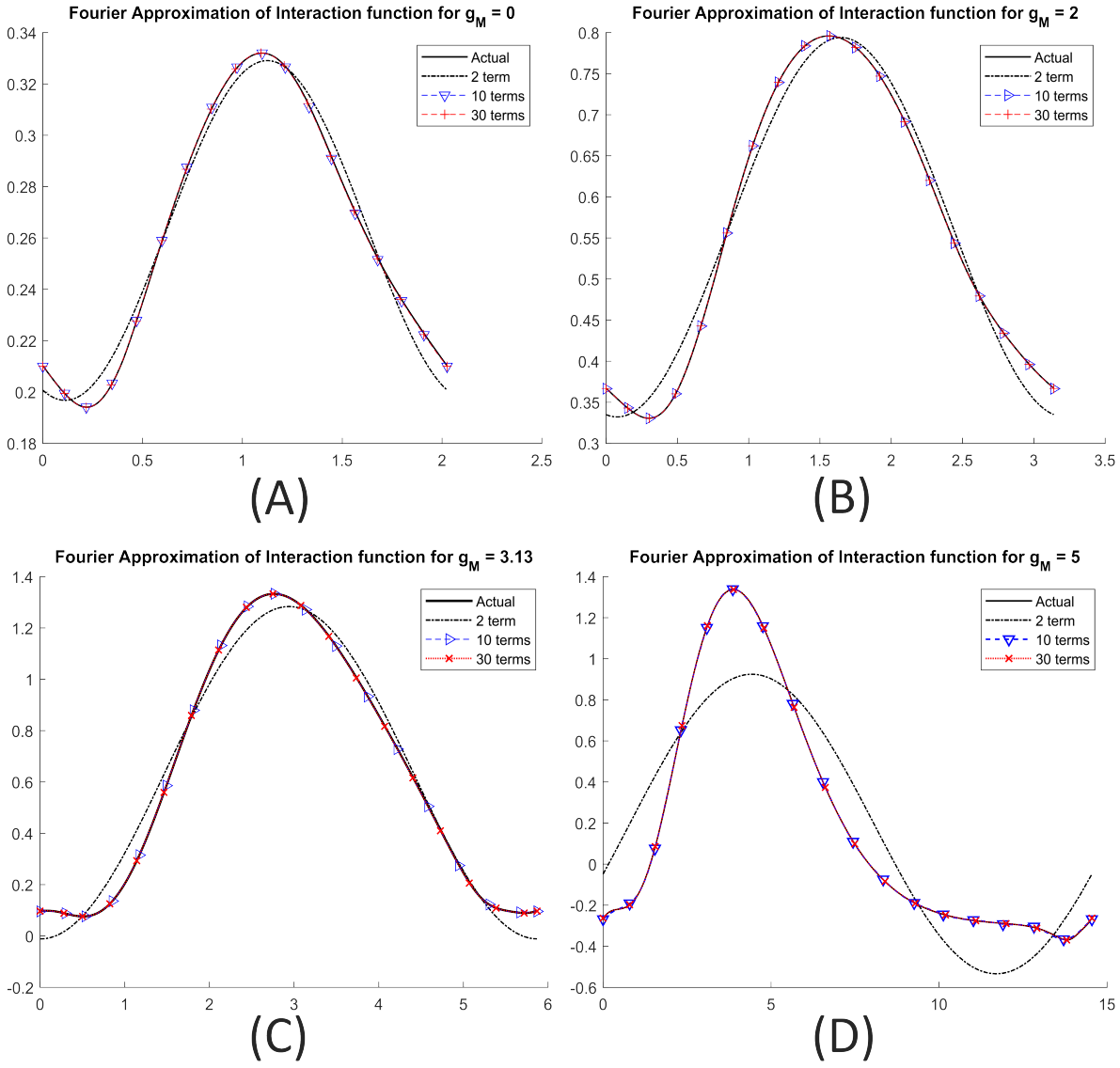


Figure C.1: Interaction function for the reduced Traub-Miles model (7.7) evaluated at four distinct values of the M-current maximal conductance, g_M. We compare the different approximations in each case using 2, 10 and 30 terms. **(A)** g_M is set to 0 **(B)** g_M is set to 2 **(C)** g_M is set to 3.13 **(D)** g_M is set to 5

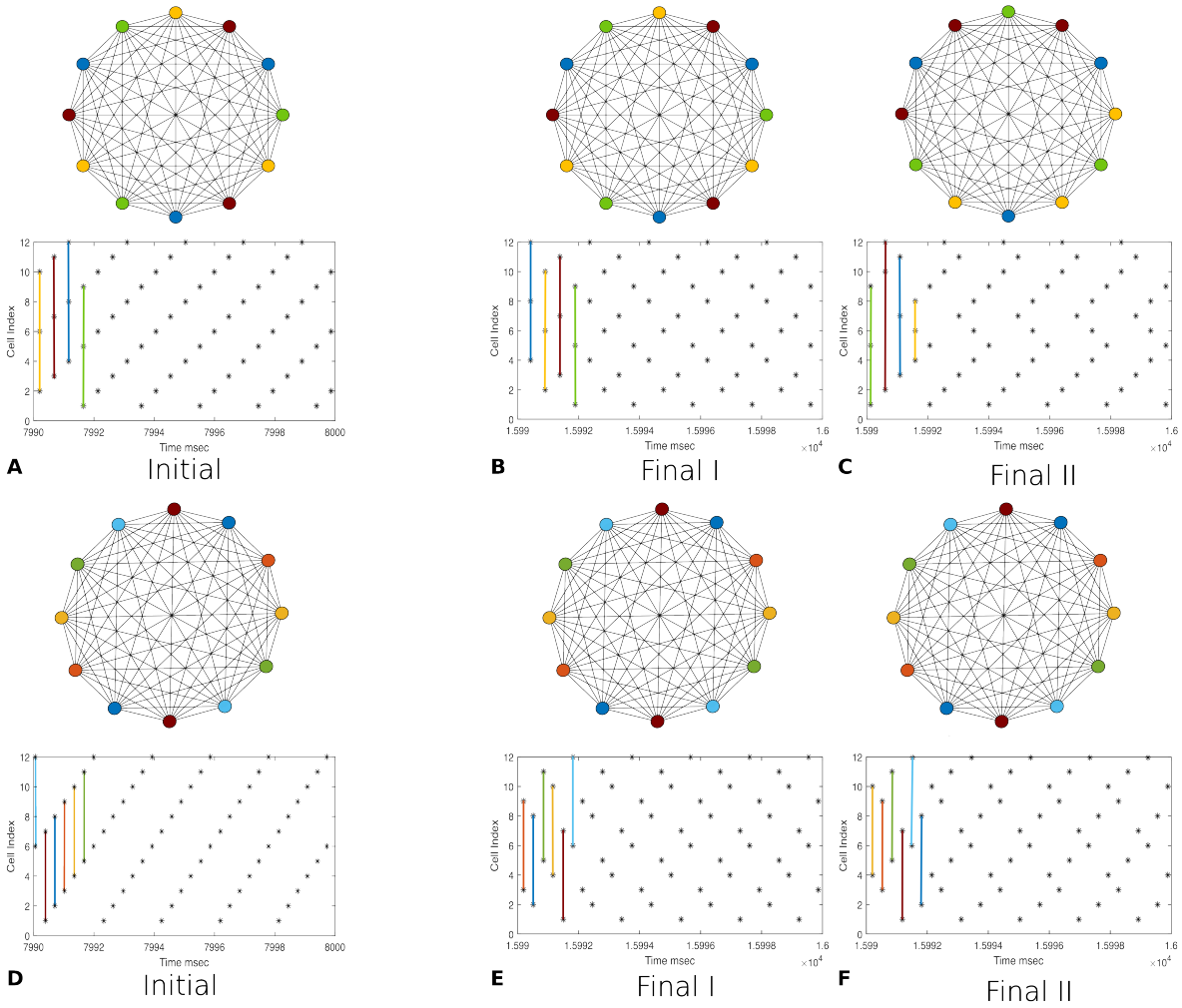


Figure C.2: Multistability when g_M is set to 0, in a network of 12 RTM model neurons with globally homogeneous coupling. **(A)** The network is initialized in a stable 4−cluster with a firing order: $C_1 - C_2 - C_3 - C_4$, where $C_i = \{i, i+4, \ldots, 7+i\}$. **(B)** A transient perturbation, in the form a current pulse, applied to a subset of the cells alters the firing order to $C_1 - C_4 - C_2 - C_3$. **(C)** Applying the pulse to a different subset of cell, can switch the network to a stable 4−cluster solution where the cells belonging to C_2 and C_4 change to $\{2, 6, 12\}$ and $\{4, 6, 8\}$ resp. **(D)** The network is initialized in a stable 6−cluster with a firing order: $C_1 - C_2 - C_3 - C_4 - C_5 - C_6$, where $C_i = \{i, i+6, \ldots, N-6-i\}$. A transient perturbation, in the form a current pulse, applied to different subset of the cells alters the firing order to **(E)** $C_1 - C_6 - C_4 - C_2 - C_5 - C_3$ and **(F)** $C_1 - C_6 - C_2 - C_4 - C_5 - C_3$.

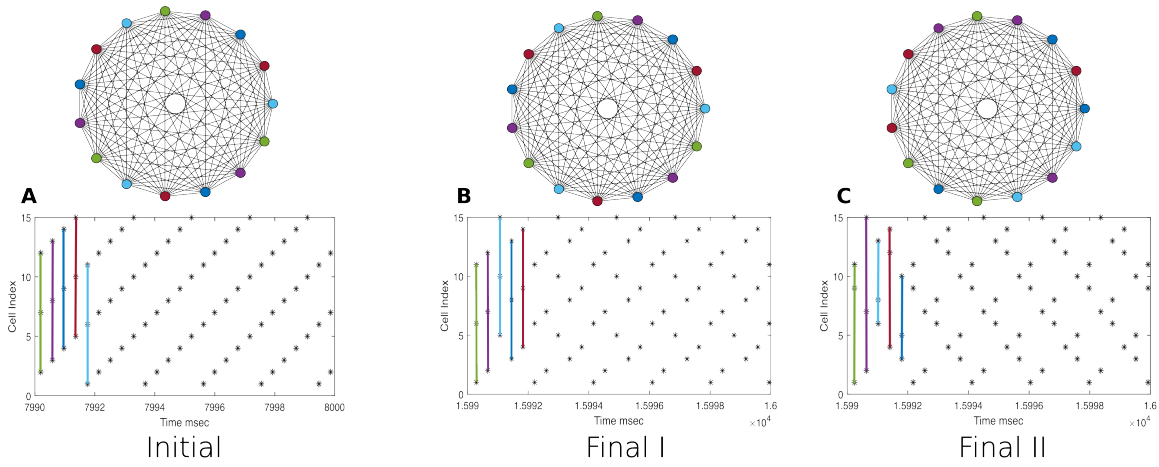


Figure C.3: Multistability when g_M is set to 0, in a network of 15 RTM model neurons with a globally homogeneous coupling. **(A)** The network is initialized in a stable 5− cluster solutions with a firing order $C_1 - C_2 - C_3 - C_4 - C_5$, where $C_i = \{i, i+5, i+5\cdot 2, \ldots, 10+i\}$, for $i = \{1,2,3,4,5\}$. **(B)** A transient perturbation applied to a subset of the cells in the network can alter the firing order of to $C_1 - C_2 - C_5 - C_3 - C_4$. **(C)** A transient perturbation applied to a different subset of cells, can alter both the firing order from (A) and the arrangement of the cells in each cluster. The new clusters are given by: $C_1 = \{1,9,11\}$, $C_2 = \{2,7,15\}$, $C_3 = \{3,5,10\}$, $C_4 = \{4,12,14\}$ and $C_5 = \{6,8,13\}$. The new firing order is given by: $C_1 - C_2 - C_5 - C_4 - C_3$.

In Figure C.3, panel (A) depicts a network of 15 RTM model neurons, initialized in a stable 5−cluster solution associated with a firing order: $C_1 - C_2 - C_3 - C_4 - C_5$, where $C_i = \{i, i+5, i+5\cdot 2, \ldots, 10+i\}$, for $i = \{1,2,3,4,5\}$. A transient current pulse applied to a subset of the cells in the network, can change the firing order to $C_1 - C_2 - C_5 - C_3 - C_4$, with no change to the cells occupying each cluster as illustrated in panel (B). A perturbation applied to a different subset of cells in the network, can switch the initial state from (A) to stable 5−cluster solution with a difference in both the firing order and in the arrangement of cells belonging to each cluster, as illustrated in panel (C). The new clusters are given by: $C_1 = \{1,9,11\}$, $C_2 = \{2,7,15\}$, $C_3 = \{3,5,10\}$, $C_4 = \{4,12,14\}$ and $C_5 = \{6,8,13\}$. The new firing order is given by: $C_1 - C_2 - C_5 - C_4 - C_3$.

C.4 Appendix for Section 7.4

We present the anti-phase ($n = 2$, $\psi = \pi$), 3−cluster and 8−cluster solutions that were found for $N = 6, 8, 16$ and 24 in Figure C.4. In C.4, panels (A)-(C) display a voltage trace

representation for the anti-phase, 3 and 8 cluster solutions respectively. The remaining panels, (D)-(I), below each voltage trace, the organization of the networks into n clusters are illustrated through raster plots and ring schematic. The ring diagrams are composed of N nodes, each representing a cell in the network, with lines between nodes indicating the bidirectional coupling architecture adopted by the system. Nodes sharing the same colour, represent cells belonging to the same cluster at the steady state. Each node also corresponds to one of the traces in the voltage trace plots (Panels (A)-(C)), identified by the same colour. Panels (D) and (I) both show raster plots for a network of 8 and 24 neurons that are in an anti-phase solution respectively. In each case, the network desynchronizes into two clusters: $C_1 = \{1, 3, 5, \ldots, 2 \cdot N - 1\}$ and $C_2 = \{2, 4, 6, \ldots, 2 \cdot N\}$ (with $N = 8, 24$), phase locking with phase difference $\psi = \pi$. Panels (B) and (I) show the $3-$cluster solutions obtained for a network of 6 and 24 neurons respectively. The clusters for this solution are given by: $C_i = \{i, i + 3, .., N - 3 - i\}$ for $i = \{1, 2, 3\}$ and $N = 6, 24$. In both solutions, the clusters will fire in the order of $C_1 - C_2 - C_3$ corresponding to $\psi = 2\frac{\pi}{3}$.

The phase model also predicts that an $8-$cluster solution corresponding to $\psi = 3\frac{\pi}{4}$ (or $5\frac{\pi}{4}$) is stable when g_M is set to 0 for $N = 8$ and 16. This solution is presented for both networks in Figure C.4 through panels (C),(F) & (I). Panel (C) shows the voltage trace for the solution, while panels (F) and (I) illustrate through a raster plot and a ring diagram, how a network of 8 and 16 neurons organize themselves into 8 clusters. In both cases, the arrangement and firing order is similar. For $N = 8$, the network exhibits a splay solution, where each cell forms its own cluster, and no two cells synchronize. For $N = 16$, the network desynchronizes into 8 clusters, each containing two cells. The clusters are given by $C_i = \{i, i+8\}$ for $i = \{1, 2, 3, 4, 5, 6, 7, 8\}$ .The firing order is $C_1 - C_4 - C_7 - C_2 - C_5 - C_8 - C_3 - C_6$ corresponds to an inter-cluster (or cell for $N = 8$) phase difference of $\psi = 3\frac{\pi}{4}$.

In Figure C.5, panel (A) shows a network of 12 RTM model neurons with no M-current ($g_M = 0$), initialized in a stable $4-$cluster solution with an inter-cluster phase difference of $\psi = \frac{\pi}{2}$. Panel (B) shows that a transient perturbation, applied to a subset of the cells, can reverse the firing order of the initial state and switch the network to a different stable $4-$cluster solution associated with $\psi = 3\frac{\pi}{2}$. Panels (C) & (D) show that the network can also switch into different stable $12-$cluster solutions by applying the perturbation to a different subset of cells. In this case, the network can switch into a $12-$cluster solution where ψ is either $5\frac{\pi}{6}$ (associated with a firing order: $C_1 - C_6 - C_{11} - C_4 - C_9 - C_2 - C_7 - C_{12} - C_5 - C_{10} - C_3 - C_8$) or $7\frac{\pi}{6}$ (associated with a firing order: $C_1 - C_8 - C_3 - C_{10} - C_5 - C_{12} - C_7 - C_2 - C_9 - C_4 - C_{11} - C_6$)

C.5 Appendix for Section 7.5

We present the anti-phase ($n = 2, \psi = \frac{\pi}{2}$), 3−cluster and 5−cluster solutions found for arbitrary networks in Figure C.6. Just like in the previous sections, panels (A)-(C) display the voltage traces corresponding to each n−cluster solution. And the panels (D)-(I) illustrate how the network will form the clusters corresponding to the voltage traces in the above panels. The ring figures show the coupling architecture of the network, with each node representing an RTM model neuron. The colour is an identifier to the cluster it belongs to as indicated in the raster plots and voltage trace. In Figure C.6, panel (A) shows a representation of the voltage trace corresponding to network of 4 (D),6 (G) and 24(I) cells respectively, in a steady anti-phase solution. The two clusters are given by $C_1 = \{1, 3, 5, .., N-1\}$ and $C_2 = \{2, 4, 6, .., N\}$. Panels (E),(H) and (K) show the 3−cluster solutions obtained for a network of N neurons with clusters given by to $\psi = \frac{2\pi}{3}$ with a firing order of $C_1 - C_2 - C_3$, whereas (H) corresponds to $\psi = \frac{4\pi}{3}$ with reverse firing order, $C_3 - C_2 - C_1$.

Panels (F),(I) and (L) show the 5−cluster solutions in a network of $5, 10$ and 15 cells respectively. For each size N, the clusters are given by $C_i = \{i, i+5, \ldots, N-5-i\}$ for $i = \{1, 2, 3, 4, 5\}$. In panel (F), the order in which the clusters fire is $C_1 - C_4 - C_2 - C_5 - C_3 - C_1$ which corresponds to a phase difference of $\psi = \frac{4\pi}{5}$. The reverse firing order ($C_1 - C_3 - C_5 - C_2 - C_4$) is observed in panel (L) corresponding to a phase difference, $\psi = 2\pi - \frac{4\pi}{5} = \frac{6\pi}{5}$. In panel (I), the firing order is given by $C_1 - C_2 - C_3 - C_4 - C_5$, which corresponds to a phase difference $\psi = \frac{2\pi}{5}$. The remaining 5−cluster solution corresponding to $\psi = \frac{8\pi}{5}$ (reverse firing order of $\psi = \frac{2\pi}{5}$) was not obtained during simulations.

We obtained the 4−cluster for a network of 4 cells as shown in panel (A) of Figure C.7. In this case, the solution corresponds to splay state for $N = 4$, in which cells fire in order of $\{1, 2, 3, 4\}$ associated with a phase difference ψ of $\frac{\pi}{2}$. In addition to this, we obtained splay states for $N = 7$ and 9, illustrated in panels (B) and (C) respectively, in Figure C.7. In panel (B), the cells fire in the order of $\{1, 3, 5, 7, 2, 4, 6\}$ corresponding to $\psi = \frac{8\pi}{7}$, and in panel (C), the cells fire in the order $\{1, 8, 6, 4, 2, 9, 7, 5, 3\}$ corresponding to $\psi = \frac{8\pi}{9}$.

Consider Figure C.8, where a network of 12 RTM model neurons are initialized in a stable 3−cluster solution associated with $\psi = 2\frac{\pi}{3}$, shown in panel (A). A transient current pulse applied to a subset of the cells can switch the network can reverse the firing order of the cells forming a stable 3−cluster solution associated with a different phase difference given by, $\psi = \frac{4\pi}{3}$, depicted in panel (B). Applying the perturbation to a different subset of cells can also switch the network to a stable 12−cluster solution or equivalently, a splay state, with a firing order: $\{1, 8, 3, 10, 5, 12, 7, 2, 9, 4, 11, 6\}$ associated with $\psi = 5\frac{\pi}{6}$, depicted

in panel (C). A third possibility could arise in which a perturbation to a subset of the cells could also switch the network to the anti-phase solution.

Similar transitions were observed in a network of 24 cells, initialized in a $3-$cluster solution associated with $\psi = 2\frac{\pi}{3}$, as illustrated in panel (E). A current pulse applied to a subset of the cells, can switch the network to a stable $12-$cluster solution where the clusters are defined as $C_i = \{i, i+12\}$ for $i = \{1, 2, 3, 4, 5, 6, \ldots, 12\}$. In particular, stimulating different cells could give rise two different realizations of the same stable $12-$cluster solutions as depicted in panels (F) and (G). The firing order in panel (F) is given by: $\{C_1 - C_6 - C_{11} - C_4 - C_9 - C_2 - C_7 - C_{12} - C_5 - C_{10} - C_3 - C_8\}$, which is associated with the equilibrium $\psi = 7\frac{\pi}{6}$. The reverse firing order is obtained in panel (G), associated with $\psi = 7\frac{\pi}{6}$. The network can also switch to the anti-phase solution as depicted in panel (H).

Panel (A) in Figure C.9, depicts a network of 8 cells, initialized in a stable splay state associated with $\psi = \frac{\pi}{4}$. Applying a perturbation to a subset of the cells, could synchronize the solution. Similarly panels (B) and (C) depict a network of 12 cells, initialized in a stable splay and stable $6-$ cluster solutions associated with $\psi = \frac{\pi}{6}$ and $\psi = \frac{\pi}{3}$ respectively. Both solutions could transition to a fully synchronized state as illustrated in panel (D) through transient perturbations applied to a subset of the cells in the network halfway through the simulation.

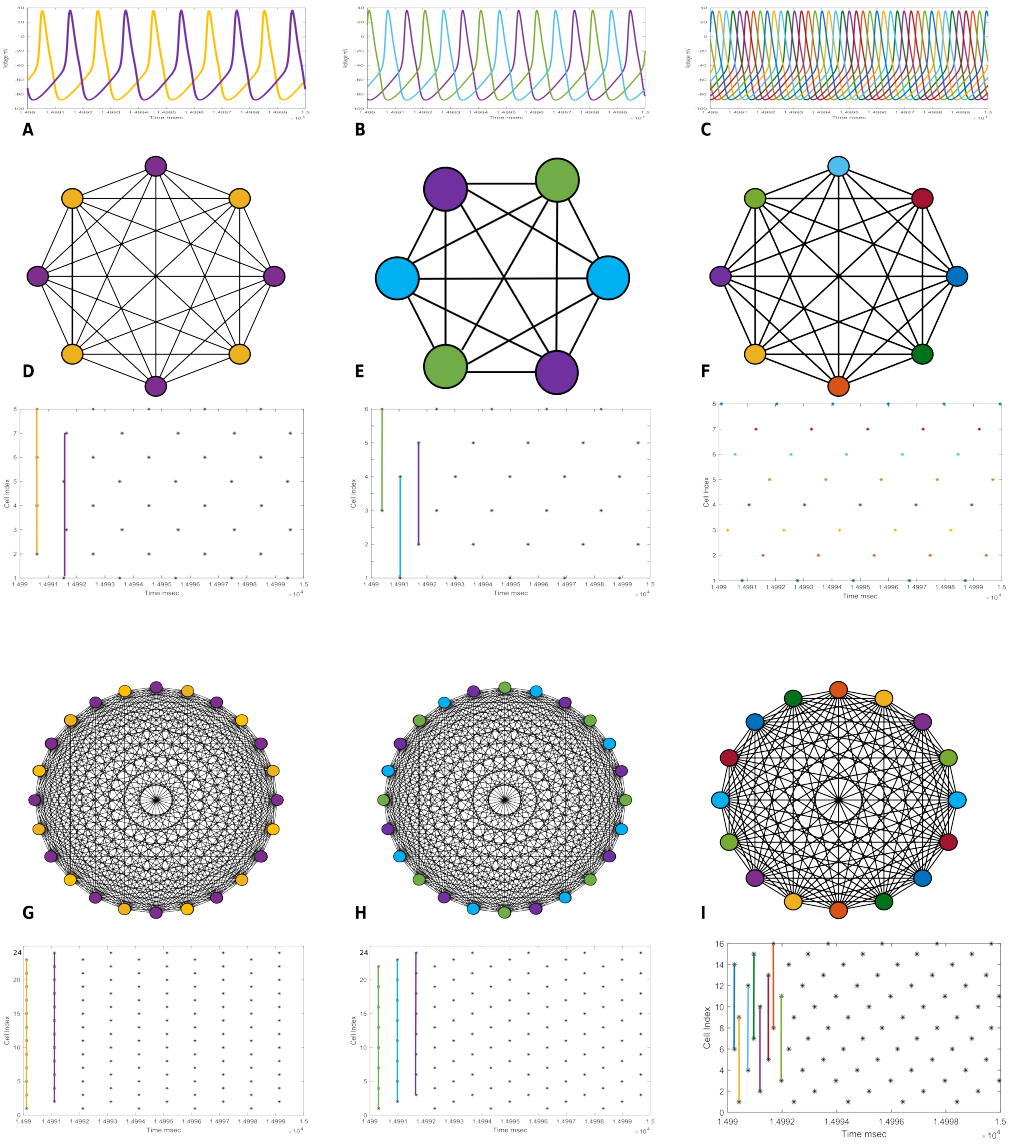


Figure C.4: Multistability in a network of reduced Traub-Miles model neurons (RTM) equipped with a monotonic globally heterogeneous coupling ($p = 0.5$, $k = \lfloor N/2 \rfloor$), with g_M set to 0. The solutions are presented through voltage traces, raster plots and ring diagrams to illustrate the spike timing and coupling architecture, respectively. Each node in the ring represents a spiking cell. Nodes sharing the same colour belong to the same cluster. Voltage trace representations are presented for **(A)** anti phase, **(B)** 3−cluster and **(C)** 8−cluster solutions. **(D)** Anti-phase solution ($\psi = \pi$) obtained for a network of 8 cells **(G)** Anti-phase solution for a network of 24 cells. **(E)** 3−cluster solution for a network of 6 cells $\left(\psi = \frac{2\pi}{3}\right)$. **(H)** 3−cluster solution for a network of 24 cells associated with $\left(\psi = \frac{2\pi}{3}\right)$. **(F)** 8−cluster solution obtained for a network of 8 cells **(I)** 8−cluster solution $\left(\psi = \frac{3\pi}{4}\right)$ obtained for a network of 16 cells. The cluster firing order is discussed in the main text.

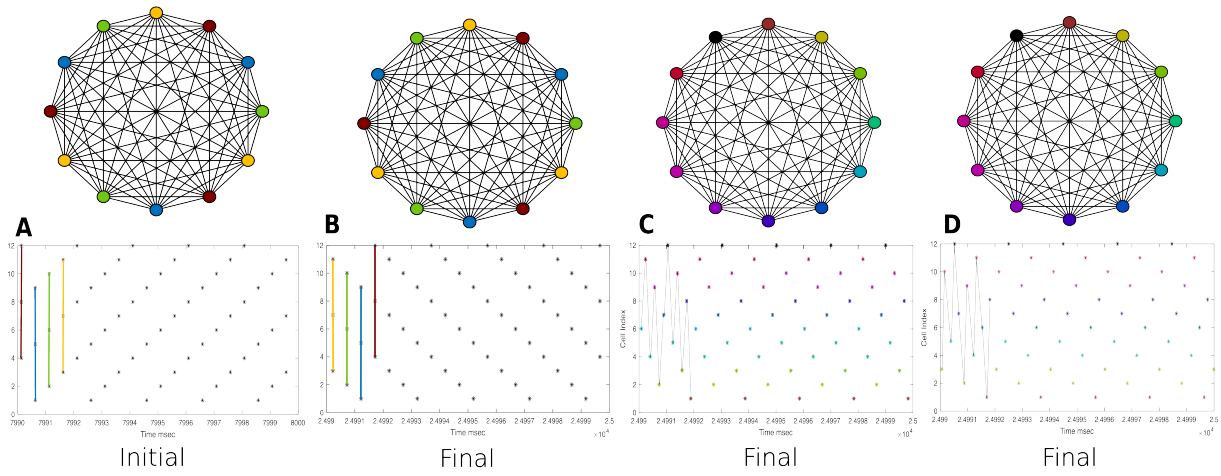


Figure C.5: Multistability in a network of 12 RTM model neurons equipped with distance dependent coupling ($p = 0.5, k = 6$) with g_M set to 0. A transient perturbation is applied to a subset of the cells for time $t \in [8000, 8050]$. **(A)** The network is initialized in a stable $4-$cluster solution corresponding to an inter-cluster phase difference of $\psi = \frac{\pi}{2}$. **(B)** The perturbation reverses the firing order of the solution from (A), switching the network to a different stable $4-$cluster solution $\left(\psi = 3\frac{\pi}{2}\right)$. **(C)** A transient perturbation applied to a different subset of cells can switch the network in (A) to a stable $12-$cluster solution associated with a inter-cell phase difference of $\psi = 5\frac{\pi}{6}$. **(D)** The perturbation can also switch the network in (A) to a $12-$cluster associated with $\psi = 7\frac{\pi}{6}$.

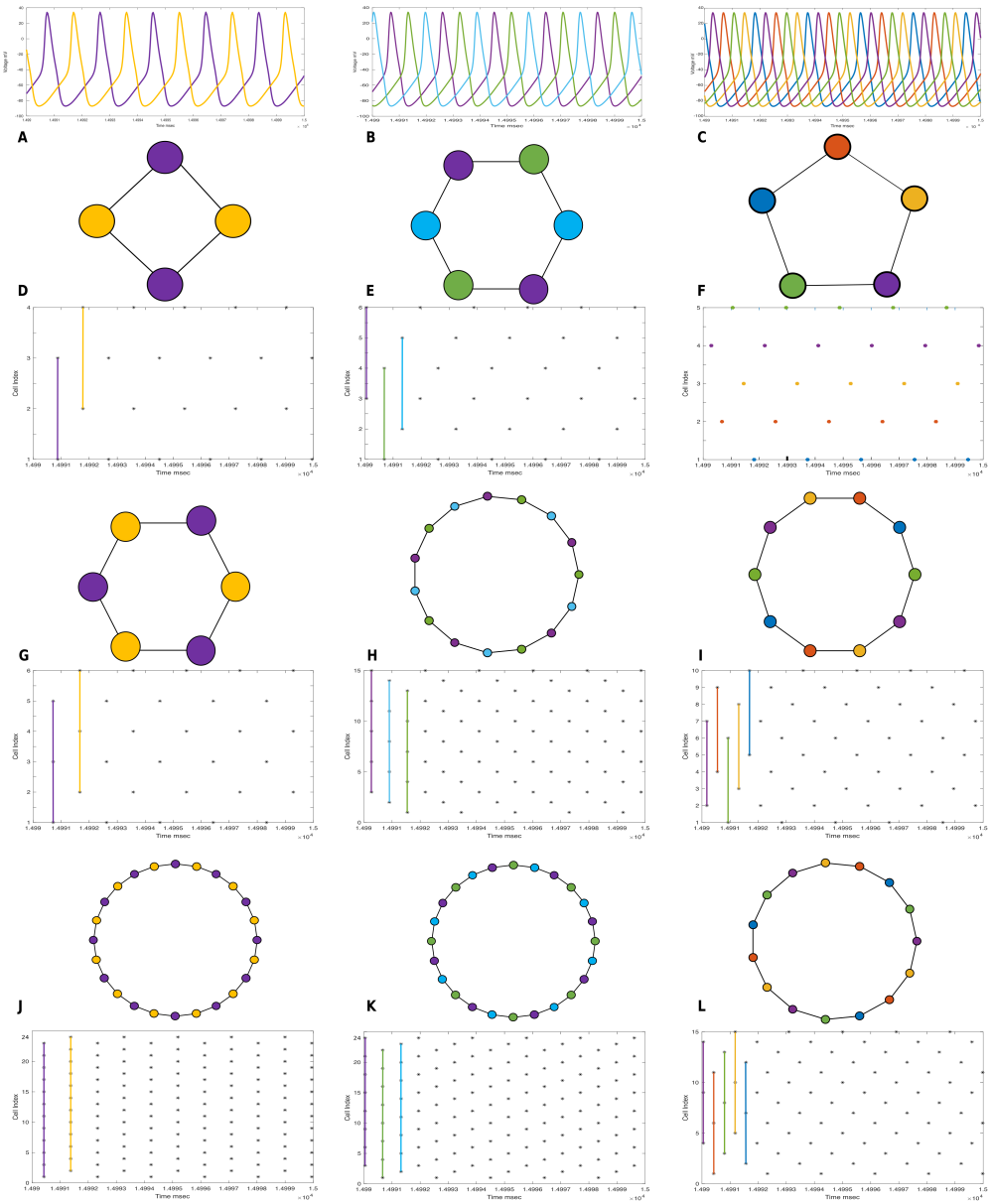


Figure C.6: Demonstration of multistablity within a network of RTM model neurons, equipped with nearest neighbour coupling and g_M set to 0. **(A)-(C)** display the voltage traces for each solution. The solutions are presented in two ways: Ring diagrams depicting the *nearest neighbour coupling* and the cells belonging to the same cluster (identified by the same colouring), and raster plots which display the firing order of the clusters. **(D),(G)** and **(J)** illustrate the anti-phase solutions for a network of 4, 8 and 24 cells resp. **(E),(H)** and **(K)** are the 3− cluster solutions for 6 ($\psi = \frac{2\pi}{3}$),15($\psi = \frac{4\pi}{3}$) and 24 ($\psi = \frac{2\pi}{3}$) cells resp. **(F),(I)** and **(L)** are the 5− cluster solutions for a network of 5($\psi = \frac{4\pi}{5}$) ,10($\psi = \frac{2\pi}{5}$) and 15($\psi = \frac{6\pi}{5}$) cells resp. The cluster ensembles and the order in which they fire are discussed in the main text.

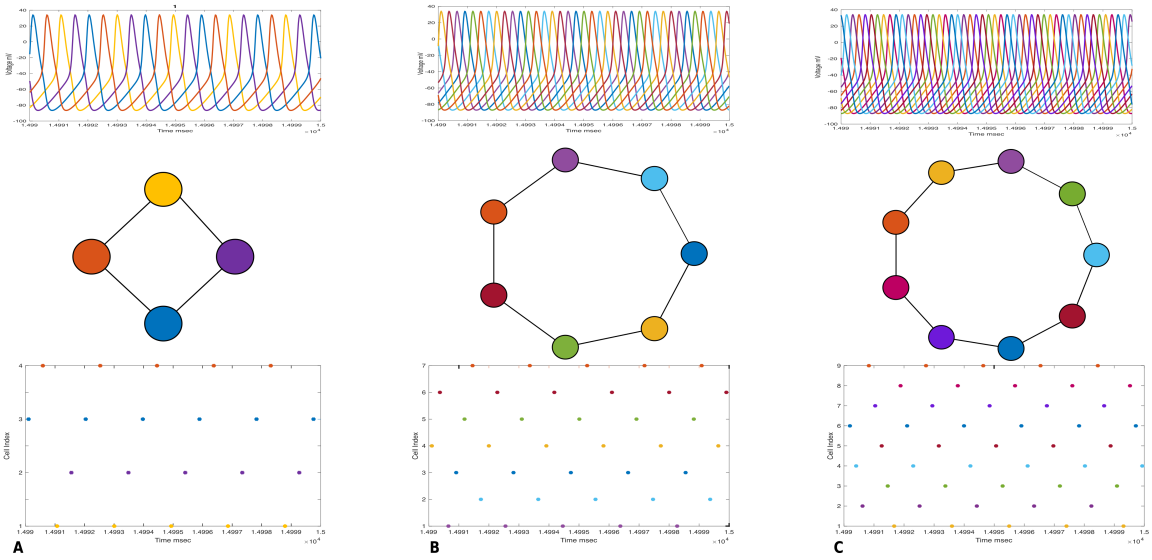


Figure C.7: Splay solutions are obtained for a network of RTM model neurons equipped with nearest neighbour coupling and with g_M set to 0. The solutions are presented in three ways: Voltage traces, Ring diagrams depicting the coupling architecture, and raster plots which tell us which cells fire when in a single cycle. **(A)** A splay state obtained for a network of 4 cells, corresponding to $\psi = \frac{\pi}{2}$. **(B)** A splay state obtained for a network of 7 cells, with $\psi = \frac{8\pi}{7}$. **(C)** A splay state obtained for 9 cells with $\psi = \frac{8\pi}{9}$. The cluster ensembles and the order in which they fire are discussed in the main text.

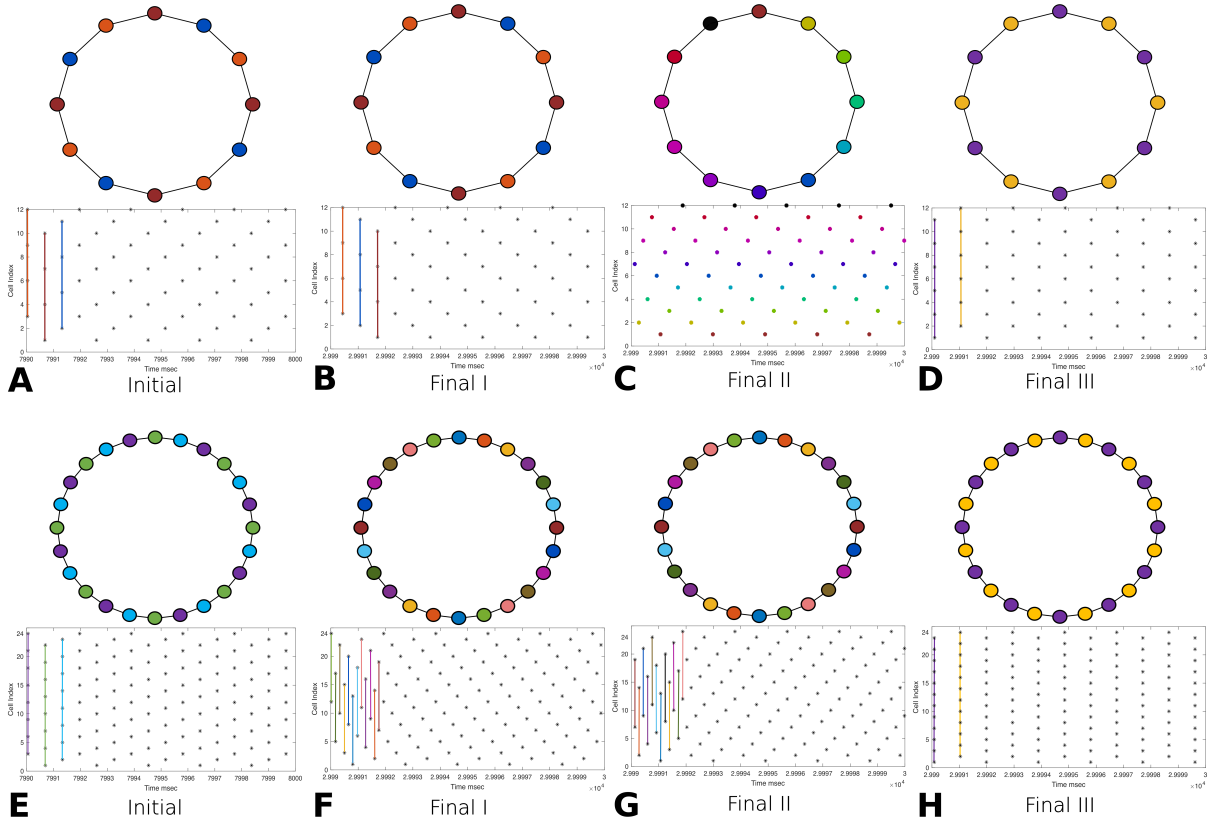


Figure C.8: Demonstration of the possible transitions of a network, equipped with nearest neighbour coupling, initialized in a stable 3−cluster solution, when g_M is set to 0. **(A)** A network of 12 neurons is initialized in a stable 3−cluster solution associated with $\psi = 2\frac{\pi}{3}$. A transient perturbation, in the form of a current pulse, applied to a subset of cells in the network, can switch it to a **(B)** stable 3−cluster solution with the reverse firing order associated with $\psi = 4\frac{\pi}{3}$, or **(C)** a stable 12−cluster solution (splay) associated with $\psi = 5\frac{\pi}{6}$, or **(D)** an anti-phase solution ($\psi = \pi$). **(E)** A network of 24 neurons is initialized in a stable 3−cluster solution associated with $\psi = \frac{2}{\pi}3$. A transient perturbation, in the form of a current pulse, applied to a subset of cells in the network, can switch it to a **(F)** stable 12−cluster solution associated with $\psi = 7\frac{\pi}{6}$, or **(G)** a stable 12−cluster solution (splay) associated with $\psi = 5\frac{\pi}{6}$, or **(H)** an anti-phase solution ($\psi = \pi$).

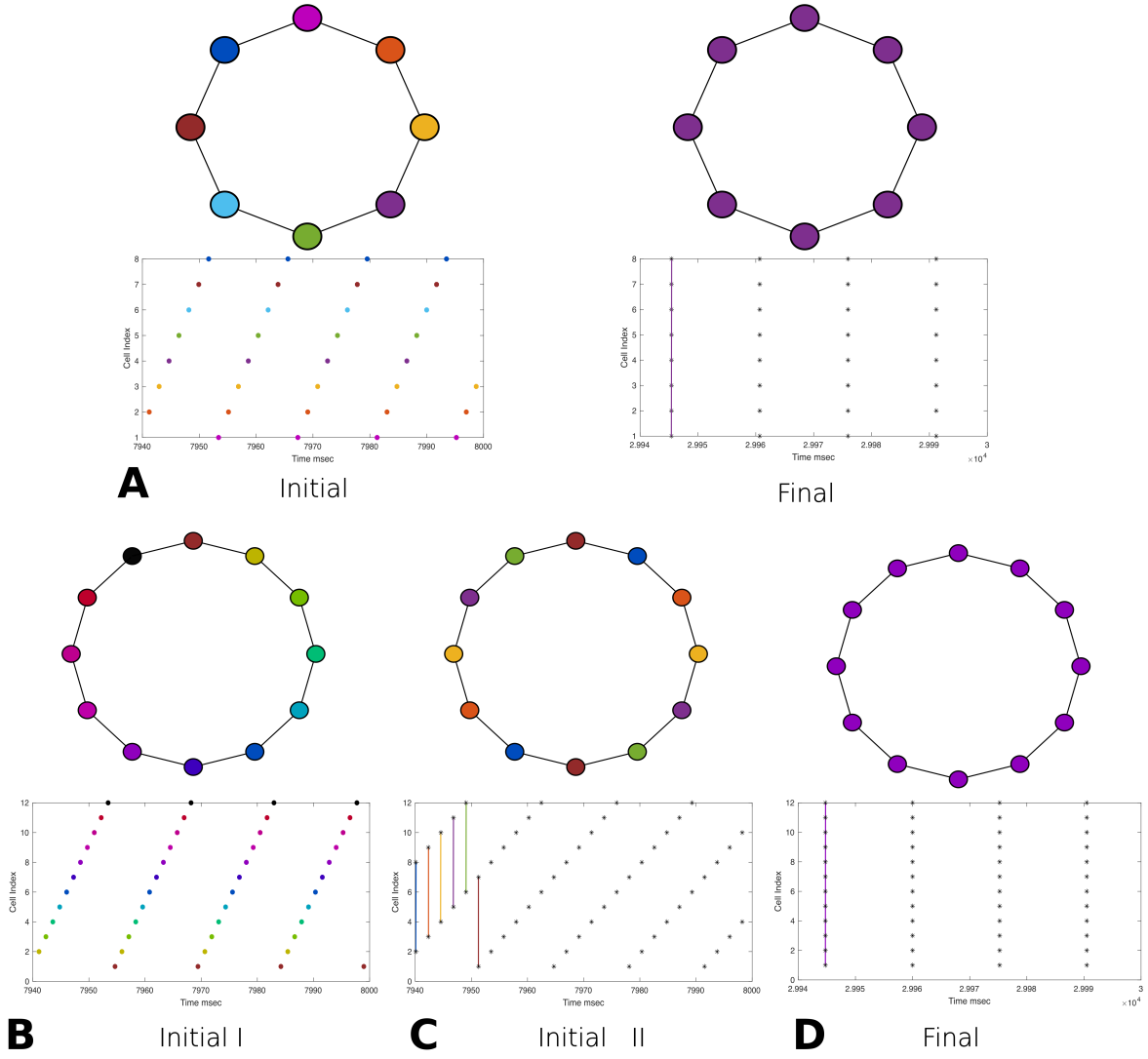


Figure C.9: Demonstration of synchrony within a network of RTM model neurons equipped with nearest neighbour coupling, when g_M is set to 5, obtained through transient current pulses applied to an initialized network, equipped with nearest neighbour coupling. **(A)** A network of 8 cells, initialized in a splay state ($\psi = \frac{\pi}{4}$) , can synchronize under the transient perturbation applied to a subset of the cells in the network (labelled initial and final respectively). A network of 12 cells is initialized in a **(B)** stable splay state ($\psi = \frac{\pi}{6}$), and a **(C)** stable 6− cluster solution ($\psi = \frac{\pi}{3}$) **(D)** A transient perturbation applied to a subset of the cells in the network, initialized in (C) and (D), can synchronize the network.